ATMIRE

Title	Study of the organic content and mineralogy effects on the acoustic properties of the Niobrara Formation, Denver Basin
Item Type	Text
Authors	Al-Khalifa, Aqeel M.
Publisher	Colorado School of Mines. Arthur Lakes Library
Rights	Copyright of the original work is retained by the author.
Download date	2026-11-28 02:31:41
Link to Item	https://hdl.handle.net/11124/170312

STUDY OF THE ORGANIC CONTENT AND MINERALOGY EFFECTS ON THE ACOUSTIC PROPERTIES OF THE NIOBRARA FORMATION, DENVER BASIN

by

Aqeel M. Al-Khalifa

A thesis submitted to the Faculty and the Board of Trustees of the Colorado School of Mines in partial fulfillment of the requirements for the degree of Master of Science (Geology).

Golden, Colorado

Date_____

Signed: _____

Aqeel M. Al-Khalifa

Signed: _____

Dr. Stephen A. Sonnenberg

Thesis Advisor

Golden, Colorado

Date_____

Signed: _____

Dr. Paul M. Santi

Professor and Head

Department of Geology and Geological Engineering

ABSTRACT

Wattenberg Field has been producing hydrocarbons since 1970. Over the past 20 years, evolution of horizontal drilling and hydraulic fracturing allowed for the expansion of unconventional gas and oil production from Niobrara chalk and marl intervals across the Greater Wattenberg Area (GWA). The Niobrara carbonate system in the Denver Basin contains a TOC range of 1-8 wt.%. Additionally, GWA is associated with a geothermal anomaly. This study investigates the effects of TOC, clay content and kerogen maturity levels on the acoustic properties of Niobrara chalk and marl intervals. Core samples from Gill Land Associates 2 and Berthoud State 3 wells were analyzed for total organic content richness and maturity. Compressional and shear ultrasonic velocities were measured under variable confining pressures up to 4000 psi. Lab measurements were integrated with source rock analysis and XRD mineralogy to establish significant correlations between acoustic properties and organic maturity. A "blind test" was performed in which the correlation models were used to predict organic carbon richness and source rock maturity indices using wireline logs from Aristocrat PC H11-07 well with measured mineralogy and organic carbon richness. Correlations with statistical significance are presented in this study. A significant correlation was established between core-calibrated porosity and V_{P0}/V_{S0} ratio. Results show that B and C intervals within the Smoky Hill Member generally have higher stiffness than A and D intervals and Ft. Hays limestone. Higher illite clay content decreases the 45° and 90° velocities significantly. In contrast higher carbonate volume shows a reverse effect. Samples rich in TOC had noticeably lower C33 and C12 stiffness coefficients. Existing hydrocarbons in the sample increase the rigidity of the sample. Higher S2 content seem to increase the shear wave velocity in the 45° and 90° directions while slowing down the overall compressional wave velocity. The previously introduced uranium spectral gamma ray method for TOC prediction by (ElGhonimy, 2015) show closer pattern to the core measured TOC. In contrast, the method presented in this study is a function of shear and compressional wireline acoustic log responses. TOC prediction from C12 provides qualitative TOC richness assessment. The introduced model results show moderate accuracy in clay-rich zones. Accuracy of estimated TOC richness was observed to be higher specifically in the C marl interval compared to a higher accuracy in the B marl when using the uranium method.

TABLE OF CONTENTS

ABSTRACT iii
LIST OF FIGURES vi
LIST OF TABLES xiii
AKNOWLEDGMENTS xiv
CHAPTER 1 INTRODUCTION 1
1.1 Objectives and Purpose 1
1.2 Project Overview and Dataset 2
1.3 Study Area 3
1.3.1 Regional Structural Setting 5
1.3.2 Stratigraphy 5
1.4 Previous Work 7
CHAPTER 2 METHODS 13
2.1 Core Description and Sampling 13
2.2 Source Rock Analysis (SRA) 15
2.3 X-Ray Diffraction Analysis (XRD) 15
2.4 Ultrasonic Measurements 17
2.4.1 Sample Preparation 18
2.4.2 Benchtop 18
2.4.3 Confined Pressure Test 18
2.5 Statistical Analysis 21
CHAPTER 3 RESULTS 23
3.1 Cores Sedimentology 23
3.1.1 Facies Analysis 24
3.2 Ultrasonic Velocity Measurements 32
3.2.1 Benchtop Velocity 32
3.2.2 Confined Pressure Velocity 32
3.2.3 Anisotropy Analysis 33
3.3 Organic Content and Maturity 50
3.3.1 Total Organic Carbon and Kerogen Type 50
3.3.2 Source Rock Maturity 54
3.4 X-Ray Diffraction Mineralogy 54

CHAPTER 4 DISCUSSION 59
4.1 Porosity Effect 59
4.2 Mineralogy Effect 62
4.3 Effects of Organic richness and Maturity 65
4.4 Estimating Organic Richness and Maturity 71
CHAPTER 5 CONCLUSIONS 83
REFERENCES CITED 86
APPENDIX A 89

LIST OF FIGURES

Figure 1.1 Location map of Denver Basin and Wattenberg field (Nelson and Santus, 2011). Location of the main cores used field in the study from Wattenberg are marked. Location of cross section A-A' (Figure 1.2) is also marked. 3

Figure 1.2 East-West cross section of Denver Basin. Niobrara is in the generation window on the western flank but thermally immature on the eastern flank (Sonnenberg, 2011). For location: see Figure 1.1 4

Figure 1.3 Stratigraphic column of the Denver Basin showing Niobrara stratigraphy (Sonnenberg, 2011). 4

Figure 1.4 Tectonic elements affecting the formation of Western Interior Basin (Weimer, 1983)..... 5

Figure 1.5 Niobrara Isopach map showing thinning of sediments toward the center of Wattenberg structure (Weimer et al., 1986). 6

Figure 1.6 Schematic Niobrara depositional model (Sonnenberg, 2011). Paleoclimates and paleohighs played a major role in facies distribution. 7

Figure 1.7 Lithological trends within the Western Interior Seaway Cretaceous Basin (Longman et al., 1998). 8

Figure 1.8 Matrix compressional stiffness related to kerogen volume. Two cases of clay content are indicated (Vernik and Milovac, 2011). 9

Figure 1.9 Vertical and horizontal compressional velocity as a function of variable confining pressure for the lower marl (Maldonado, 2011). The upper plot represents constant differential pressure, lower plot represents constant pore pressure..... 11

Figure 1.10 Vertical compressional velocity as a function of variable confining pressure for the D chalk (Maldonado, 2011). The upper plot represents constant differential pressure, lower plot represents constant pore pressure. 12

Figure 2.1 Source rock analyzer used for samples analysis..... 16

Figure 3.2 (A) schematic diagram for XRD analysis, (B) shows an example analysis results (Cullity, 1956). 17

Figure 2.3 shape and dimensions of core slab and plug samples acquired for Berthoud State 3 (Not to scale). 19

Figure 2.4 Benchtop velocity measurement setup (panametric transducers images are courtesy of Olympus Corporation). Experiment is repeated for each direction. Diagram is not to scale. 19

Figure 2.5 Sample jacket design, courtesy of (Panfiloff, 2016), used for confined pressure velocity measurements. Due to limitations on core plug sample size, resistivity measurments were not collected. Pore pressure line was isolated using a screw plug. 21

Figure 3.1 Core description and formation tops for Berthoud State 3 core. For location see Figure 1.1 25

Figure 3.2 Core description and formation tops for the Gill Land Associates 2 core. For location see Figure 1.1 26

Figure 3.3 Facies samples from Gill Land Associates 2 core. (A) Weakly bioturbated marl (depth: 6707 ft). (B) Horizontally stratified pelletal chalky marl (depth: 6739 ft). (C) Moderately bioturbated marly chalk (depth: 6851ft). (D) Highly bioturbated bioclastic chalk (depth: 6845 ft). (E) Bioturbated bioclastic limestone (Depth: 6890.4 ft). For location see Figure 1.1. 27

Figure 3.4 Scanning electron microscopy images (SEM) of four samples from Gill Land 2 core. (A) clay rich marly chalk sample from the C-chalk showing a clay-lined pyrite framboid (Py), cocolith fragments (CF) and abundant interlayered illite and smectite clays (I/S). (B) well preserved Coccosphere surrounded by cocolith fragments and interlayered illite/smectite. (C) undifferentiated uniserial foraminifera, chambers display multiple patterns of cementation: calcite crystals (Ct) and micrite (Mi). (D) chalky marl sample showing microfractured calcite crystal, cocolith fragments and pyrite framboid. 29

Figure 3.5 Core sample from Gill Land Associates 2 core. Black arrows mark macro inoceramid fragments. Red arrows highlight pyritized ash beds (Bentonites). For well location see Figure 1.1 30

Figure 3.6 Sample facies distribution for studied intervals. Data shown for Berthoud State 3 core. 31

Figure 3.7 Compressional and shear wavelets examples from the acquired dataset. Results are from the parallel to bedding measurements for sample 3101.9 ft from Berthoud State3 core. The top waveforms were captured at 4000 psi confining pressure. Lower two waveforms represent benchtop 0 psi conditions. Vertical scale is amplitude. Horizontal scale is time. Arrow symbols demonstrate first arrival velocity picking. The vertical scale was modified for benchtop results to enhance the waveform. 35

Figure 3.8 Velocity measurements under confined pressure for sample 3013.75 ft from Berthoud State 3 core. Horizontal axis is pressure; it shows the continuous range of pressures at which the samples were tested (i.e. pressuring up to 4000 psi followed by a pressuring down to 0 psi in a single continuous experiment). Vertical scale is velocity in km/s. Both compressional and shear velocities show modified velocity pattern during pressuring down stages. Velocities measured along the 90° exhibit the highest change in velocity in response to pressure change. 36

Figure 3.9 Velocity measurements under confined pressure for sample 3054.1 ft from Berthoud State 3 core. Both compressional and shear velocities show modified velocity patterns during pressuring down stages. 37

Figure 3.10 Velocity measurements under confined pressure for sample 3077.4 ft. from Berthoud State 3 core. Velocity change in response to pressure for this sample is much less pronounced when compared to the other tested samples. 38

Figure 3.11 Velocity measurements under confined pressure for sample 3101.9 ft from Berthoud State 3 core. Both compressional and shear velocities show modified velocity patterns during pressuring down stages. 39

Figure 3.12 Schematic illustration of principal axes of rotation, orientation of measured velocities and orientation of stiffness coefficients discussed in any transversely isotropic medium. Note: both X1 and X2 are parallel to bedding axes whereas X3 is perpendicular to bedding plane. 41

Figure 3.13 Crossplots of calculated stiffness coefficients (in giga Pascals, Gpa) from measured velocities versus applied confining pressure (in psi). All samples are from the Berthoud State 3 core. Samples shown are: (A) B chalk. (B) B marl. (C) C chalk. (D) C marl. Generally, stiffness is greater in the three observed directions (i.e. 0°, 45° and 90°) in sample 3077. The latter sample particularly shows different behavior when compared to the other three samples. 43

Figure 3.14 Stiffness coefficients (in Gpa) for benchtop measured velocities plotted against depth (in ft.). Left plot is for Gill Land 2 core samples. Right plot is for Berthoud State 3 core samples. This plot provides comparable multidirectional stiffness measurements for all Niobrara Formation interval. Ft. Hays limestone samples shows the highest stiffness coefficients in all directions. A moderate increase in stiffness can be observed in B and C samples when compared to the other intervals within the Smoky Hill Member. 44

Figure 3.15 Thomsen anisotropy parameters from benchtop velocities. Right plot shows Berthoud State 3 core samples. Left plot shows Gill Land 2 core samples. Samples are annotated with the origin of sample interval. It is very important to note that Thomsen anisotropy parameters are much

lower in magnitude for Berthoud State 3 core samples. Note the horizontal scale difference. Ft. Hays samples anisotropies are very low suggesting an isotropic acoustic behavior. 45

Figure 3.16 Thomsen anisotropy parameters calculated from measured velocities under different confining pressures. (A) sample from B chalk, (B) B marl, (C) C chalk and (D) C marl. All sample exhibit major change in all anisotropies at 250 psi except sample 3077.4 ft. While all the samples don't show major changes in their anisotropies beyond 250ps, 3077.4 sample shows noticably increasing epsilon and gamma anisotropies beyond 2500psi. 46

Figure 3.17 Crossplots of elastic moduli versus confining pressure: Bulk modulus (K),vertical shear modulus (Go), horizontal shear modulus (Gh), (Ev) and (Eh) are vertical and horizontal Young's modulus respectively. (A) sample from B chalk, (B) B marl, (C) C chalk and (D) C marl. All samples share similar trend beyond 250 psi in bulk modulus, shear moduli and vertical Young's modulus. Sample 3077 shows distenctivly smaller change between 0-250 psi. Bulk modulus is semi-stable beyond 250 psi in B samples whereas it increases in C samples..... 48

Figure 3.18 Poisson's ratio as a function of variable confining pressure. v13 is ratio of change X3/X1, v31 is for X1/X3 and v12 is for X1/X2. See Figure 3.12 for illustration of axes orientation. (A) sample from B chalk, (B) B marl, (C) C chalk and (D) C marl. Specifically in sample 3077.4, the effect of confining pressure on the change in Poisson's ratio seems to be minimal. .. 49

Figure 3.19 Plots of source rock analysis data: (A) maturity plot using Tmax and productivity index (PI), (B) kerogen typing from S2 versus TOC values, (C) maturation levels from Tmax and hydrogen index (HI), (D) kerogen typing from HI and oxygen index (OI). Two different levels of maturity can be observed. Although both cores contain mixture of kerogen types II and III, kerogen from Gill Land 2 core appears to contain more type III by comparison. It is important to note that the higher maturity of Gill Land 2 samples suppresses the kerogen types in B and D above. Plots reference grids are modified from (Finn and Johnson, 2005). 52

Figure 3.20 Vitrinite reflectance levels in reference to hydrocarbons generation and destruction windows. Range of calculated Ro for studied samples are noted with yellow bars. Modified from (Cardott, 2014). 55

Figure 3.21 Summary of the XRD mineralogy for Gill Land 2 core samples. Samples are generally rich in carbonates with variable clay and quartz content..... 56

Figure 3.22 Summary of the XRD mineralogy for Berthoud State 3 core samples. Mineralogy variation is highly correlatable to Gill Land 2 core samples. 57

Figure 3.23 Crossplot of total clay versus quartz content. Positive excellent correlation is observed. Significance level is 0.05, calculated probability is 0.000018. . 57

Figure 3.24 Ternary plot diagram of the XRD data. Reference grid is following the organic mudstone classification scheme (Gamero-Diaz et al., 2013). Plotted data can be interpreted as mixed carbonate mudstone and carbonate-dominated lithotype. 58

Figure 4.1 Compressional velocity from well log compared to core porosity for Gill Land 2 core. Number of samples is 164. P-value is 0.09, therefore correlation has marginal significance when compared to a significance level of 0.05. 60

Figure 4.2 Calculated density porosity curve for the Gill Land 2 core Core. A core-calibration shift was achieved by applying a multiplier value of 0.7 to match the measured core porosity. Both types of core measured porosities are displayed for reference. Dphi was calibrated to WIP porosity specifically as helium is known to underestimate pore volume in tight samples. 61

Figure 4.3 Crossplot of measured (horizontal axis) vs. calculated porosity (vertical axis). P-value of the regression indicate an excellent significance (significance level is 0.05)..... 62

Figure 4.4 Crossplots showing core calibrated porosity for Gill Land 2 core samples versus: (A) Parallel to bedding compressional to shear velocity ratio, correlation p-value indicate good significance. (B) Transverse compressional (C33) stiffness coefficient Both crossplots indicate inverse relationship with porosity. C33 shows weak correlation significance to core-calibrated porosity. C33 coeffecient is dependant on Vp90 and sample denisty. 63

Figure 4.5 Crossplots showing samples of established mineralogy and ultrasonic parameters relationships with significant correlations. (A) and (B) show correlation with very good significance between C33 and calcite volume, and total clays vs. C33 respectively. (C) and (D) show lower significance correlation for C44 vs calcite content, and total clays vs C44 respectively. Four datapoints measured at 3000 psi are presented for reference but were not included in the regression. Pressure effect is observed as an increase in the C33 and C44 for each sample. Numbered samples are as follows: (1) B Chalk- 3013.75 ft, (2) B Marl-3054.1 ft, (3) C Chalk-3077.4 ft and (4) C Marl-3101.9 ft. 64

Figure 4.6 Histogram analysis of the established correlations between SRA data and observed ultrasonic properties. Any correlation with R value between 0.5 and -0.5 was eliminated due to insignificancy. 66

Figure 4.7 TOC effect on C33 (A) and C12 (B) stiffness coefficients. Number of samples= 19. Samples measured under 3000 psi confining pressure are presented. Numbered samples are as follows: (1) B Chalk- 3013.75 ft, (2) B Marl-3054.1 ft, (3) C Chalk-3077.4 ft and (4) C Marl-3101.9 ft. 67

Figure 4.8 C33 vs. (porosity and kerogen content) for multiple source rocks (Prasad et al., 2011). Data for Niobrara from this study are presented in Figure 4.7. 68

Figure 4.9 Vs45 (A), C33 (B) and C44 (B) correlation to S1 values. S1 vs. C44 yielded the highest correlation coefficient. Number of samples is 14. Numbered samples are: (1) B Chalk- 3013.75 ft, (2) B Marl-3054.1 ft, (3) C Chalk-3077.4 ft and (4) C Marl-3101.9 ft. 69

Figure 4.10 Vs/Vp45, Vs90 and DTCO correlation with S2 values. S2 vs. DTCO shows an excellent correlation significance. Number of samples is 14. Numbered samples are as follows: (1) B Chalk- 3013.75 ft, (2) B Marl-3054.1 ft, (3) C Chalk-3077.4 ft and (4) C Marl-3101.9 ft. 70

Figure 4.11 DTCO, Vs/Vp45 and v31 correlations to S3 content. Numbered samples are as follows: (1) B Chalk- 3013.75 ft, (2) B Marl-3054.1 ft, (3) C Chalk-3077.4 ft and (4) C Marl-3101.9 ft. Correlation results are comparable to S2 crossplots in Figure 4.10. 72

Figure 4.12 DTCO, Vs90, Vp90, deep resistivity and Vs45 linear correlations with hydrogen index (HI). Numbered samples are as follows: (1) B Chalk-3013.75 ft, (2) B Marl-3054.1 ft, (3) C Chalk-3077.4 ft and (4) C Marl-3101.9 ft. Number of samples=14. 73

Figure 4.13 Oxygen index compared to Vp/Vs0 ratio. The correlation has fair significance based on number of samples=14. Numbered samples are as follows: (1) B Chalk- 3013.75 ft, (2) B Marl-3054.1 ft, (3) C Chalk-3077.4 ft and (4) C Marl-3101.9 ft. Number of samples=14. ... 74

Figure 4.14 Tmax correlation with C33. Correlation shows weak marginal significance. Numbered samples are as follows: (1) B Chalk- 3013.75 ft, (2) B Marl-3054.1 ft, (3) C Chalk-3077.4 ft and (4) C Marl-3101.9 ft. 74

Figure 4.15 Measured vs. predicted source rock richness (TOC) and maturity: (S2, hydrogen index HI and oxygen index OI) based on lab generated prediction models. Data displayed for Aristocrat PC H11-07 core. Measured data points and core description are courtesy of ElGhonimy (2015). 77

Figure 4.16 Error distribution for predicted TOC and S2 values. 78

Figure 4.17 Error distributions for predicted HI and OI values. 79

Figure 4.18 Predicted TOC by delta log R method compared to core TOC (ElGhonimy, 2015). Three cases were calculated using three different resistivity baselines..... 80

Figure 4.19 core TOC vs spectral uranium and total GR logs. Regressions calculated were used to predict TOC from uranium and total GR logs in ElGhonimy (2015) 81

Figure 4.20 comparison of TOC prediction for Aristocrat PC H11-07 core using: this study method (track1), ElGhonimy (2015) regressions based on core TOC, GR and spectral uranium logs (tracks 2 and 3). The GR estimated TOC is six times higher than the core TOC. Uranium method shows the best fit to core data across the B Marl interval whereas the method from this study provide better accuracy in the C Marl interval. 82

LIST OF TABLES

Table 2.1 Summary table of samples acquired in this study and types of measurements. Data acquired during this study are marked with "x". Previously acquired data were mainly accessed through U.S. Geological Survey Core Research Center - Well Catalog online database (U.S. Geological Survey, 2016). 14

Table 2.2 Cores used for this study and their respective vitrinite reflectance data as a measure of maturity levels. For location see Figure 1.1. 13

Table 2.3 Delay times measured using calibration aluminum sample with known velocities. Delays are presented in nanoseconds. Sample jacket 1 was used for samples 3101.9 and 3077.4, sample jacket 2 was used for samples 3054.1 and 3013.75. 21

Table 2.4 Correlation coefficient threshold for confidence level 0.05 based on different sample sizes (Fisher and Yates, 1953). R-value threshold can be used to determine if the correlation is significant or not (i.e. correlation coefficient must exceed the threshold to become significant based on the specified significance level). 23

Table 3.1 Benchtop measured velocities, sorted primarily by core and secondarily by depth and type of wave velocity measured. Velocities are reported in km/s. Facies and internal structure of each sample is described in the third column. 34

Table 3.2 Summary table for source rock analysis data used in this study. Note: two samples from Berthoud State 3 were not analyzed by pyrolysis. 51

Table 3.3 Average source rock analysis values for the samples sorted by cores. Average was obtained for samples with TOC values of ≥ 1.0 wt% 54

Table A.1 All correlation coefficients between all ultrasonic velocities and stiffness coefficients (rows) and core calibrated porosity for Gill Land 2 core (column). Darker highlight indicates higher R-value. 89

Table A.2 All significant correlation coefficients between all ultrasonic measurements (rows) and all XRD mineralogy (columns). Darker highlight indicates higher R-value 90

Table A.3 All possible correlation coefficients between all ultrasonic measurements and wireline logs (rows) and all source rock analysis measurements (columns). Darker highlight indicates higher R-value. 91

AKNOWLEDGMENTS

I would like to acknowledge my thesis advisor Dr. Steve Sonnenberg for his guidance, support and patience throughout this project. My thesis committee members, Dr. Manika Prasad and Dr. Donna Anderson for their help in formulating and motivating this research. Saudi Aramco for their generous financial sponsorship. OCLASH consortium members: Andre Panfiloff, Cesar Mapeli and Liwei Ou for facilitating the experimental setup and for their support and dedication in making this a successful and safe research. Niobrara consortium and USGS core research center for sharing the core data. My wife Sukaina for her understanding, encouragement and support through this journey. Her endless support made this thesis possible.

CHAPTER 1 INTRODUCTION

The Niobrara Formation was deposited in the Western Interior Seaway basin during Middle to Late Cretaceous. The formation spans northeastern Colorado, eastern Wyoming, northwestern Nebraska and western part of South Dakota. The study area, Wattenberg field, is located in the central part of the Denver Basin, Colorado (Figure 1.1). The field was discovered in 1970 when the J sandstone reservoir unit was completed in gas wells. The field continued to expand rapidly until 2006 when it became the 7th largest US gas producer field. The field currently produces from more than 20,000 active wells targeting multiple Cretaceous reservoirs: Dakota, J Sandstone, Codell, Niobrara Shale/Greenhorn shale and limestone, Sussex and Shannon formations. Two distinctive members can be recognized within Niobrara Formation: Ft. Hays limestone and Smoky Hill Member which consists of high frequency thinly interbedded chalk and marl intervals. Organic richness of the Smoky Hill Member varies between 1-6 wt.%.

Horizontal drilling and hydraulic fracturing activity targeting Niobrara Formation has been increasing for the past four years in the Denver Basin area. This study presents two complete cores of the Niobrara Formation from Wattenberg field, Denver Basin. Both cores are studied for maturity using source rock analysis, mineralogy using X-ray diffraction and multidirectional ultrasonic velocity measurements. Ultrasonic measurements are acquired in benchtop conditions and under multi-stage confining pressure up to 4000 psi at 500 psi intervals. Lab measurements are collected independently from each other on the cores. Lab results were integrated into a model to observe the effect of maturity levels and clay content on acoustic velocities, stiffness coefficients and Thomson anisotropies. Established models are used to predict wireline logs with measured source rock maturity from core samples.

1.1 Objectives and Purpose

Sonic measurements are acquired for numerous wells drilled in the Denver Basin due to demand for porosity and geomechanical characterization. Additionally, both open-hole and cased-hole wireline compressional (and less frequently shear) sonic measurements are commonly available either due to cement quality control (i.e. environmental assurance) and/or the low cost involved. Additionally, the scarcity of core data due to the high cost of coring wells presents a challenge that can only be solved using existing wireline logs or another form of low cost data. Therefore, the objective of this study was to examine elastic and mechanical properties represented by ultrasonic responses of the Niobrara organic-rich chalk and marl

intervals in the Denver Basin and establish: (1) a relationship to clay content, total organic content (TOC) richness and maturity levels, and (2) velocity to porosity relationship. Measurements were acquired in the lab using core plug samples representing variable maturity zones within the Greater Wattenberg Area (GWA). The main output of this study is acoustic properties correlated to TOC and maturity properties, which may be used qualitatively to improve placement of future wells based on previously drilled offset wells. Additionally, once the relationship is established, TOC and other reservoir properties of Niobrara intervals can be modelled from sonic properties and can later be calibrated by core data as field development progresses in the future.

1.2 Project Overview and Dataset

This study investigates acoustic properties variability in response to organic content, clay content and maturation levels. Two complete cores of the Niobrara Formation are used for core sampling and measurements: Gill Land Associates 2 and Berthoud State 3 cores (Figure 1.1). Nineteen cylindrical plugs have been sampled for this study. A third core, Aristocrat PC H11-07, is used for verification of established correlation models. Geomechanical parameters response to confining pressure is also investigated on four plug samples from the Berthoud State 3 core. Intra-core and inter-core pattern variations were also examined. Established correlations allow for a qualitative assessment of TOC content and maturation levels in non-cored, new and previously drilled wells using dipole acoustic logs. To examine elastic properties of the Niobrara Formation, this study integrates different experimental lab results from core samples from Greater Wattenberg area. Samples from each core have been collected in the form of cylindrical plugs (length * diameter = 1.0*1.0 inch for Gill Land Associates 2 core and 1.5 * 1.5 inches for Berthoud State 3 core) parallel to bedding. Horizontally plugged samples allowed for the measurements to be collected at 0°, 45° and 90° to bedding planes. At least one plug was sampled from each sub-member within the Smoky Hill and Fort Hays members. Lab measurements were carried out to collect the following data: (a) compressional and shear static (19 samples) and dynamic (4 samples) ultrasonic velocity measurements and (b) source rock analysis (SRA) for 10 samples was also measured. Wherever applicable, mineralogy (XRD) and SRA data from previous studies on the same cores were integrated in this study to reduce overall cost and time required.

1.3 Study Area

Wattenberg field is located in the central part of the Denver Basin, Colorado (Figure 1.1). The field was discovered in 1970 when the J sandstone reservoir unit was completed in gas wells. The field continued to expand rapidly until it became the 7th largest US gas producer field in 2006. The field currently produces from more than 20,000 active wells targeting multiple Cretaceous reservoirs: Dakota, J Sandstone, Codell, Niobrara Shale/Greenhorn shale and limestone, Sussex and Shannon formations. As of March 2008, daily production was 1.2 billion cubic feet of gas per day (Encana, 2008).

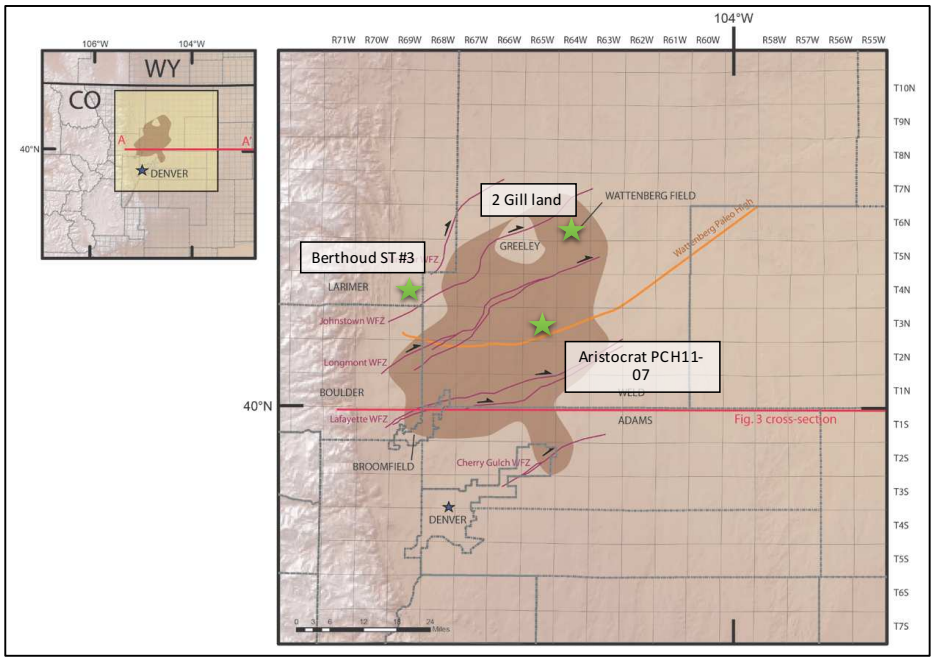


Figure 1.1 Location map of Denver Basin and Wattenberg field (Nelson and Santus, 2011). Location of the main cores used field in the study from Wattenberg are marked. Location of cross section A-A' (Figure 1.2) is also marked.

The Niobrara Formation represents a major transgression within the Western Interior Cretaceous Basin. Stratigraphy of Niobrara Formation in the Denver Basin consists of two members (Figure 1.3): Fort Hays limestone overlain by the Smoky Hill Member. The latter include three transgressive and regressive cycles of chalk and organic-rich marls (Sonnenberg, 2011). Thickness of the chalk beds range from zero to 80 ft. (Figure 1.2) while the organic-rich marls range from 20-150 ft. across Wattenberg field (Weimer et al., 1986).

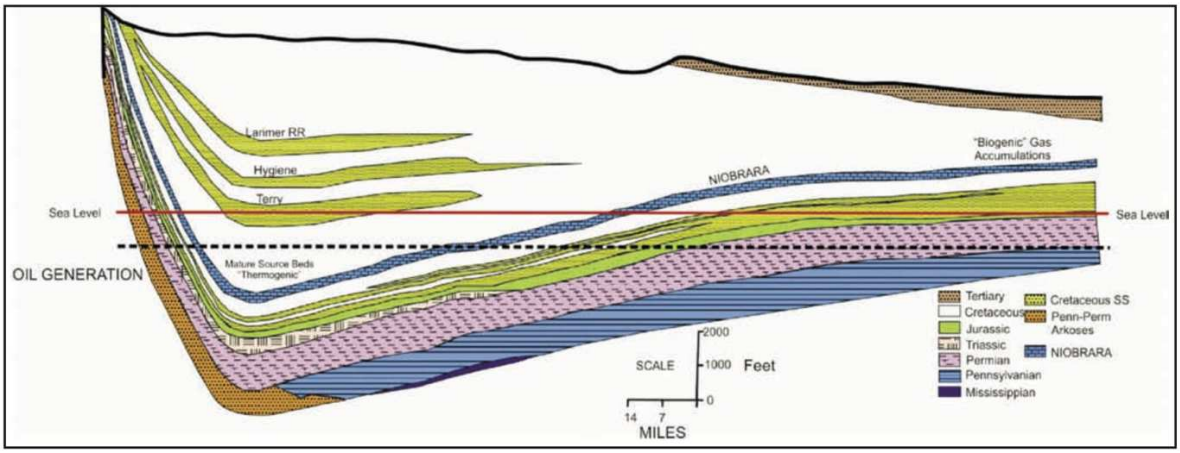


Figure 1.2 East-West cross section of Denver Basin. Niobrara is in the generation window on the western flank but thermally immature on the eastern flank (Sonnenberg, 2011). For location: see Figure 1.1

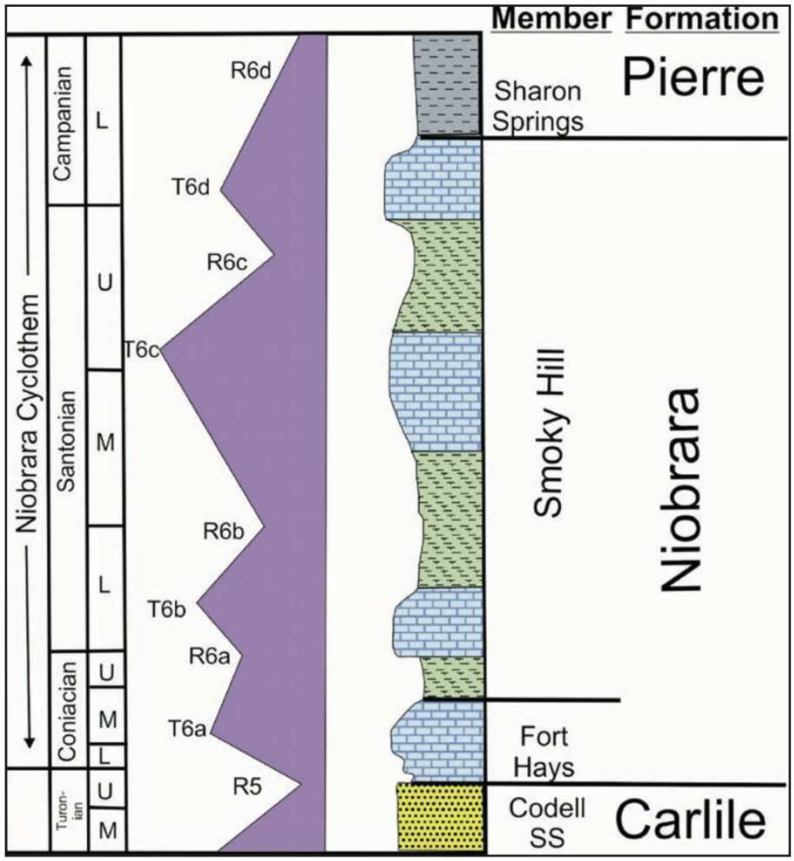


Figure 1.3 Stratigraphic column of the Denver Basin showing Niobrara stratigraphy (Sonnenberg, 2011).

1.3.1 Regional Structural Setting

The Niobrara Formation was deposited in the the Western Interior Seaway (WIS) basin which is an asymmetric foreland basin (Figure 1.2) which characteristically shows steeper dipping stratigraphic units on the western flank compared to the eastern flank (Weimer et al., 1986). The WIS basin was bounded by a fold-thrust belt from the west and the North American craton on the east (Figure 1.4). Sediments were deposited above thick continental crust (Weimer, 1983).

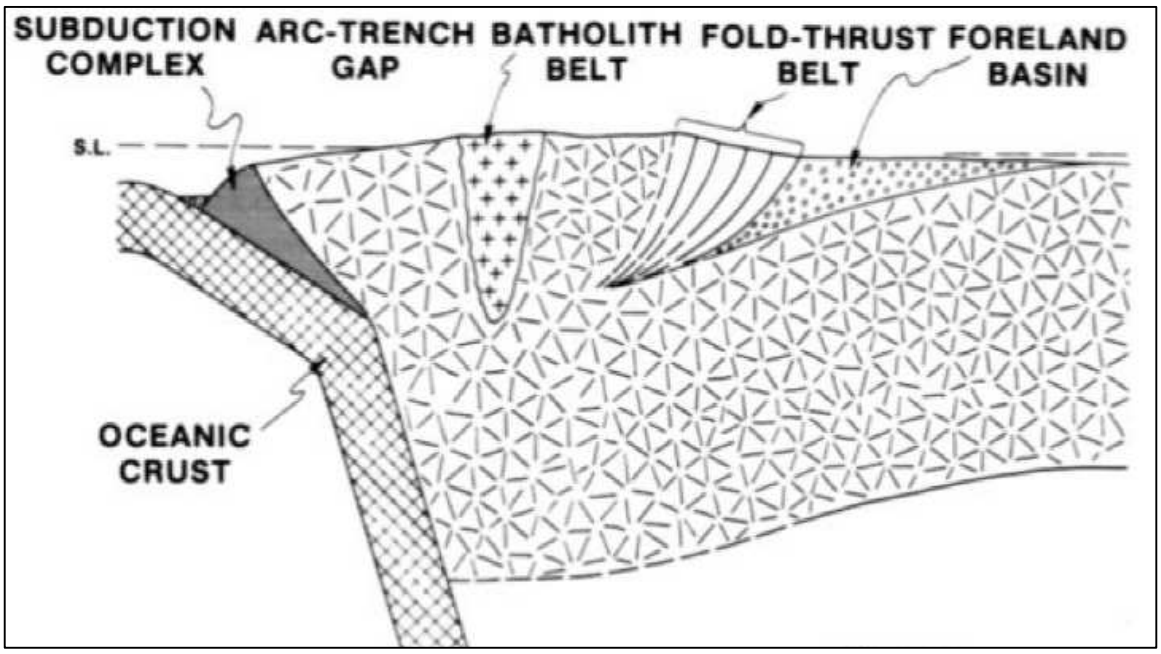


Figure 1.4 Tectonic elements affecting the formation of Western Interior Basin (Weimer, 1983).

Deformation during the Laramide orogeny resulted in the present-day basins as well as controlling much of the uplifts and arches in the Western Interior basin. As a result, the Denver Basin, the focus of this study, axis is aligned north-south parallel to the trend of the Front Range uplift. Most of the structural fields in the basin formed as folds responding to basement faults. Additionally, during deposition of the Pierre shale, Wattenberg area was a paleo high as inferred from thinning of Niobrara Formation (Figure 1.5) (Weimer et al., 1986).

1.3.2 Stratigraphy

The Niobrara Formation represents one of the most widespread carbonate deep carbonate systems within the Western Interior Cretaceous Basin. Niobrara chalks and marls are believed to be a depositional response to paleoclimatic and/or sea level controls. In general,

chalk intervals are linked to warmer sea currents influx combined with relatively higher sea level. In contrast, organic-rich marls are product of shallower water level, land-derived detrital clays and limited vertical water cycling (anoxic conditions), resulting in organic-rich marls (Figure 1.6). Sandstone facies equivalent to the Niobrara Formation exist on the Western side of the basin. Regionally, Niobrara changes laterally toward the east from sandstone to calcareous shale and finally to chalk and marl facies (Sonnenberg, 2011).

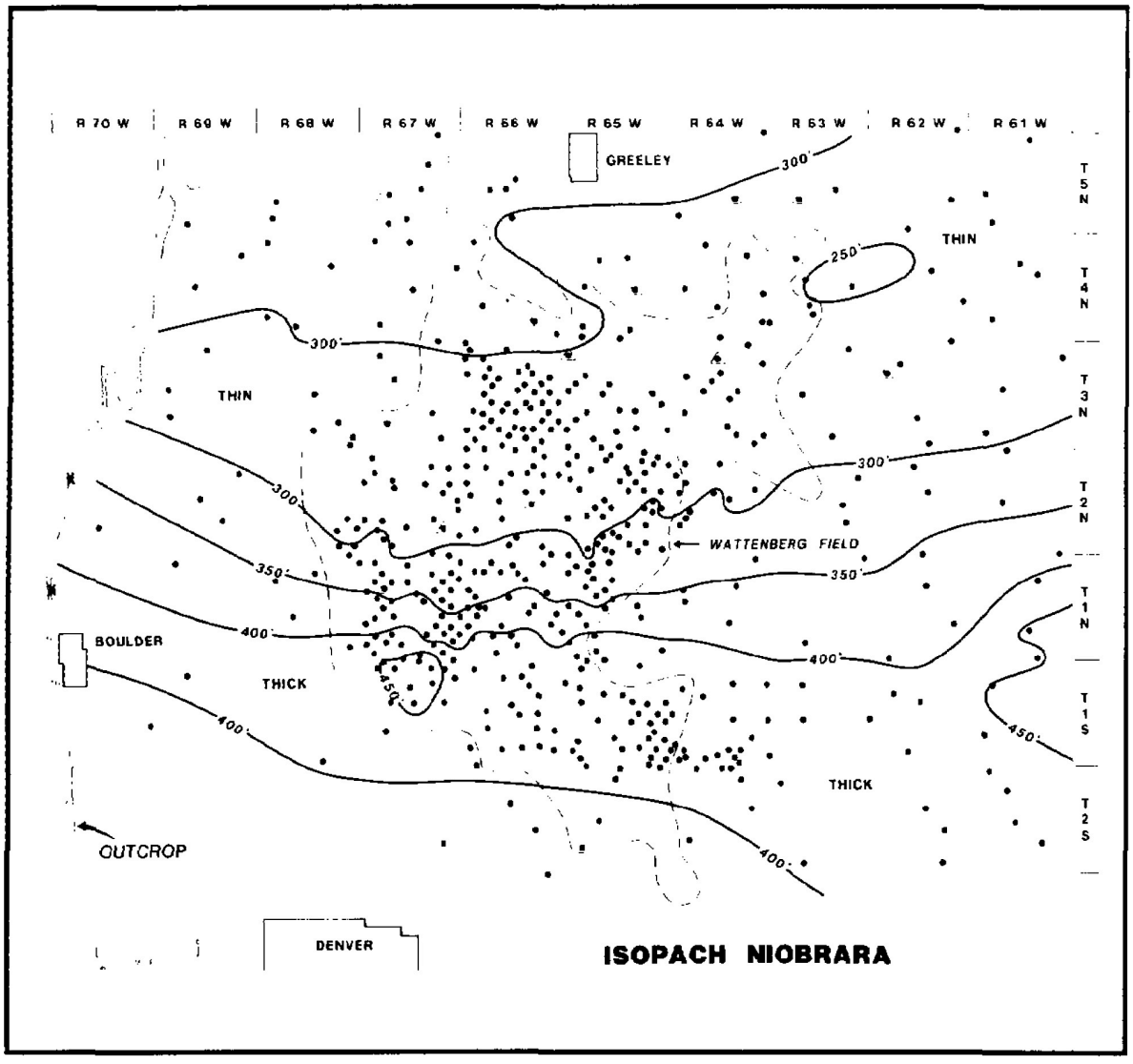


Figure 1.5 Niobrara Isopach map showing thinning of sediments toward the center of Wattenberg structure (Weimer et al., 1986).

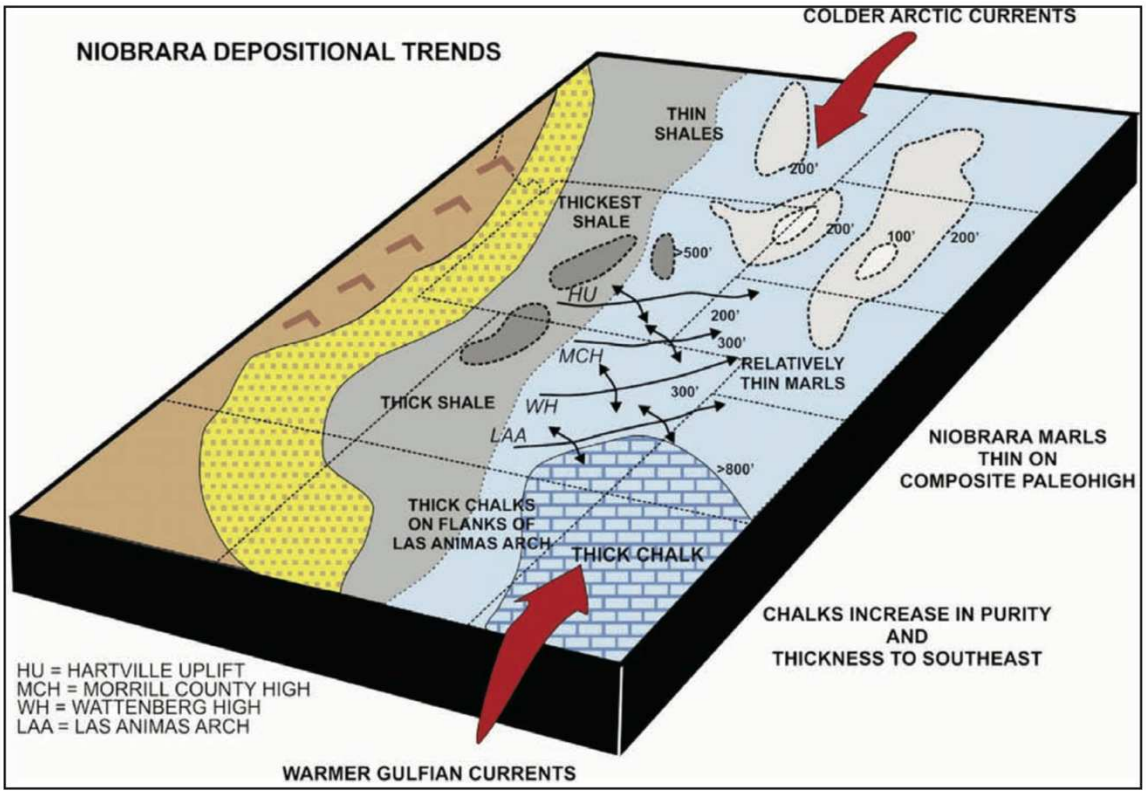


Figure 1.6 Schematic Niobrara depositional model (Sonnenberg, 2011). Paleoclimates and paleohighs played a major role in facies distribution.

While siltstone and shale facies were derived from highlands on the western shorelines, limestone facies of the Niobrara are composed of coccolith-rich fecal pellets, *inocermaid* and oyster shell fragments, planktonic foraminifera tests, micritic mud and clay and silt-sized quartz grains (Sonnenberg, 2011). In general, carbonate content increases toward the southeast, caused by warmer paleoclimates. Total organic carbon (TOC) increases significantly toward the eastern side reaching a maximum value of 8 wt.% and ranging between 1-6 wt.%. In contrast, clay and sand content increase toward west (Figure 1.7) (Longman et al., 1998).

1.4 Previous Work

(Vernik and Nur, 1992) recognized the dynamic elastic properties variance in response to their kerogen levels, maturation states and structurally-induced natural fractures. The strong velocity anisotropy in organic-rich shales arises from the presence of organic layering in addition to their complex nano-pore system geometry. Those characters provide shale with a high contrast in comparison to layers of relatively lower or organic-free content. The strongest velocity anisotropy is present in the bedding-normal direction (Vernik and Nur, 1992). The

authors also noted that anisotropy may be elevated by high pore pressures, liquefaction of kerogen through elevated temperatures, or in certain locations, larger scale layering.

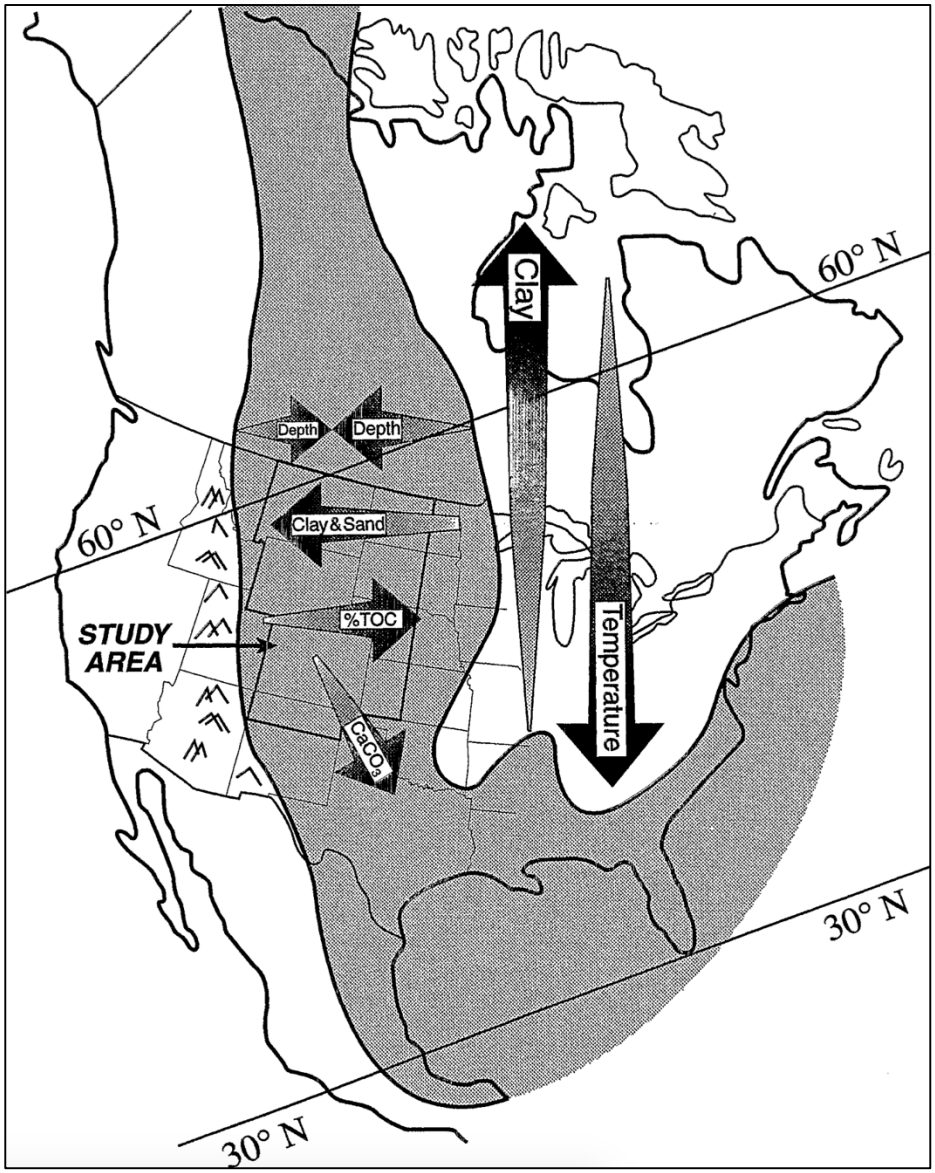


Figure 1.7 Lithological trends within the Western Interior Seaway Cretaceous Basin (Longman et al., 1998).

Vernik and Liu (1997) conducted lab experiments on multiple shale plugs with variable clay, kerogen content and different porosities. Their findings indicated that intrinsic velocity anisotropy does respond to degree of compaction, kerogen concentration and porosity levels. Rock diagenesis plays a very important role due to smectite-to-illite transformation. Vernik and Milovac (2011) compiled a large dataset of organic-rich shales and their respective compressional and shear velocities, some of which are from the Bossier, Woodford and Bakken

shales. They were able to derive bedding-normal matrix compressional stiffness (C_{33m}) equation (equations 1.1 and 1.2) based on volume of clay, kerogen and volume of silt. Their conclusions indicated that bedding-normal elasticity, represented by matrix compressional stiffness (C_{33m}), is primarily related to the kerogen concentration (Figure 1.8) but can also be secondarily correlated to the clay content of the samples (Vernik and Milovac, 2011).

$$C_{33m} = \langle C_{33i} \rangle^{-1} = \left(\frac{v_{cl}}{C_{33cl}} + \frac{K}{C_{33K}} + \frac{1 - v_{cl} - K}{C_{33ncl}} \right)^{-1} \tag{1.1}$$

$$K = \frac{TOC}{C_k} \frac{\rho_b - \rho_f \phi}{\rho_k (1 - \phi)} \tag{1.2}$$

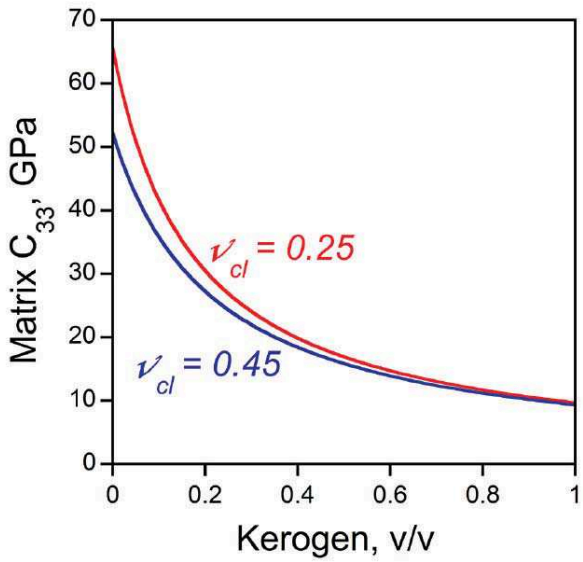


Figure 1.8 Matrix compressional stiffness related to kerogen volume. Two cases of clay content are indicated (Vernik and Milovac, 2011).

Similarly, sonic velocity responds variably based on pore volume and interconnectivity (i.e. permeability) of the examined sample. Alam et al. (2011) concluded, based on samples from the Ekofisk and Tor formations, that if grain specific surface (S_g) of chalk is known, then velocity-porosity and velocity-permeability relationship can be established, enabling the prediction for subsurface chalks porosity and permeability. Although, pore volume magnitude within the Niobrara formation is believed to be much lower when compared to the Ekofisk and Tor formations, porosity effect is still expected to be comparable. Most accurate predictions were achieved by calculating porosity from velocity first and then predict permeability based

on obtained porosity. Grain specific surface (S_g) or flow zone indicator (FZI) can be calculated using the following equations (Alam et al., 2011):

$$FZI = \frac{0.0314}{\varepsilon}\sqrt{\frac{k}{\Phi}} \tag{1.3}$$

$$S_g = S_{BET} \times P_g \tag{1.4}$$

$$S = (1 - \Phi)S_g \tag{1.5}$$

$$S_\Phi = \frac{S}{\Phi} \tag{1.6}$$

Where: *FZI* is flow zone indicator, *k* is liquid permeability, Φ is porosity, $\boldsymbol{\varepsilon}$ is the void ratio, S_g is specific surface of grain, S_{BET} is the nitrogen adsorption technique measurement introduced by Brunauer et al. (1938); P_g is grain density, S is the bulk specific surface and S_Φ is the specific surface with respect to pore volume.

Tensile strength measurements on the Niobrara lower chalk/marl and the Ft. Hays Member using the Brazilian test method show that tensile strength increases with increasing clay content (Maldonado, 2011). The same study measured elastic properties using the triaxial test method on the same interval. Results indicated that Young's modulus decreased with higher gamma readings, responding mainly to the mineralogy of the Niobrara Formation. In contrast, Poisson's ratio was constant throughout the formation. Results show that, with a constant differential pressure, compressional velocity increases linearly as the confining pressure increases. The same property increases logarithmically if the pore pressure is held constant while increasing the confining pressure. In addition, specific to the lower marl test interval, the compressional velocity was evidently higher compared to the vertical velocity (Figure 1.9; Figure 1.10).

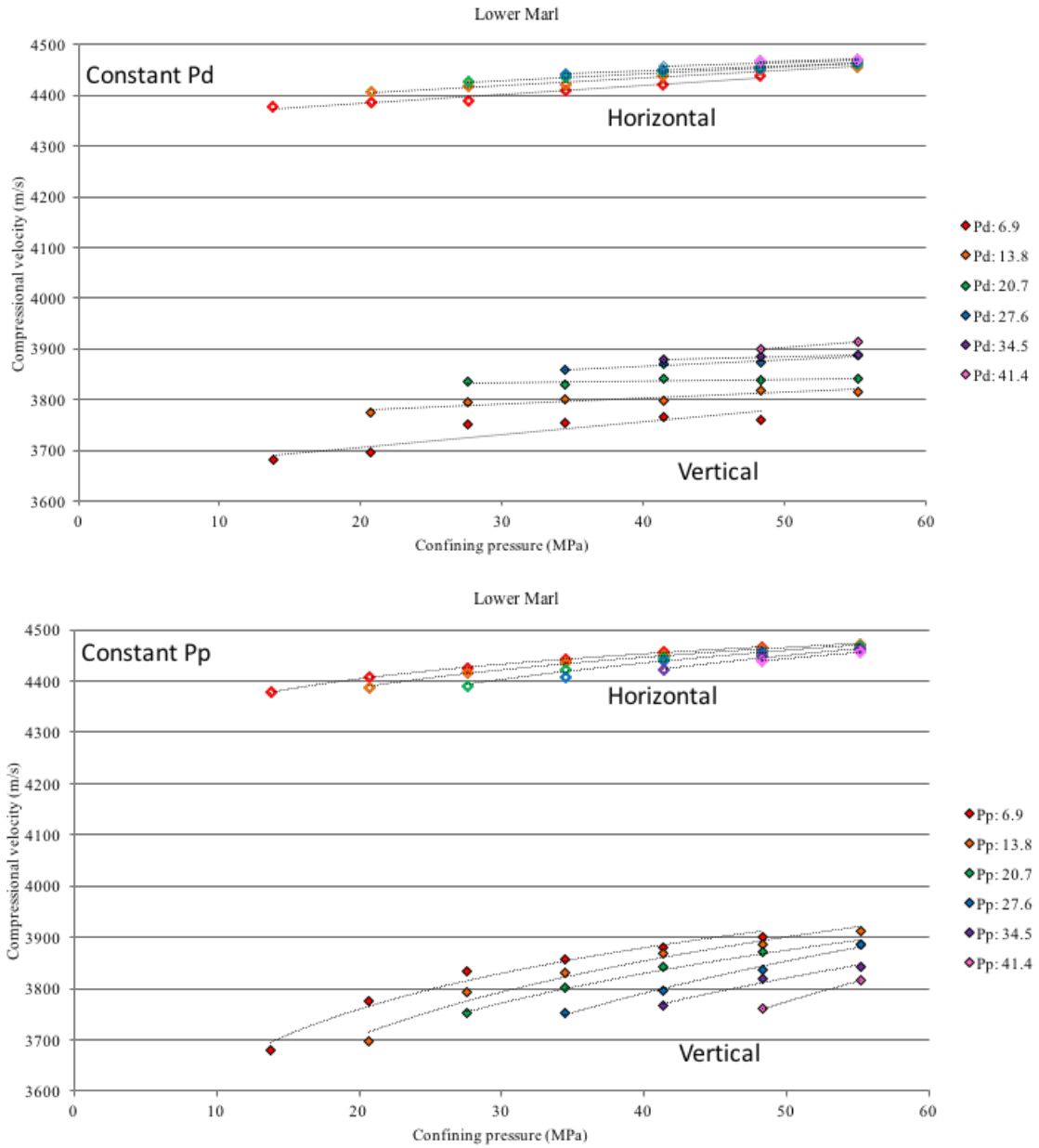


Figure 1.9 Vertical and horizontal compressional velocity as a function of variable confining pressure for the lower marl (Maldonado, 2011). The upper plot represents constant differential pressure, lower plot represents constant pore pressure.

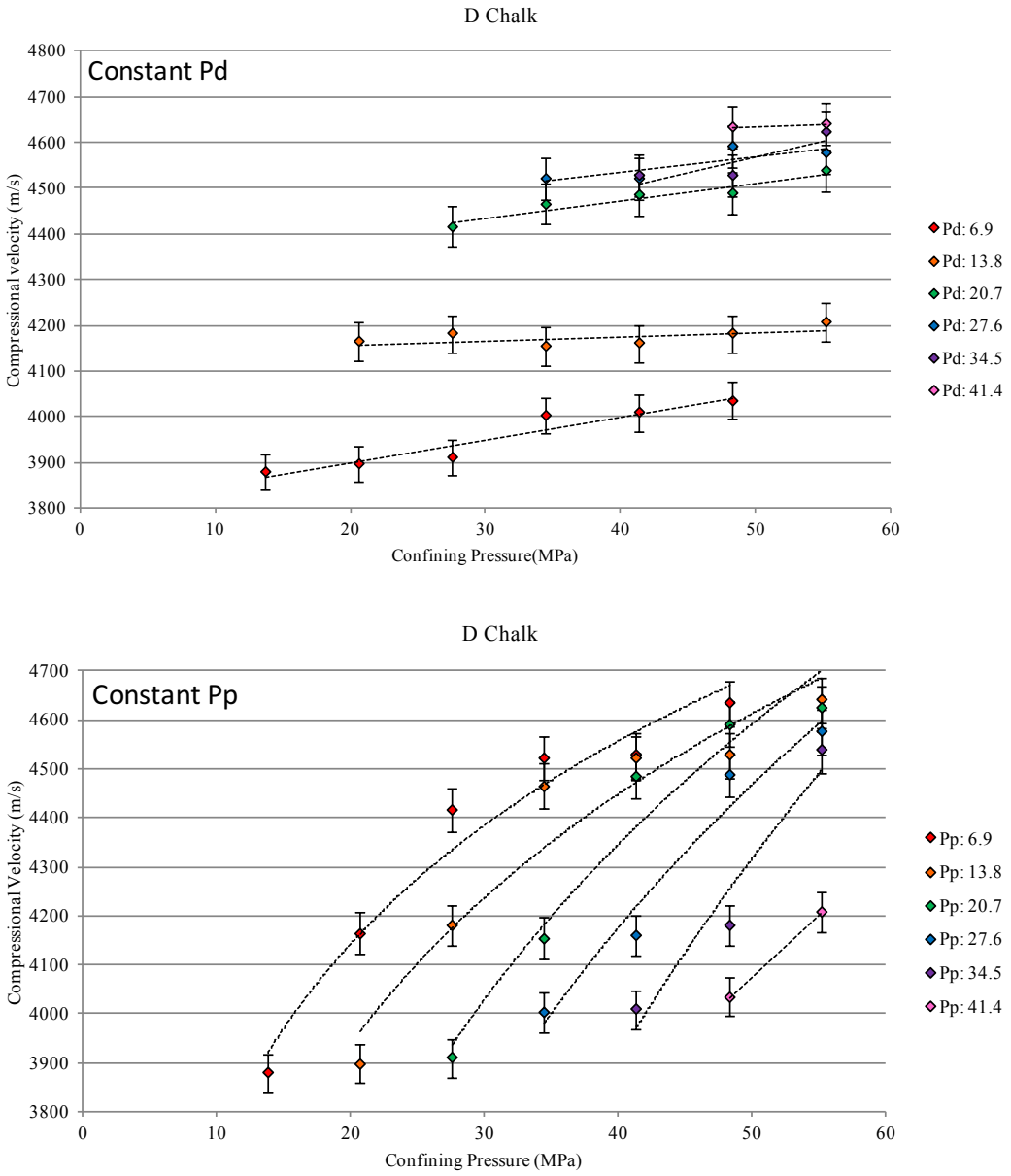


Figure 1.10 Vertical compressional velocity as a function of variable confining pressure for the D chalk (Maldonado, 2011). The upper plot represents constant differential pressure, lower plot represents constant pore pressure.

CHAPTER 2 METHODS

A combination of lab measurements and detailed core description were used to investigate the effects of mineralogy and organic richness and maturity on the elastic properties of Niobrara Formation. The studied cores (Table 2.1) have been previously analyzed for different purposes. Some of the data include previously acquired x-ray diffraction and source rock analysis; where applicable, existing data were incorporated. However, none of these cores have been studied for acoustic purposes. This section will demonstrate theory and procedures for each experimental measurement carried out on the samples. For each experimental data used for this study, see Table 2.2.

2.1 Core Description and Sampling

Three cores were selected within GWA to represent contrasting maturity states (Table 2.1). Prior to sampling, two cores (Gill Land Associates 2 and Berthoud State 3) were described in detail with half foot resolution, Aristocrat PC H11-07 core has been described previously by ElGhonimy (2015) and was incorporated in this study. The primary objective for core description was to capture vertical variability in facies, lithology types, degree of bioturbation, clay content, frequency and presence of natural fractures. Results of the core description were used during sampling to capture texture, facies and reservoir characters of each core plug. Alignment of fabric, lamination or presence of macro fossils are all expected to affect the acoustic velocity in each plug sample.

Table 2.1 Cores used for this study and their respective vitrinite reflectance data as a measure of maturity levels. For location see Figure 1.1.

Core	Vitrinite Reflectance R_0	Source of Test
Berthoud State 3	0.72	Average calculated R_0 Using Tmax (USGS CRC database, 2016)
Gill Land Associates 2	1.36	Average Measured R_o (USGS CRC database, 2016)
	0.92	Average calculated R_o using Tmax
Aristocrat PC H11-07	>1.0	Log-derived vitrinite reflectance contour map of Denver Basin (Smagala et al., 1984)

The focus of this study is to investigate the effects of organic content presence and maturity as well as clay mineralogy on the acoustic response of Niobrara intervals.

Table 2.2 Summary table of samples acquired in this study and types of measurements. Data acquired during this study are marked with "x". Previously acquired data were mainly accessed through U.S. Geological Survey Core Research Center - Web Catalog online database (U.S. Geological Survey, 2016).

Core	Zone	Depth	Ultrasonic Velocity Compressional (P) and Shear (S) at 0°, 45°, 90°		X-Ray Diffraction (XRD)	Source Rock Analysis (SRA)
			Benchtop	Confined Pressure		
Gill Land Associates 2	A-Chalk	6661.92	X		Tanck (1997)	Tanck (1997)
	A-Marl	6698.23	X		Tanck (1997)	Tanck (1997)
	B Chalk	6736.25	X		Tanck (1997)	X
	B Marl	6776.25	X		Tanck (1997)	Tanck (1997)
	B Marl	6791.05	X		Tanck (1997)	Tanck (1997)
	C chalk	6816.67	X		Tanck (1997)	X
	C marl	6851.50	X		Tanck (1997)	Tanck (1997)
	C marl	6855.08	X		Tanck (1997)	X
	D chalk/marl	6880.00	X		Tanck (1997)	Tanck (1997)
	Ft. Hays	6890.47	X		Tanck (1997)	Tanck (1997)
Berthoud State 3	A-Chalk	2936.50	X		Keel (2015)	X
	A-Marl	2984.70	X		Keel (2015)	X
	B Chalk	3013.10	X		Keel (2015)	Keel (2015)
	B Chalk	3013.75	X	X	Dean and Arthur, (1998)	X
	B Marl	3054.10	X	X	Keel (2015)	X
	C chalk	3077.40	X	X	Keel (2015)	X
	C marl	3101.90	X	X	Keel (2015)	Keel (2015)
	D chalk/marl	3164.50	X		Keel (2015)	X
	Ft. Hays	3193.05	X		Dean and Arthur, (1998)	X

Therefore, plug samples were selected carefully from each core to represent the eight different zones within the Smoky Hill and Ft. Hays members (Table 2.2). Additionally, sampling depths were selected based on representativity of the described facies. Lower frequency interstratification was preferentially chosen to reduce uncertainty in acoustic to facies association. Visually identifiable fractured depths were avoided to promote successful plugging. Samples were plugged using an air-cooled drill bit. To enhance the overall contrast of the results, previously studied XRD and TOC analysis results, available through School of Mines or USGS datasets, were integrated during core sampling to ensure enough contrast in TOC and total clays volumes between samples.

2.2 Source Rock Analysis (SRA)

To understand the organic richness and maturity of the samples, core samples were analyzed using in-house source rock analyzer (Model: Weatherford SRA-TPH/TOC) (Figure 2.1). Prior to testing, a sample is prepared by grinding a core chip representative of the same depth of the core plug to powder size using a grinding bowl (Mortar and pestle). Sample powder is measured to an average of 75±10 milligrams (mg) using an enclosed lab weight scale. The sample is then loaded into a vessel. The weight measurement excludes weight of vessel. Samples are loaded on a rotating tray where they can be indexed and referenced to each sample location and weight. The instrument is connected to a computer software through a computer network to capture and interpret data.

The following is the pyrolysis test theory adopted from Tissot and Welte (2013). The sample is heated progressively at a rate of 25°C/minute to 550°C. The first stage of the pyrolysis measures the pre-existing free hydrocarbons in the sample (noted: S1 in mg HC/g rock). The intermediate thermal stage measures the volume of hydrocarbons forming due to thermal pyrolysis (noted: S2 in mg Hc/g rock). The third stage captures the CO2 yielded by the thermal cracking of kerogen (noted: S3 in mg CO2/g rock). TOC is calculated from the combination of the residual organic carbon and the pyrolyzed organic carbon. The temperature at which maximum evolution of S2 hydrocarbons occur (Tmax) is also recorded based on the time and heating rate.

2.3 X-Ray Diffraction Analysis (XRD)

XRD data presented in this study was previously measured by different authors (Dean and Arthur, 1998; Keel, 2015; Tanck, 1997). The following provides an overview of the analysis, adopted from (Cullity, 1956). XRD provides a quantitative analysis of the mineralogy

of the tested sample. Sample must be prepared in powder size. The sample is exposed to an X-Ray generated from a source with a known fixed wavelength such as copper x-ray tubes. Both the incident angle of the diffraction and the intensity are recorded. The measurements can be compared to a table of standard minerals for interpretation (Figure 2.2). XRD response is a function of the internal structure of the minerals, therefore, hydrocarbons and other non minerals cannot be quantified using this method.

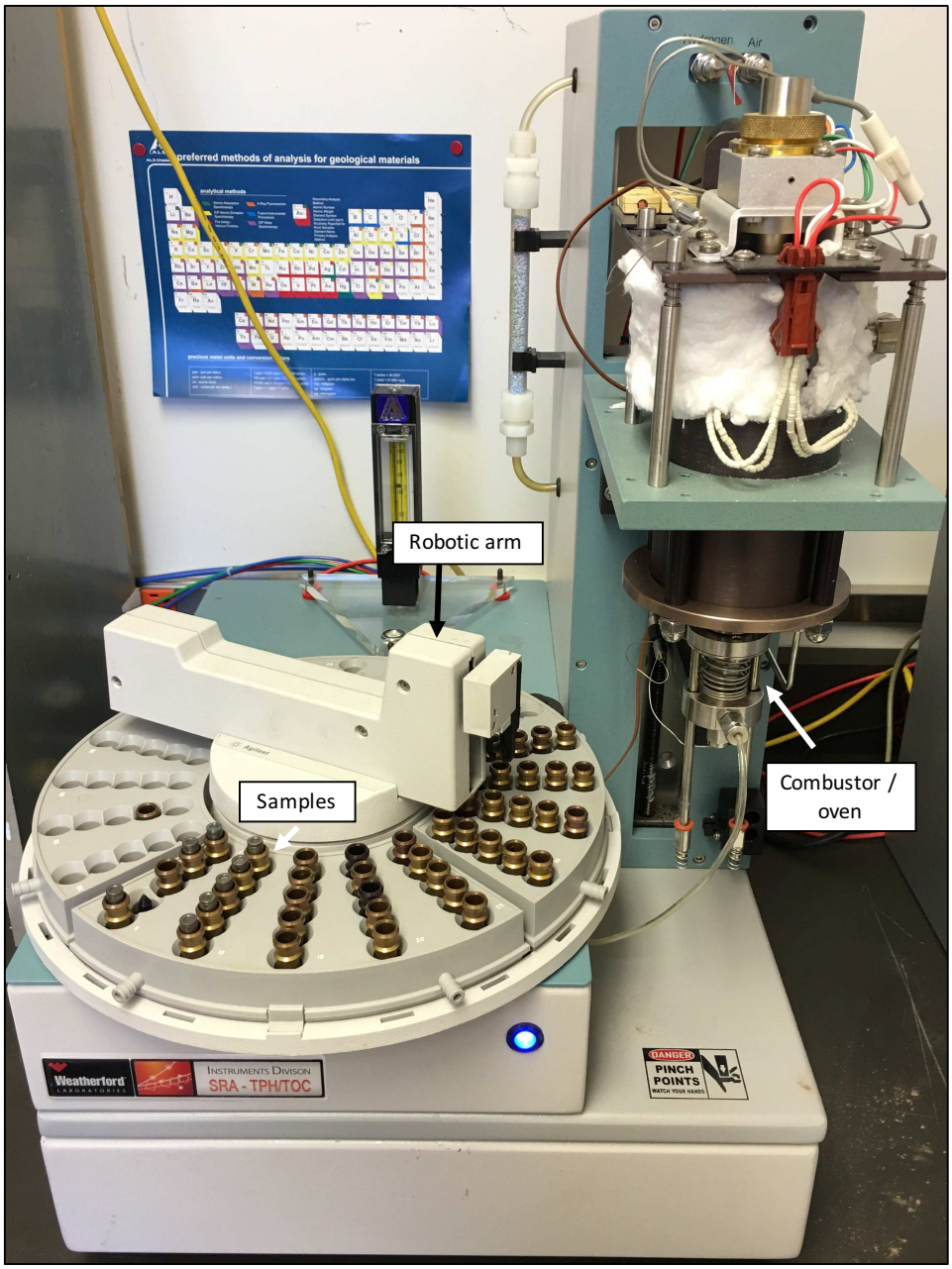


Figure 2.1 Source rock analyzer used for samples analysis

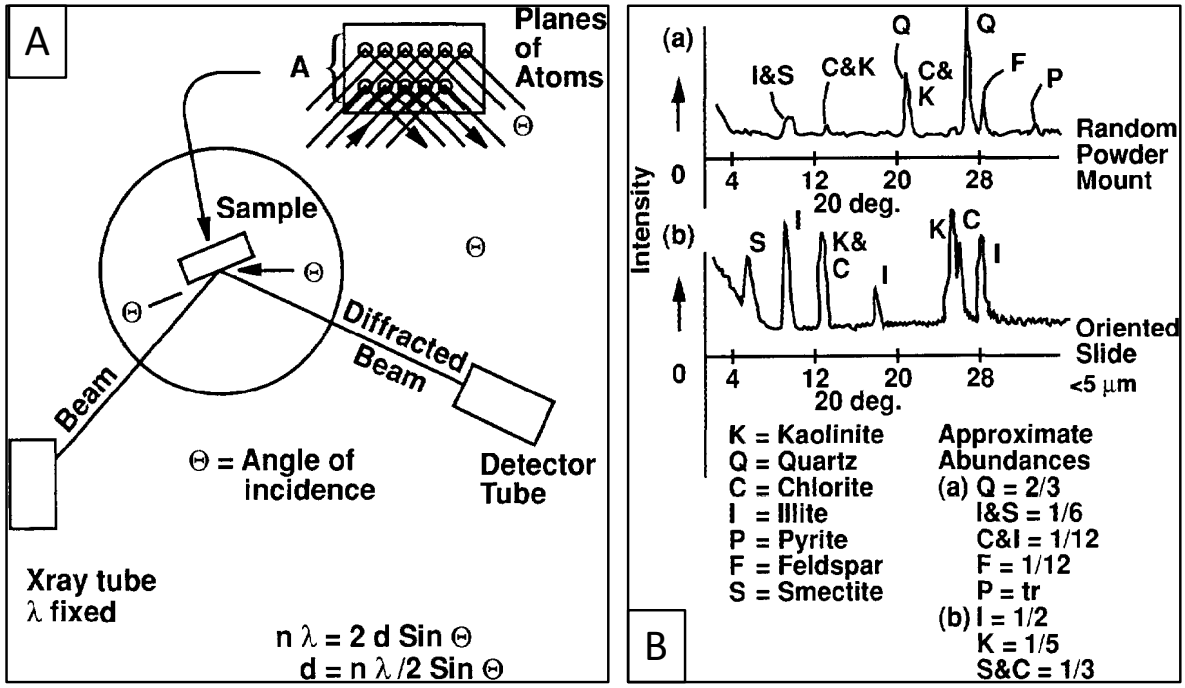


Figure 2.2 (A) schematic diagram for XRD analysis, (B) shows an example analysis results (Cullity, 1956).

2.4 Ultrasonic Measurements

Ultrasonic velocity was measured using the pulse transmission method. In this method, two piezoelectric transducers are used to send and receive an elastic wave signal. The signal is generated by an electric-powered pulser which is connected to the sending transducer. The receiving transducer receives the wave and transforms it to an electrical signal that is recorded by a digital oscilloscope. The digital oscilloscope plots the arriving signal as a wavelet. The oscillator is connected to a computer which facilitates permanent storage of the recorded signal. Two types of wave velocities are measured along three directions. Compressional-wave (P) and shear-wave (S) velocities are measured along bedding plane direction (0°), normal to bedding direction (90°) and at 45° to bedding. The total of six measurements for each sample are measured in two settings. First, at benchtop conditions without any applied pressure, and second, at confining pressure of up to 4000 psi to simulate subsurface conditions. In both techniques, an ultrasonic couplant is applied to ensure efficient transmission of sound energy from transducer to tested sample.

2.4.1 Sample Preparation

Both cores (Gill Land Associates 2 and Berthoud State 3) have been already slabbed prior to this study as part of core handelling. Both cores were fully described in details prior to selection of sampling depths. Both well cores were plugged horizontally parallel to bedding. the Gill Land Associates 2 core plugs were provided by USGS Core Research Center along with core chips (Table 2.2). However, due to logistic limitations, diameter of plugs was limited to 1 inch for the Gill core limiting the acoustic measurements to be carried out in benchtop settings only. The Berthoud State 3 well core slab was available at the Colorado School of Mines Core center. Core plugs were drilled using in-house plugging machine. The diameter for Berthoud core plugs was 1.5 inches. However, due to the nature of the slab, plugs were not flat on one side (Figure 2.3). This was resolved by applying hardened metal epoxy on the bottom of the plug creating a perfect cylindrical plug. This step was crucial due to the sample jacket design limitation which will be demonstrated in section 2.4.3 in detail. The exact dimensions of the plugs are recorded for volumetric and velocity calculation later.

2.4.2 Benchtop

Core plug surfaces are carefully assessed for any abnormal features that may induce unrepresentative measurement. Direction of bedding is carefully noted during the coring process to ensure accurate marking of bedding plane and other corresponding planes of measurements. Benchtop panametric transducers are aligned at both ends of the plane axis (Figure 2.4).Test is repeated along the three directions. First arrival velocity picking was performed using the final recorded signal on a computer using Spectrum Division 2.6g software. Each sample wavelet response is stored on a digital memory for further analysis. Finally, arrival time along with length of tested sample, the distance between transducers (i.e. diameter of measured core sample), are used to calculate each respective velocity using the following equation:

$$\text{Velocity (V)} = \frac{Length\ (L)}{Time\ (T)} \tag{2.1}$$

2.4.3 Confined Pressure Test

The purpose to acquire ultrasonic measurements under confined pressure is to simulate subsurface conditions. For example, naturally occurring fractures tend to have much smaller effect on the final acoustic response under confining pressure when compared to surface

conditions. Therefore, pressurized ultrasonic measurements can be used for several applications such as: core to log correlation and hydraulic fracturing simulations.

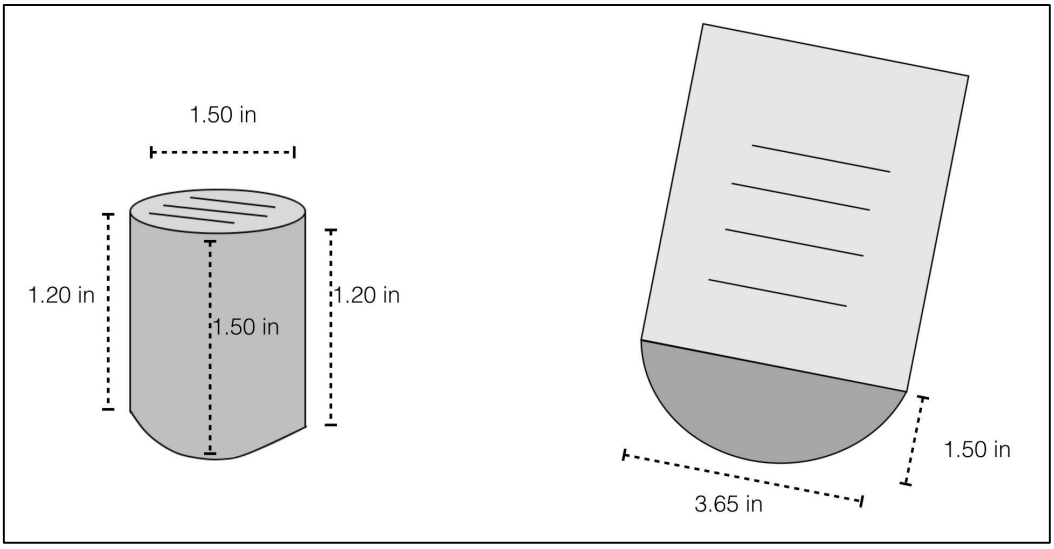


Figure 2.3 shape and dimensions of core slab and plug samples acquired for Berthoud State 3 (Not to scale).

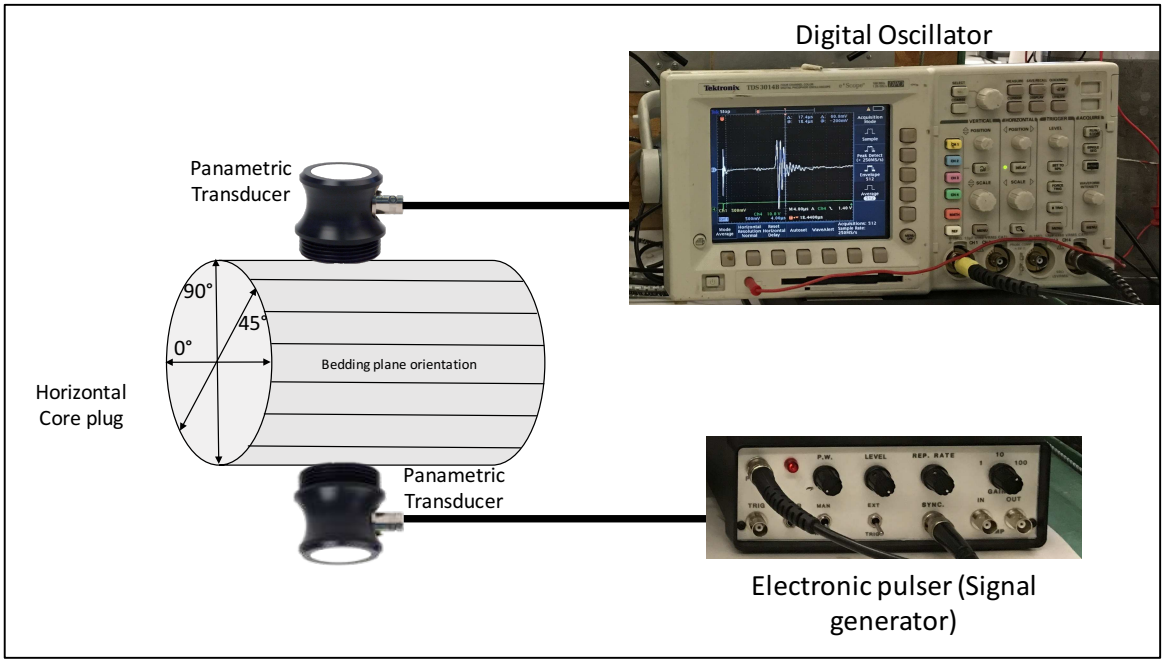


Figure 2.4 Benchtop velocity measurement setup (panametric transducers images are courtesy of Olympus Corporation). Experiment is repeated for each direction. Diagram is not to scale.

In this experiment, the same velocity measurements are acquired while the sample is inside a pressure vessel which provides a controllable confining pressure setting. A sample

jacket is prepared to hold the plug within the vessel (Figure 2.5). The sample jacket was designed originally by Panfiloff (2016). The sample jacket is fitted with 12 transducers: 3 P-wave senders, 3 S-wave senders and on the opposite side a similar count to receive the signals (i.e. 6 receiving transducers). The jacket is used in order to preserve the sample, eliminate the need to install new transducers for each sample, but more importantly, to ensure consistency in running the test and shorten the experiment time significantly.

This section will explain the confined pressure velocity measurement procedure. Before the core can be measured, the sample jacket is calibrated by conducting the measurements on a cylindrical aluminum sample (1.5 inches long and 1.5 inches in diameter). The aluminum sample has known velocities that are measured at benchtop conditions. Additionally, aluminum velocity change with respect to increasing pressure is minimal, therefore, when velocity of the aluminum sample is measured at different pressure conditions, system delay time can be calculated for each pressure stage which will be applied later when testing core plug samples (Table 2.3). The system delay time, measured in nanoseconds, accounts for the time delay of the signal. Delay time is a function of the gap between transducer crystal and measured sample (i.e. jacket wall thickness) and the efficiency of the sending and receiving crystals. This step also allows to test the jacket up to the desired pressure, which was 4000 psi for this study. Once calibration is recorded, the jacket is disassembled for cleaning followed by installing the core sample. Each core sample is tested at benchtop conditions prior to placement in pressure vessel. Once the sample is inside the pressure vessel, velocities are measured at the following pressure points: 0, 250, 500, 1000, 1500, 2000, 2500, 3000, 3500 and 4000 psi. The same measurements are repeated while pressuring down in reverse order in order to capture any changes in velocity behavior (i.e. pressure vs. velocity hysteresis). The pressure in the vessel is controlled by a mechanical pressure pump with a digital controller. Automotive oil is used as a pressurizing fluid and supplied through a confining pressure line. The pressuring rate was controlled at 15 psi/minute during this experiment. This ensures enough time for the sample and jacket to react naturally to the increasing pressure. When replacing a sample, the jacket is inspected thoroughly for any oil leaks from the pressure vessel into the sample jacket. The same procedure is repeated for the next sample. After testing the first two samples, an oil leak was found between transducer and jacket wall which resulted in poor signal quality. The transducing crystals were replaced completely and a new epoxy was applied to avoid any future leakage. A new calibration was measured prior to proceeding with the rest of samples.

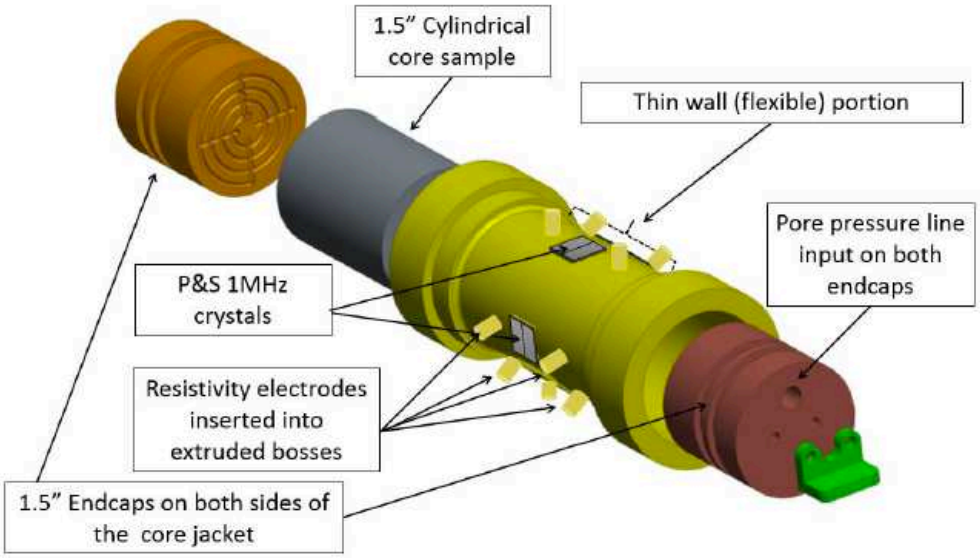


Figure 2.5 Sample jacket design, courtesy of (Panfiloff, 2016), used for confined pressure velocity measurements. Due to limitations on core plug sample size, resistivity measurments were not collected. Pore pressure line was isolated using a screw plug.

Table 2.3 Delay times measured using calibration aluminum sample with known velocities. Delays are presented in nanoseconds. Sample jacket 1 was used for samples 3101.9 and 3077.4, sample jacket 2 was used for samples 3054.1 and 3013.75.

Direction	Sample Jacket 1		Sample Jacket 2		Aluminum sample Velocity (km/s)
	0 psi	250-4000 psi	0 psi	250-4000 psi	
	Delay times in nanoseconds (ns)				
Vp0°	1019	979	1070	970	6.392
Vp45°	1032	1024	1070	1010	6.388
Vp90°	1039	995	1055	1050	6.379
Vs0°	2010	1963	2370	2300	3.121
Vs45°	2110	2065	2360	2310	3.124
Vs90°	2185	2110	2375	2320	3.092

2.5 Statistical Analysis

In order to determine possible correlation between the measured velocities, calculated mechanical parameters and core analysis data (organic content and maturity, and mineralogy), Pearson's product-moment correlation coefficient (Pearson et al., 1929) is calculated. Pearson's correlation coefficient (R-value) is the covariance of two variables (e.g. velocity and porosity) divided by the product of their standard deviations. R is calculated using the equation:

$$R = \frac{\sum XY - \frac{(\sum X)(\sum Y)}{n}}{\sqrt{\left(\sum X^2 - \frac{(\sum X)^2}{n}\right)\left(\sum Y^2 - \frac{(\sum Y)^2}{n}\right)}} \quad (2.2)$$

Where: X and Y are the examined variables, n is the number of samples.

To establish the correlation significance, a probability (P-value) is obtained using t test statistical tables. P value rely on the degrees of freedom and the t-statistic value, both of which are calculated according to the following equations:

$$\text{degrees of Freedom} \qquad (df) = n - 1 \quad (2.3)$$

$$\text{t statistic} \qquad t = \frac{\bar{X} - \mu_0}{\sigma/\sqrt{n}} \quad (2.4)$$

where: n is number of samples, $\bar{X}$ is sample mean, μ_0 is the population mean and σ is the sample standard deviation. Once the p-value is calculated, it can be used to test the correlation for significance by comparing p value to an established significance level (alpha). For this study and the most widely used alpha value in scientific research is 0.05. This means if p value is less than 0.05 then the null hypothesis is rejected and the correlation has a certain level of significance. Alternatively, if p is more than 0.05, then the null hypothesis can not be rejected and therefore, the correlation is not significant. Additionally, if p is >0.1 then the correlation is considered not significant, if p<0.1 then the correlation is considered of a marginal significance, if p<0.05 then the correlation has fair significance, p<0.01 then the correlation has good significance and finally if p<0.001 the correlation is interpreted to have an excellent significance. Pearson's R-value thresholds based on variably sample size (Fisher and Yates, 1953) can be found in Table 2.4.

Table 2.4 Correlation coefficient threshold for confidence level 0.05 based on different sample sizes (Fisher and Yates, 1953). R-value threshold can be used to determine if the correlation is significant or not (i.e. correlation coefficient must exceed the threshold to become significant based on the specified significance level).

Number of Samples	R threshold if confidence level=0.05	Number of Samples	R threshold if confidence level=0.05
2	0.9	17	0.4821
3	0.99692	18	0.4683
4	0.95	20	0.4438
5	0.8783	22	0.4227
6	0.8114	27	0.3809
7	0.7545	32	0.3494
8	0.7067	37	0.3246
9	0.6664	42	0.3044
10	0.6319	47	0.2875
11	0.6021	52	0.2732
12	0.576	62	0.250
13	0.5529	72	0.2319
14	0.5324	82	0.2172
15	0.5139	92	0.205
16	0.4973	102	0.1946

CHAPTER 3 RESULTS

This chapter will present the results from the core description, experimental results from ultrasonic velocity measurements and source rock analysis in detail. Each data category below was acquired independently. Observations will be discussed in the following chapter.

3.1 Cores Sedimentology

Two cores were described in detail. The Berthoud State 3 core captures the full Niobrara section, 283 ft thick, from Berthoud Field and includes 3.5 ft from the underlying Codell Sandstone Member of the Carlile Formation and 4 ft from the overlying Sharon Springs Member of the Pierre Shale (Figure 3.1). The Gill Land Associates 2 core, 239 ft thick, was missing the base of Ft.Hays Limestone Member and the top of A-chalk sub-Member (Figure 3.2). Due to lack of macro sedimentary structures, facies within the Smoky Hill Member within the Niobrara Formation were classified mainly based on a gray-scale visual analysis of clay vs. chalk content (Figure 3.3). Other descriptive parameters from core description such as pellet index and bioturbation index were also recorded using an abundance scale with range of 0-5, with 5 representing most abundant and 0 representing total absence. SEM and thin sections were studied to identify micro-bioclasts.

3.1.1 Facies Analysis

Types and distribution of sedimentary facies in each core was investigated. Eight facies were recognized while describing the cores:

Bioturbated Sandstone: fine to medium sandstone with muddy matrix. Mostly horizontally and vertically bioturbated with bioclastic fragments. This facies is limited to the Codell Sandstone Member of the Carlile Formation and exists only in the Berthoud State 3 core. Preserved sedimentary structures include low angle cross stratification and horizontal laminations. Estimated core porosity range is 5-17%. Clay content is variable but visually estimated at 5-10%. This facies is interpreted to be of a marine shelf origin.

Bioclastic Limestone: bioclastic wackestone to mud-lean packstone, mainly vertically burrowed. Preserved sedimentary structures include very fine mud drapes. Clay content is very low. Bioclasts include inoceramid and oyster shell fragments and other undifferentiated biofragments that are up to 2 inches in size. Pyrite inclusions are moderate to common. Horizontal stylolites are very common at bed boundaries and within individual beds. This facies is only observed within the Ft. Hays Member.

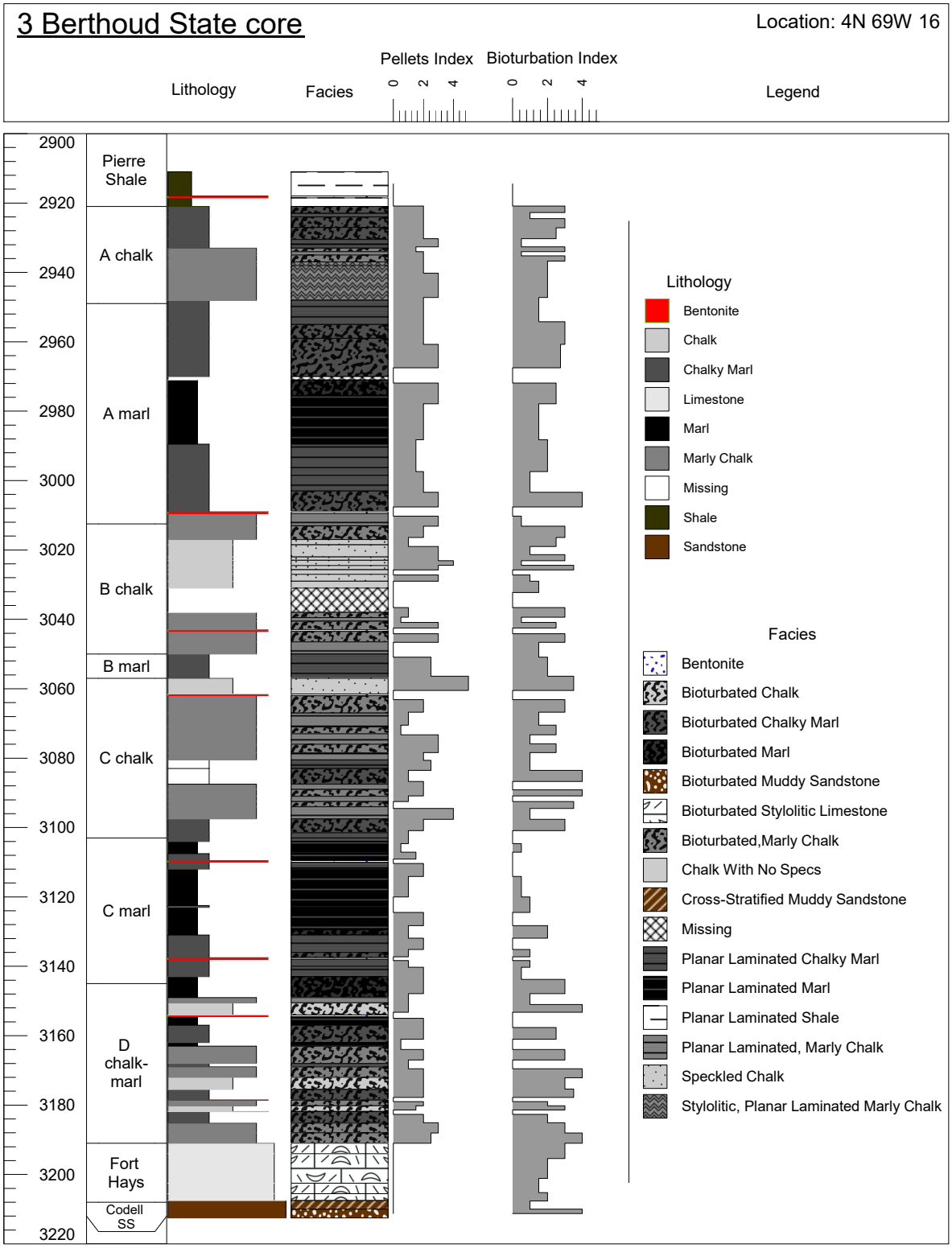


Figure 3.1 Core description and formation tops for Berthoud State 3 core. For location see Figure 1.1

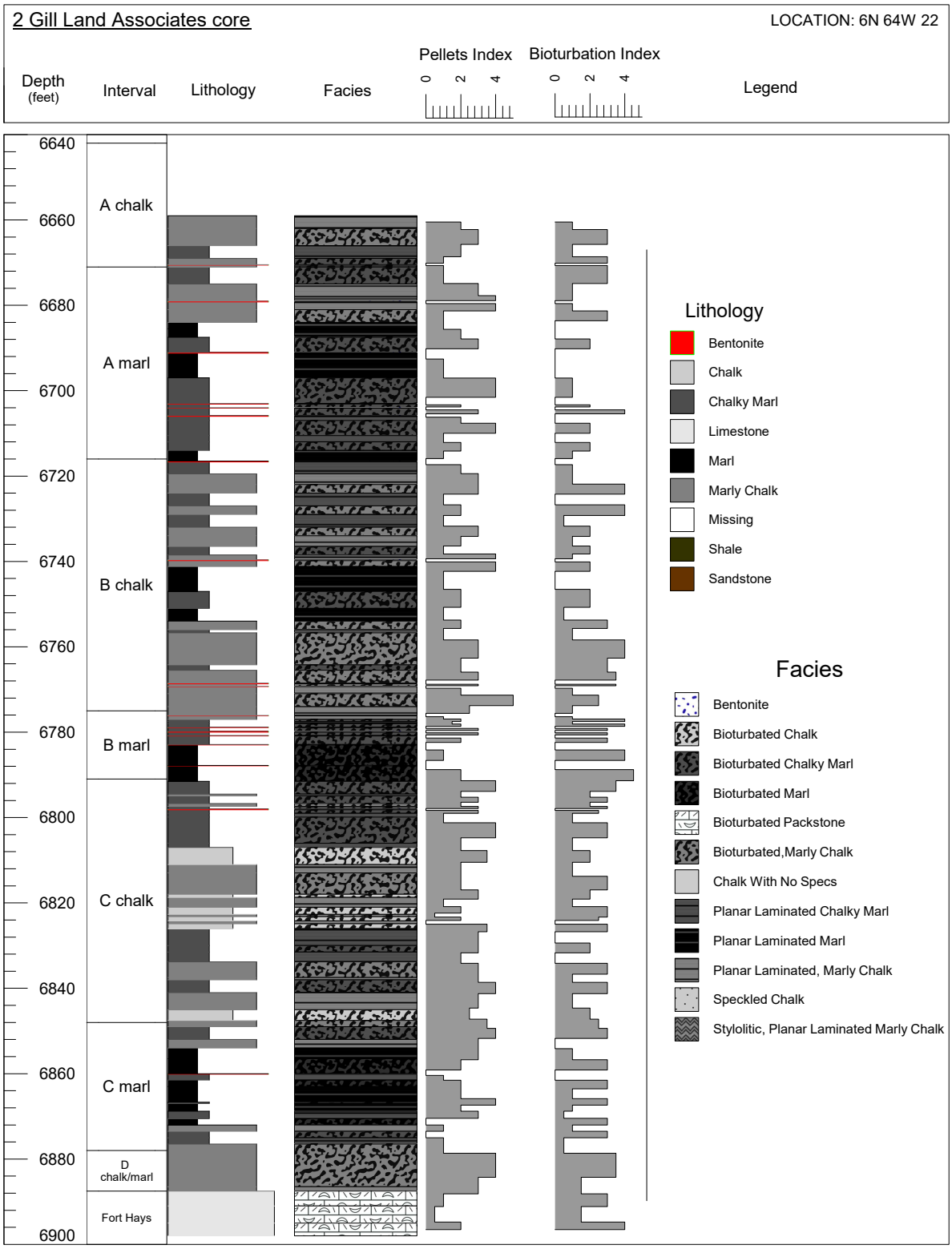


Figure 3.2 Core description and formation tops for the Gill Land Associates 2 core. For location see Figure 1.1



Figure 3.3 Facies samples from Gill Land Associates 2 core. (A) Weakly bioturbated marl (depth: 6707 ft). (B) Horizontally stratified pelletal chalky marl (depth: 6739 ft). (C) Moderately bioturbated marly chalk (depth: 6851ft). (D) Highly bioturbated bioclastic chalk (depth: 6845 ft). (E) Bioturbated bioclastic limestone (Depth: 6890.4 ft). For location see Figure 1.1.

Marl: mudstone to foram, pellet wackestone. Pellets size range between 0.01-0.2 mm. This facies is characterized by very high clay content with none to very low chalk content. It can be described as silt to very fine chalk with pellets floating in matrix of clay-rich carbonates.

Where bioturbation is absent, planar stratification is faintly observed by a horizontal alignment of chalk pellets. Bioclastic fragments are very rare to moderate. Bioclasts include undifferentiated uniserial and biserial *foraminiferas* (Figure 3.4) that are less than 0.5mm in size.

Chalky Marl: low to moderate chalk content. Commonly, it contains higher pellet index, 1-3 using the abundance scale, and increased bioclastic fragments with notable presence of macro *inoceramid* shell fragments (Figure 3.5) and low abundance of undifferentiated uniserial *foraminifera.* Average size of *foraminifera* is 0.05mm. Pyrite may be present as replacement or framboids.

Marly Chalk: bioclastic mud-rich packstone to wackestone. Moderate to high chalk content. Moderately bioturbated. Semi abundance of chalk pellets (2-4). Bioclastic fragments are very common. Bioclasts include: macro *inoceramid* shell fragments, undifferentiated uniserial and biserial *foraminiferas*. Size of *foraminiferas* range between 0.04-0.5mm in size. Larger vertical fractures seem to be commonly associated with this facies.

Chalk: bioclastic pelletal packstone/wackestone with very low clay content, characterized by very light grey color. Bioclasts include *coccospheres*, cocolith fragments and large undifferentiated biserial *foraminiferas* that are up to 0.9mm in size (Figure 3.4). Moderate to very high pellet index. Extensive bioturbation leading to rarely preserved horizontal stratifications.

Bentonite: clay to silt size volcanic ash beds. Modified diagenatically by pyrite replacement (Figure 3.5). Characteristically greenish yellow in color and thinly bedded. Thickness range between 0.1-1.75 inches.

Shale: clay to mud size shale. Parallel lamination is abundant with high frequency. Bioturbation is rare to absent. Clay content is very high. This facies is limited to the Sharon Springs Member of the Pierre Shale Formation.

Facies distribution (Figure 3.6) across Niobrara members revealed the following: (1) both cores show high frequency cycles of interstratified chalks and marls with variable chalk and clay content; (2) expected pattern of increasing chalk dominated facies within chalk members whereas marl members show higher percentage of marl dominated facies; (3) Weak correlation between chalk content and bioturbation; (4) Chalk pellets density and bioturbation index can be very useful in distinguishing facies. Although high heterogeneity exists across different cores, geomechanical, acoustic behavior and petrophysical logs are still correlatable.

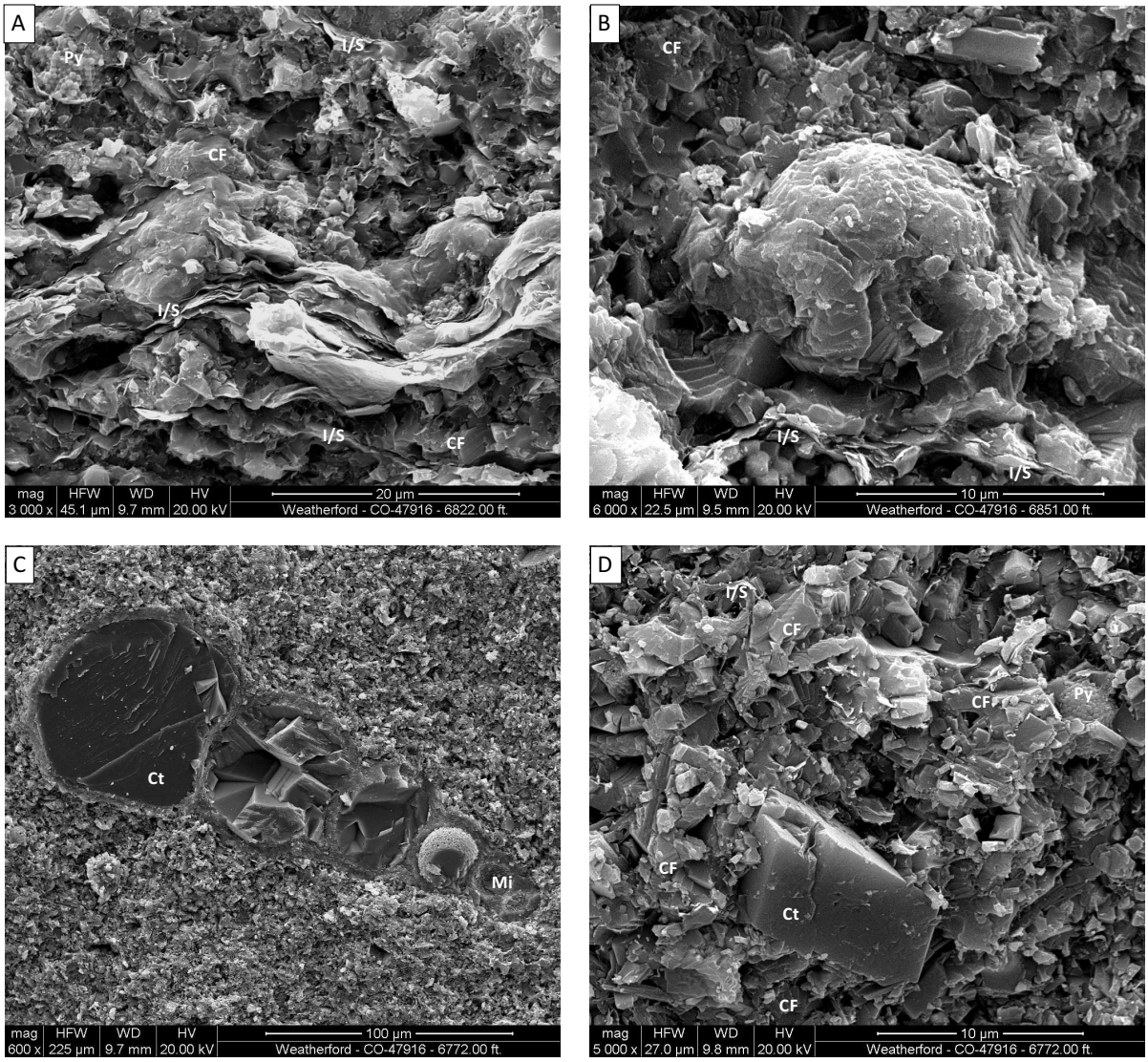


Figure 3.4 Scanning electron microscopy images (SEM) of four samples from Gill Land 2 core. (A) clay rich marly chalk sample from the C-chalk showing a clay-lined pyrite framboid (Py), cocolith fragments (CF) and abundant interlayered illite and smectite clays (I/S). (B) well preserved Coccosphere surrounded by cocolith fragments and interlayered illite/smectite. (C) undifferentiated uniserial foraminifera, chambers display multiple patterns of cementation: calcite crystals (Ct) and micrite (Mi). (D) chalky marl sample showing microfractured calcite crystal, cocolith fragments and pyrite framboid.

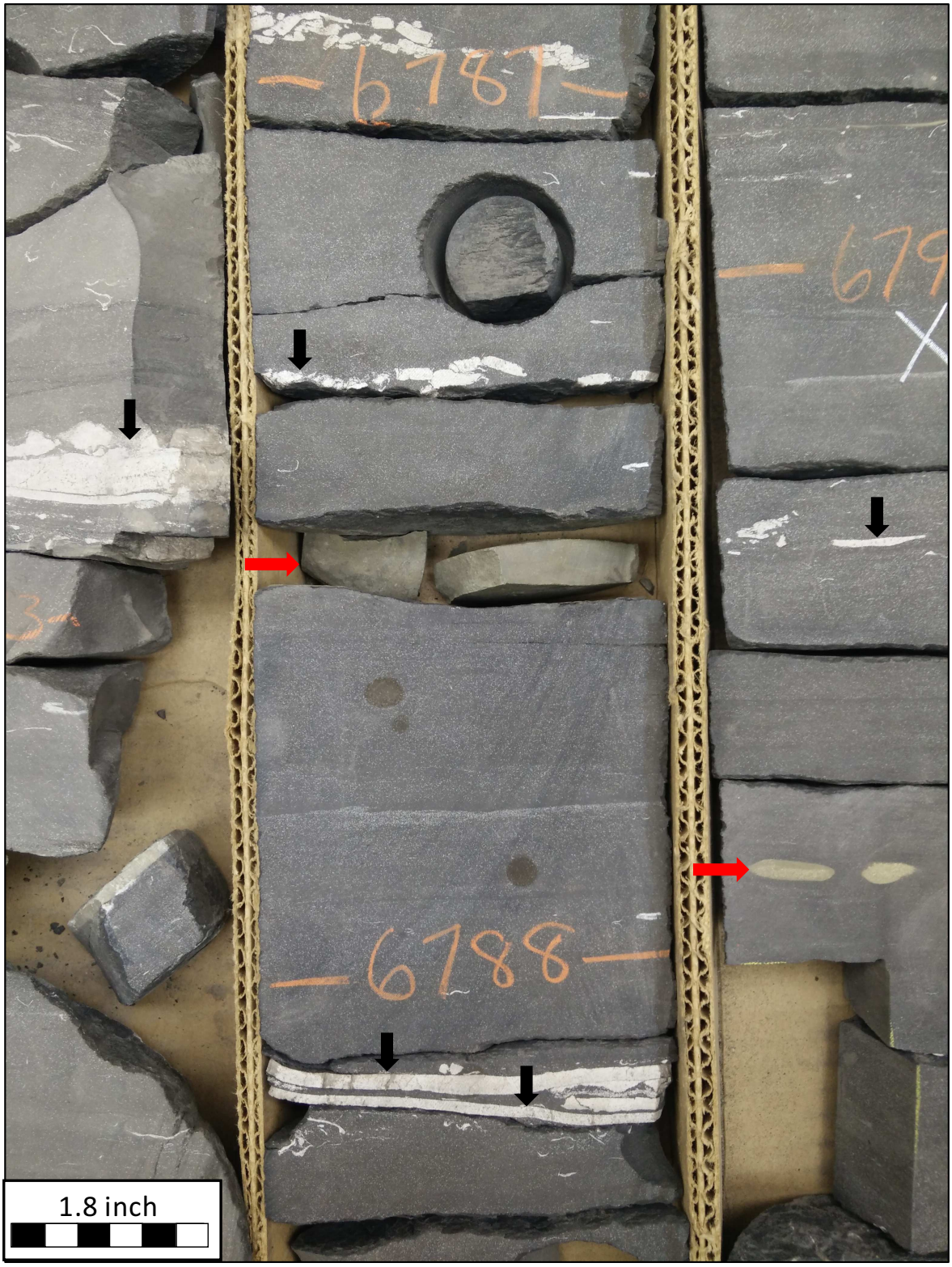


Figure 3.5 Core sample from Gill Land Associates 2 core. Black arrows mark macro *inoceramid* fragments. Red arrows highlight pyritized ash beds (Bentonites). For well location see Figure 1.1

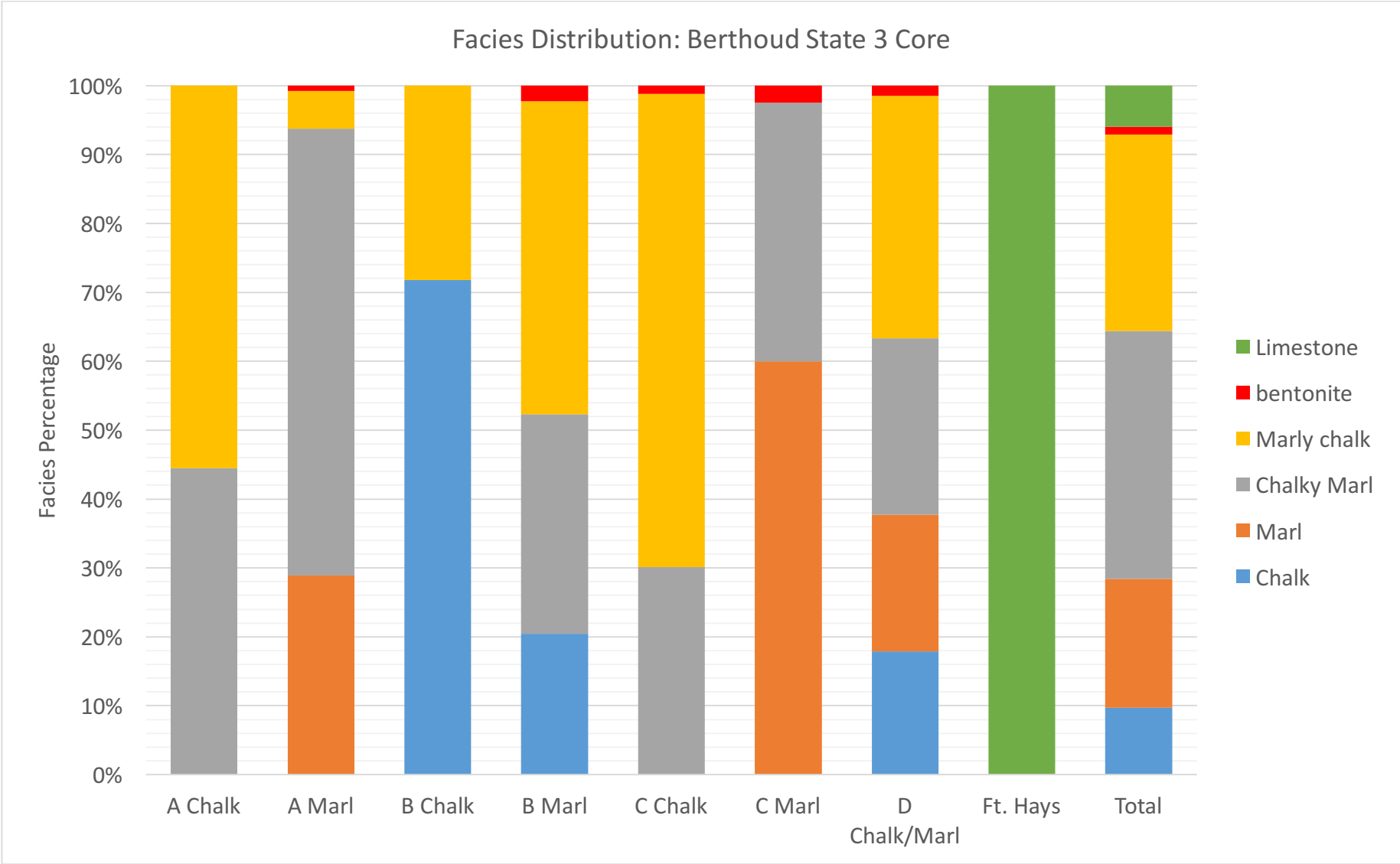


Figure 3.6 Sample facies distribution for studied intervals. Data shown for Berthoud State 3 core.

3.2 Ultrasonic Velocity Measurements

Multidirectional compressional (P-wave) and shear (S-wave) velocities were measured for 19 cylindrical core plug samples. Benchtop velocity (i.e. benchtop pressure conditions) was measured on all 19 samples whereas velocity under confined pressure, up to 4000 psi, was measured for 4 samples only from the Berthoud State 3 core. The four samples represent B chalk, B marl, C chalk and C marl. Source rock analysis and XRD mineralogy measurements were conducted independently using powdered core chips. Velocity was picked using the first-arrival method on the acquired wavelets in three directions (Figures 2.4 and 3.7): parallel to bedding (Vp0° and Vs0°), 45° to bedding (Vp45° and Vs45°) and normal to bedding (Vp90° and Vs90°). The ultrasonic velocities results will be presented in the following sub-sections.

3.2.1 Benchtop Velocity

Benchtop velocities were measured for all the samples from both cores. Delay times were measured for this experiment. The measured delay times are: 172 nanoseconds for P-wave velocity and 268 nanoseconds for S-wave velocity. Benchtop results are presented in Table 3.1. Velocity varied between 0.674-5.528 km/s. The average velocity was 3.174 km/s. Both compressional and shear wave velocities were highest at the direction parallel to bedding, lower at 45° to bedding and lowest at normal to bedding angle. The shear equivalent of the compressional velocity was on average twice as slow (i.e. $V_p=2*V_s$). A clear slowness was observed in the 45° and 90° directions compared to the bedding plane parallel velocity for all the samples in general. However, sample 3077 shows much lower contrast between the different directions.

3.2.2 Confined Pressure Velocity

The same measurements were recorded for four samples from the Berthoud State 3 core under confined pressure. The four samples tested represent B chalk, B marl, C chalk and C marl from the Smoky Hill Member within Niobrara Formation in Berthoud State 3 core Multidirectional compressional and shear wave velocities were measured at nine increasing pressure stages between 0-4000 psi in increments of 0, 250, 500, 1000, 1500, 2000, 2500, 3000, 3500 and 4000 psi. The same measurements were collected in reverse order while pressuring down to capture any changes in rock acoustic behavior due to pressuring. Delay times for each jacket used were measured and are presented in (Table 2.3). Results are presented in Figure 3.8-Figure 3.11. All tested samples revealed a consistent increase in ultrasonic velocity as the confined pressure increases. Additionally, all samples showed maximum velocity increase

occurring between 0 and 250 psi except for sample 3077 ft from Berthoud State 3 core (Figure 3.10) which showed rather minor change in velocity throughout the experiment.

3.2.3 Anisotropy Analysis

This section will present calculated results for three main groups of elastic parameters: (1) Stiffness tensor: provides a descriptive and quantifiable measure of the compressional and shear Stiffnesses in three dimensional reference; (2) Thomsen anisotropy parameters: summarize P and S wave anisotropies; and (3) anisotropy of dynamic geomechanical parameters as measured by dynamic Young's modulus, Poisson's ratio, bulk modulus and shear modulus.

3.2.3.1 Stiffness Coefficients

Stress (σ) applied to any object can be related to the strain (ε) created through Hooke's Law:

$$\sigma = C_{ij}\,\varepsilon \tag{3.1}$$

where: C_{ij} is the stiffness tensor. The stiffness of any given object can be described by the stiffness matrix derived from Hook's law for three dimensional objects:

$$C_{ij} = \begin{bmatrix} C_{11} & C_{12} & C_{13} & C_{14} & C_{15} & C_{16} \\ C_{21} & C_{22} & C_{23} & C_{24} & C_{25} & C_{26} \\ C_{31} & C_{32} & C_{33} & C_{34} & C_{35} & C_{36} \\ C_{41} & C_{42} & C_{43} & C_{44} & C_{45} & C_{46} \\ C_{51} & C_{52} & C_{53} & C_{54} & C_{55} & C_{56} \\ C_{61} & C_{62} & C_{63} & C_{64} & C_{65} & C_{66} \end{bmatrix} \tag{3.2}$$

In transversely isotropic medium (Figure 3.12), the stiffness tensor C_{ij} can be reduced to:

$$C_{ij} = \begin{bmatrix} C_{11} & C_{11}-2C_{66} & C_{13} & 0 & 0 & 0 \\ C_{11}-2C_{66} & C_{11} & C_{13} & 0 & 0 & 0 \\ C_{13} & C_{13} & C_{33} & 0 & 0 & 0 \\ 0 & 0 & 0 & C_{44} & 0 & 0 \\ 0 & 0 & 0 & 0 & C_{44} & 0 \\ 0 & 0 & 0 & 0 & 0 & C_{66} \end{bmatrix} \tag{3.3}$$

Table 3.1 Benchtop measured velocities, sorted primarily by core and secondarily by depth and type of wave velocity measured. Velocities are reported in km/s. Facies and internal structure of each sample is described in the third column.

Core	Zone (sub-Member)	Sample Lithology L=Laminated B=Bioturbated	Depth (Sample number)	Vp0	Vp45	Vp90	Vs0	Vs45	Vs90
			ft.	km/s					
Gill Land 2	A-Chalk	Marly Chalk (L)	6661.92	4.75	2.23	1.73	2.72	0.74	0.67
Gill Land 2	A-Marl	Chalky Marl (B)	6698.23	4.54	2.91	1.60	2.66	1.50	1.09
Gill Land 2	B Chalk	Marl (L)	6736.25	5.08	3.83	3.07	2.80	1.51	1.00
Gill Land 2	B Marl	Marly Chalk (B)	6776.25	5.12	4.10	3.94	2.93	2.16	2.05
Gill Land 2	B Marl	Marly Chalk (B)	6791.05	4.91	3.29	2.10	2.78	1.49	1.07
Gill Land 2	C chalk	Chalky Marl (L)	6816.67	5.09	4.44	3.98	2.87	1.73	1.08
Gill Land 2	C marl	Marl (L)	6851.5	4.60	2.82	1.70	2.54	1.38	0.78
Gill Land 2	C marl	Chalk (B)	6855.08	4.95	3.88	2.81	2.77	1.84	1.47
Gill Land 2	D chalk/marl	Marl (L)	6880	4.96	3.52	2.44	2.64	1.02	0.80
Gill Land 2	Ft. Hays	Limestone (B)	6890.47	5.53	5.48	4.98	2.67	2.68	1.91
Berthoud State 3	A-Chalk	Chalky Marl (B)	2936.5	5.14	5.15	4.99	2.87	2.89	2.83
Berthoud State 3	A-Marl	Marl (L)	2984.7	4.84	3.28	2.81	2.83	1.80	1.63
Berthoud State 3	B Chalk	Marly Chalk (B)	3013.1	4.45	4.42	3.76	2.77	2.63	2.44
Berthoud State 3	B Chalk	Chalky Marl (B)	3013.75	4.93	4.28	3.83	2.86	2.04	1.95
Berthoud State 3	B Marl	Chalky Marl (B)	3054.1	4.89	4.01	3.77	2.87	1.98	1.94
Berthoud State 3	C chalk	Marly Chalk (B)	3077.4	5.34	5.10	4.97	2.99	2.91	2.86
Berthoud State 3	C marl	Marl (L)	3101.9	4.83	4.13	3.83	2.83	2.71	2.53
Berthoud State 3	D chalk/marl	Marly Chalk (B)	3164.5	4.80	4.53	4.37	2.87	2.85	2.71
Berthoud State 3	Ft. Hays	Limestone (B)	3193.05	5.38	5.35	5.35	2.03	3.00	3.01

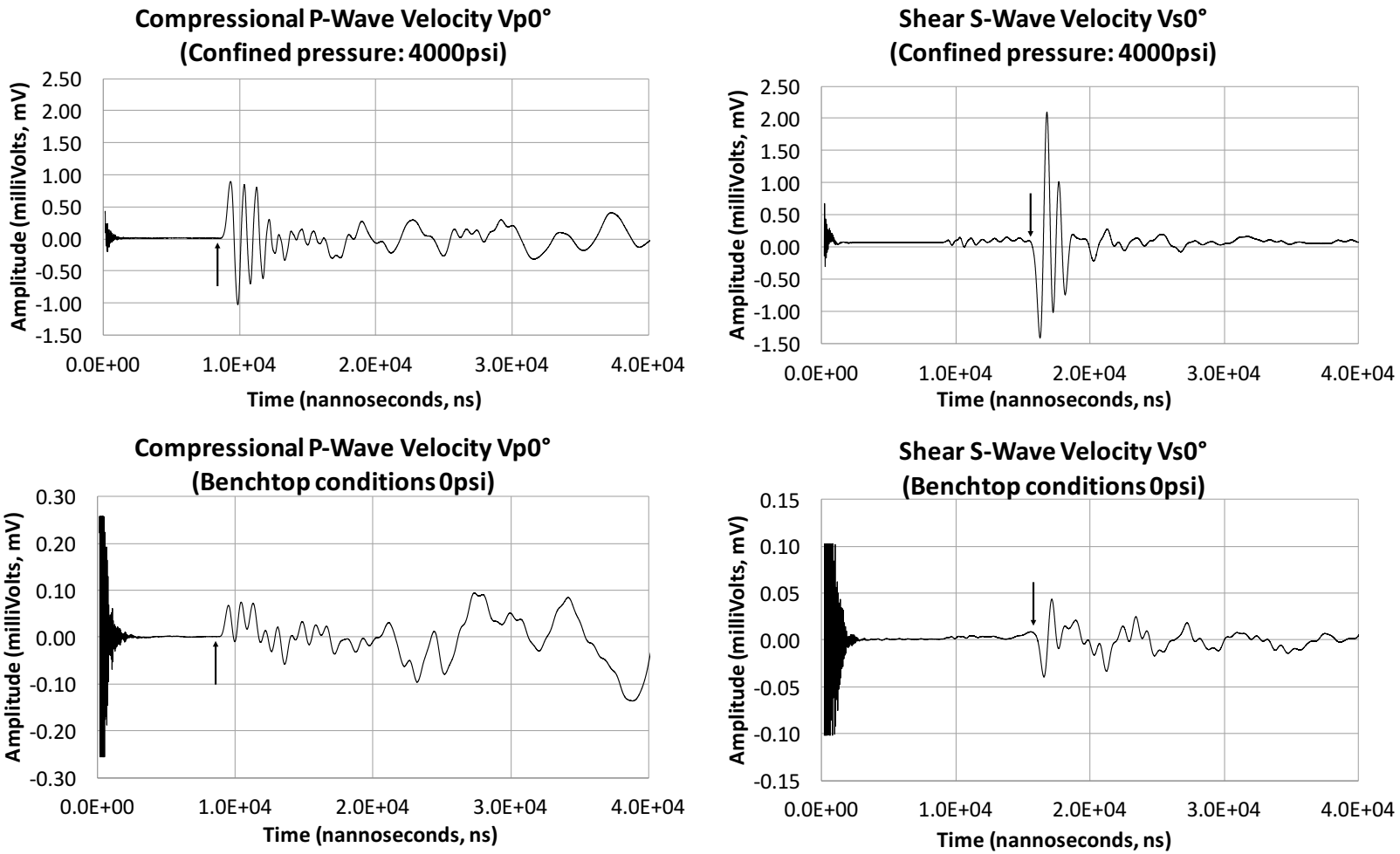


Figure 3.7 Compressional and shear wavelets examples from the acquired dataset. Results are from the parallel to bedding measurements for sample 3101.9 ft from Berthoud State3 core. The top waveforms were captured at 4000 psi confining pressure. Lower two waveforms represent benchtop 0 psi conditions. Vertical scale is amplitude. Horizontal scale is time. Arrow symbols demonstrate first arrival velocity picking. The vertical scale was modified for benchtop results to enhance the waveform.

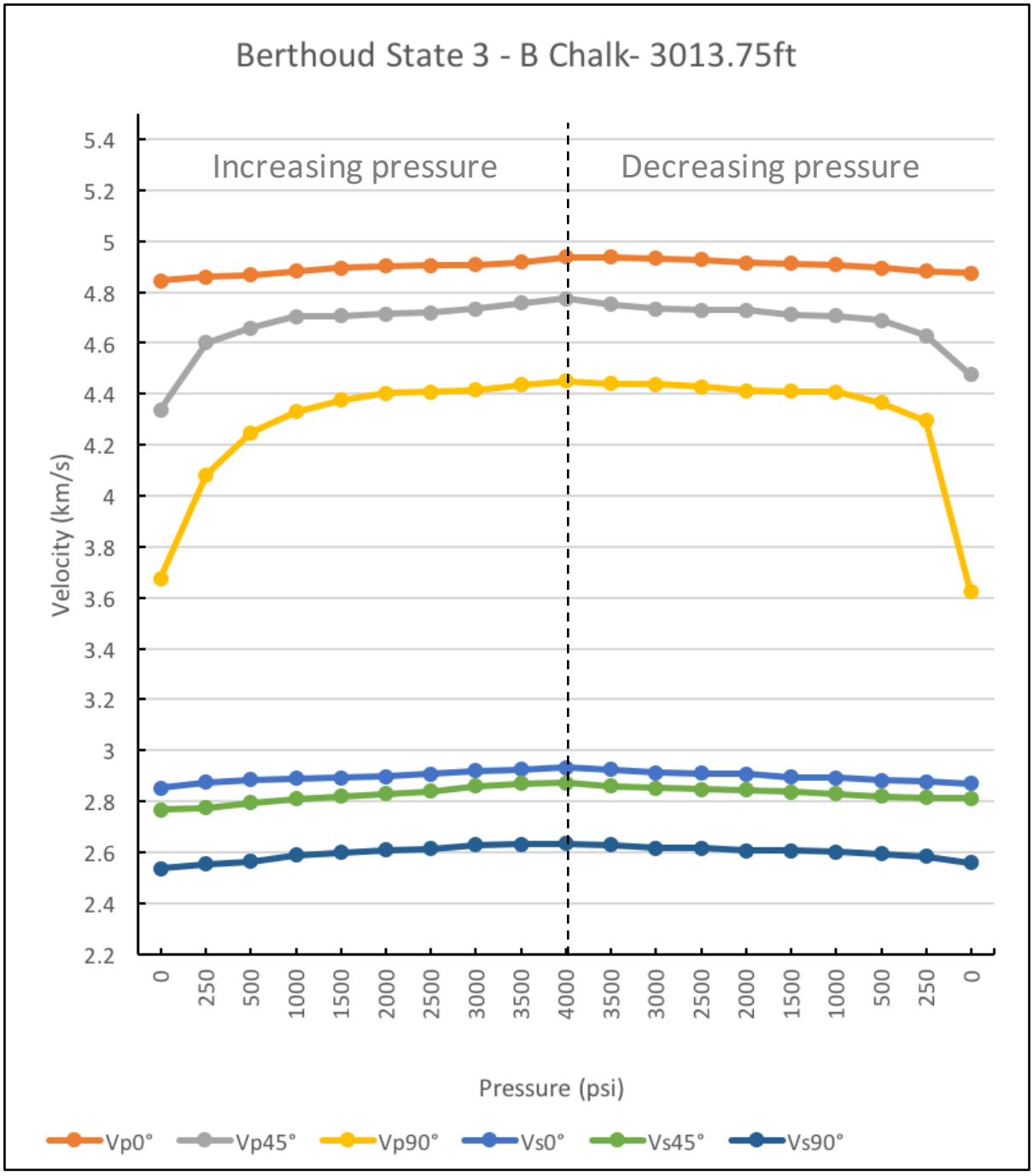


Figure 3.8 Velocity measurements under confined pressure for sample 3013.75 ft from Berthoud State 3 core. Horizontal axis is pressure; it shows the continuous range of pressures at which the samples were tested (i.e. pressuring up to 4000 psi followed by a pressuring down to 0 psi in a single continuous experiment). Vertical scale is velocity in km/s. Both compressional and shear velocities show modified velocity pattern during pressuring down stages. Velocities measured along the 90° exhibit the highest change in velocity in response to pressure change.

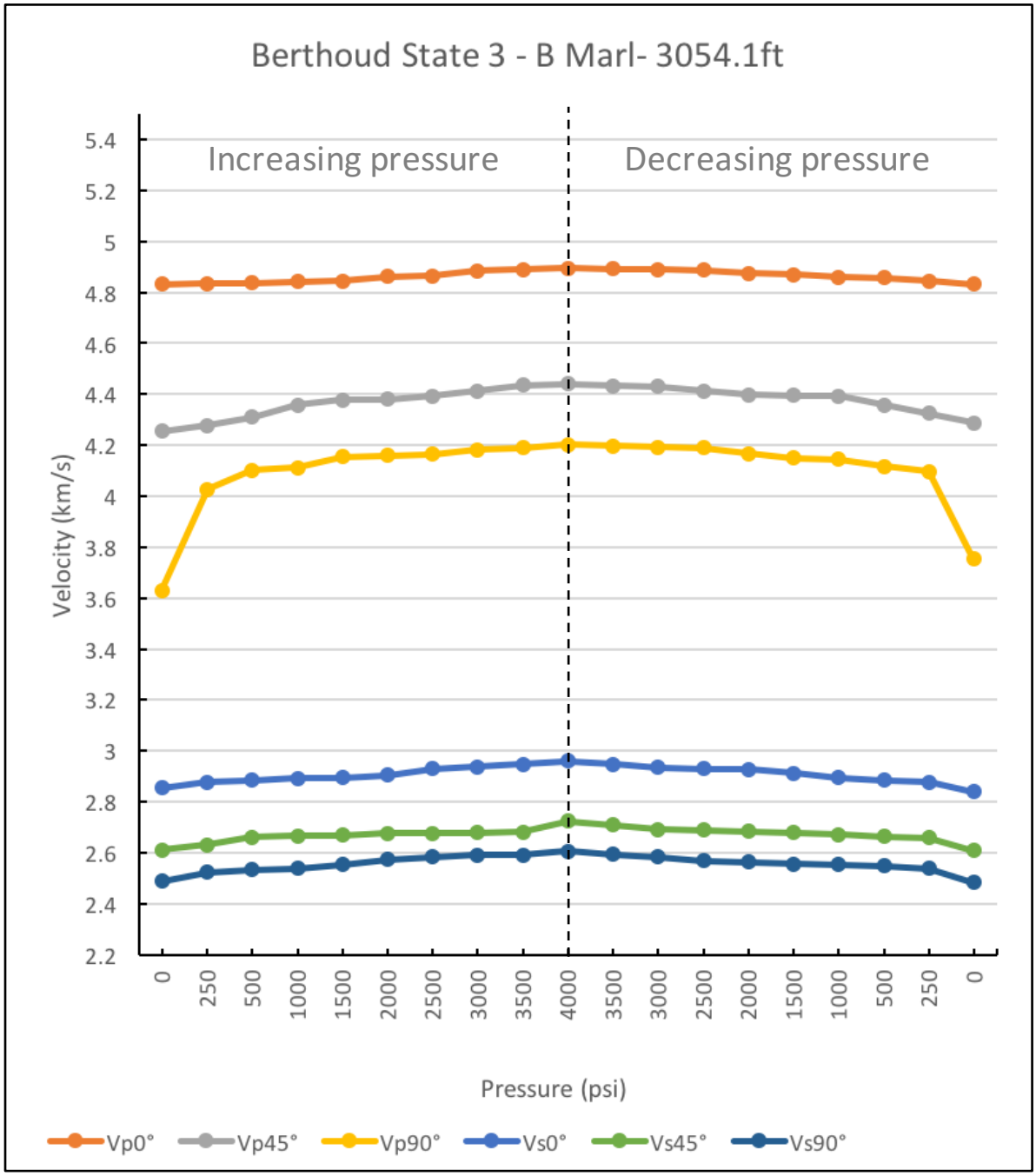


Figure 3.9 Velocity measurements under confined pressure for sample 3054.1 ft from Berthoud State 3 core. Both compressional and shear velocities show modified velocity patterns during pressuring down stages.

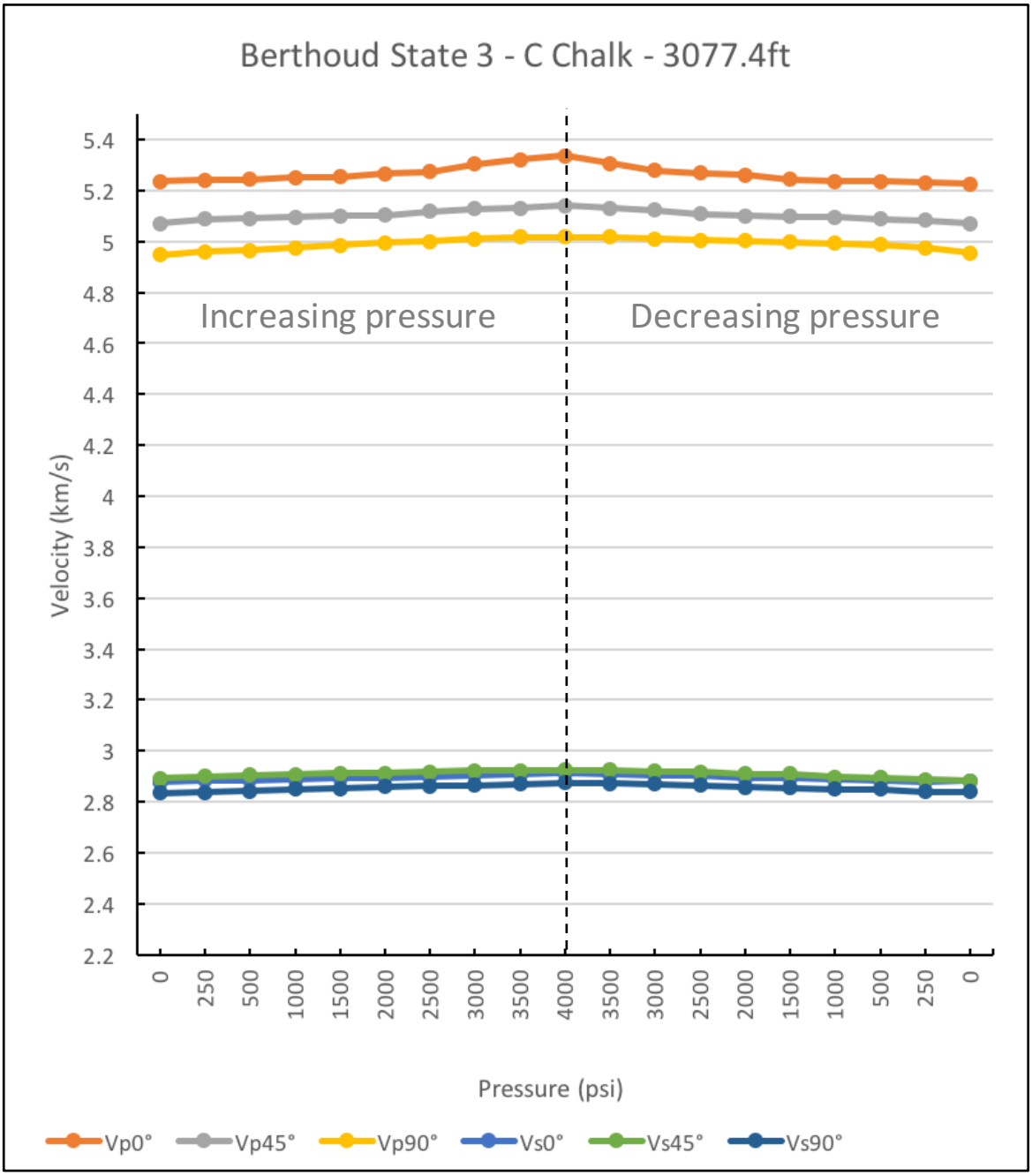


Figure 3.10 Velocity measurements under confined pressure for sample 3077.4 ft. from Berthoud State 3 core. Velocity change in response to pressure for this sample is much less pronounced when compared to the other tested samples.

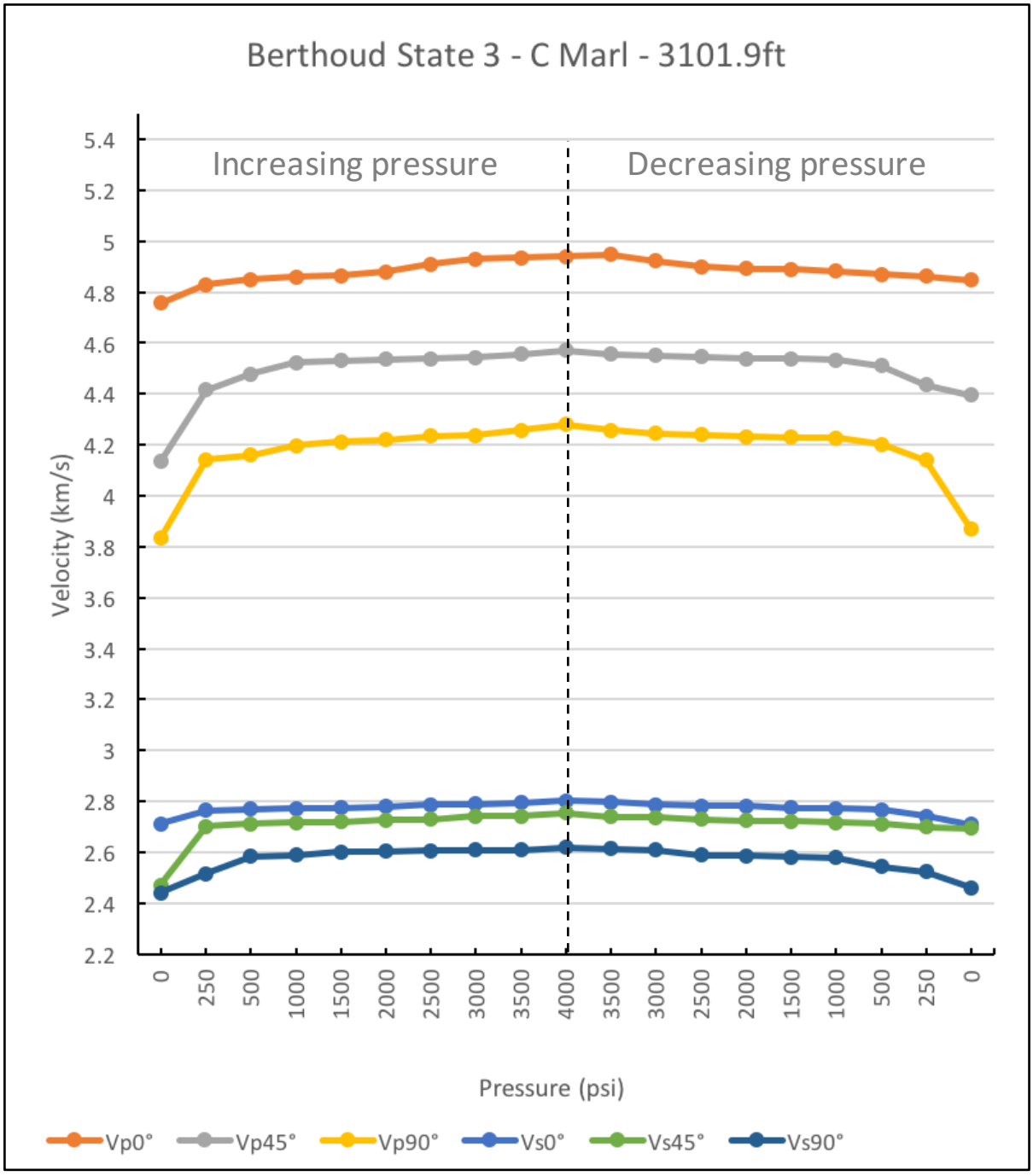


Figure 3.11 Velocity measurements under confined pressure for sample 3101.9 ft from Berthoud State 3 core. Both compressional and shear velocities show modified velocity patterns during pressuring down stages.

The Smoky Hill Member of the Niobrara Formation consists of highly cyclic interstratified marl and chalk beds. This formed a horizontally laminated sedimentary deposit, that locally can be bioturbated observed during facies analysis (Figure 3.3). This satisfies the transversely-isotropic objects definition. Therefore, the stiffness tensor matrix from Hook's law for transversely isotropic becomes applicable. Six independent stiffness coefficients for can be calculated and used to describe three dimensional objects. The following equations were used to calculate the stiffness coefficients (King, 1969):

Parallel to bedding compressional:

$$C_{11} = \rho V_{P0}^2 \tag{3.4}$$

Normal to bedding compressional:

$$C_{33} = \rho V_{P90}^2 \tag{3.5}$$

Normal to bedding shear:

$$C_{44} = \rho V_{S90}^2 \tag{3.6}$$

Parallel to bedding shear:

$$C_{66} = \rho V_{S0}^2 \tag{3.7}$$

Parallel to bedding translational:

$$C_{12} = C_{11} - 2C_{66} \tag{3.8}$$

Normal to bedding translational:

$$C_{13} = -C_{44} + \sqrt{(C_{11} + C_{44} - 2\rho V_{45}^2)(C_{33} + C_{44} - 2\rho V_{45}^2)} \tag{3.9}$$

where: ρ is density in kg/m^3, V_P and V_S denote compressional and shear velocities respectively. Number subscripts associated with each velocity denote the direction of the measurement (Figure 3.12). Mechanically, stiffness coefficients can be used to describe the rigidity or resistance against applied stresses. Moreover, each coefficient represents the stiffness of the tested sample in a specific direction and while being subjected to a specific stress type, e.g. compressional, shear or translational. Results of the calculated stiffness coefficients are presented in Figure 3.13 and Figure 3.14. Confined pressure results for all samples suggest that compressional stiffness coefficients (i.e. C11 and C33) are considerably higher, ranging 38-72 Gpa, in comparison to shear and translational stiffnesses (range of 15-30 Gpa). Specifically, results of sample 3077.4 ft (a C chalk sample) from Berthoud State 3 core indicate much higher overall stiffness. Although shear and translational stiffnesses are closely clustered, the transverse translational stiffness coefficient (C13) was consistently the lowest except for sample 3077.4.

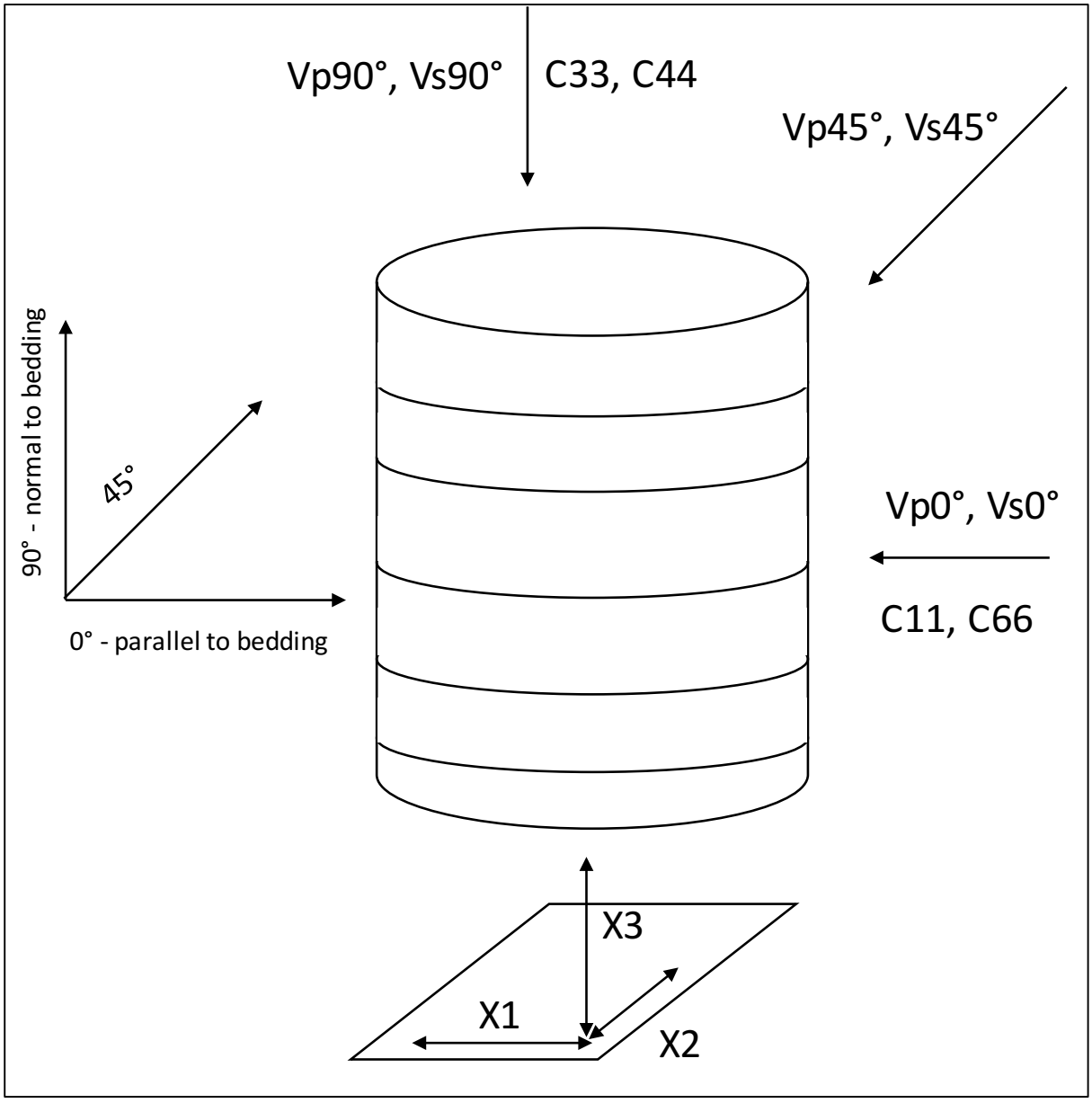


Figure 3.12 Schematic illustration of principal axes of rotation, orientation of measured velocities and orientation of stiffness coefficients discussed in any transversely isotropic medium. Note: both X1 and X2 are parallel to bedding axes whereas X3 is perpendicular to bedding plane.

Stiffnesses calculated from benchtop velocities (Figure 3.14) also shows that bedding parallel compressional stiffness (C11) is the highest. Transverse compressional stiffness was lower than translational and transverse shear stiffnesses in three marls and one chalk samples from the Gill Land 2 core. In both cores, Ft. Hays samples yielded the highest overall stiffness.

Additionally, noticeable increase in stiffness was observed in samples collected form the B and C intervals when compared to samples from the A interval within the Smoky Hill Member. In general, translational and shear stiffness coefficients are consistently closely ranged in both cores. This may suggest that orientation of tested velocity does not have as great effect on the resultant shear and translational particle movements as their compressional counterparts.

3.2.3.2 Thomsen Anisotropy Parameters

In addition to the stiffness coefficients, Thomson anisotropy parameters were calculated using the equations below:

$$\varepsilon = \frac{C_{11} - C_{33}}{2C_{33}} \tag{3.10}$$

$$\gamma = \frac{C_{66} - C_{44}}{2C_{44}} \tag{3.11}$$

$$\delta = \frac{(C_{13} + C_{44})^2 - (C_{33} - C_{44})^2}{2C_{33}(C_{33} - C_{44})} \tag{3.12}$$

Where epsilon (ε) is the P wave anisotropy factor, gamma (γ) is the S wave anisotropy factor and delta (δ) is a parameter controlled by the P wave shape and S wave surfaces. Thomsen anisotropy parameters for benchtop and confined pressure results are presented in Figure 3.15 and Figure 3.16 respectively. Anisotropy seems to decrease significantly when a confining pressure is applied up to 500 psi, reduction in anisotropy beyond 500 psi is very subtle. The 3077 sample from the Berthoud State 3 core represents an exception as it shows an increase in delta and epsilon anisotropies at 2500 psi. It also yielded the lowest anisotropy parameters from the confined pressure tested samples. The overall magnitude of anisotropy for Gill Land 2 core samples is much greater than the Berthoud State 3 core samples. All anisotropy parameters reduce to zero in Ft. Hays limestone samples in both cores suggesting isotropic behavior. Sample 6776.25 from the Gill Land 2 core and samples 3013.1 and 3077.4 from the Berthoud State 3 core also show similar behavior.

3.2.3.3 Elastic Moduli

Bulk modulus *(K)* measures the resistance of the rock to change its volume in response to applied compression. It is a factor of the applied pressure and the relative change in volume. In contrast, shear modulus (G) is a measure of rock resistance to a change its shape in response to applied shear forces. Shear modulus can also be used to describe the rigidity of the rock. Young's modulus is concerned with the relationship between the stress applied and the strain or deformation produced.

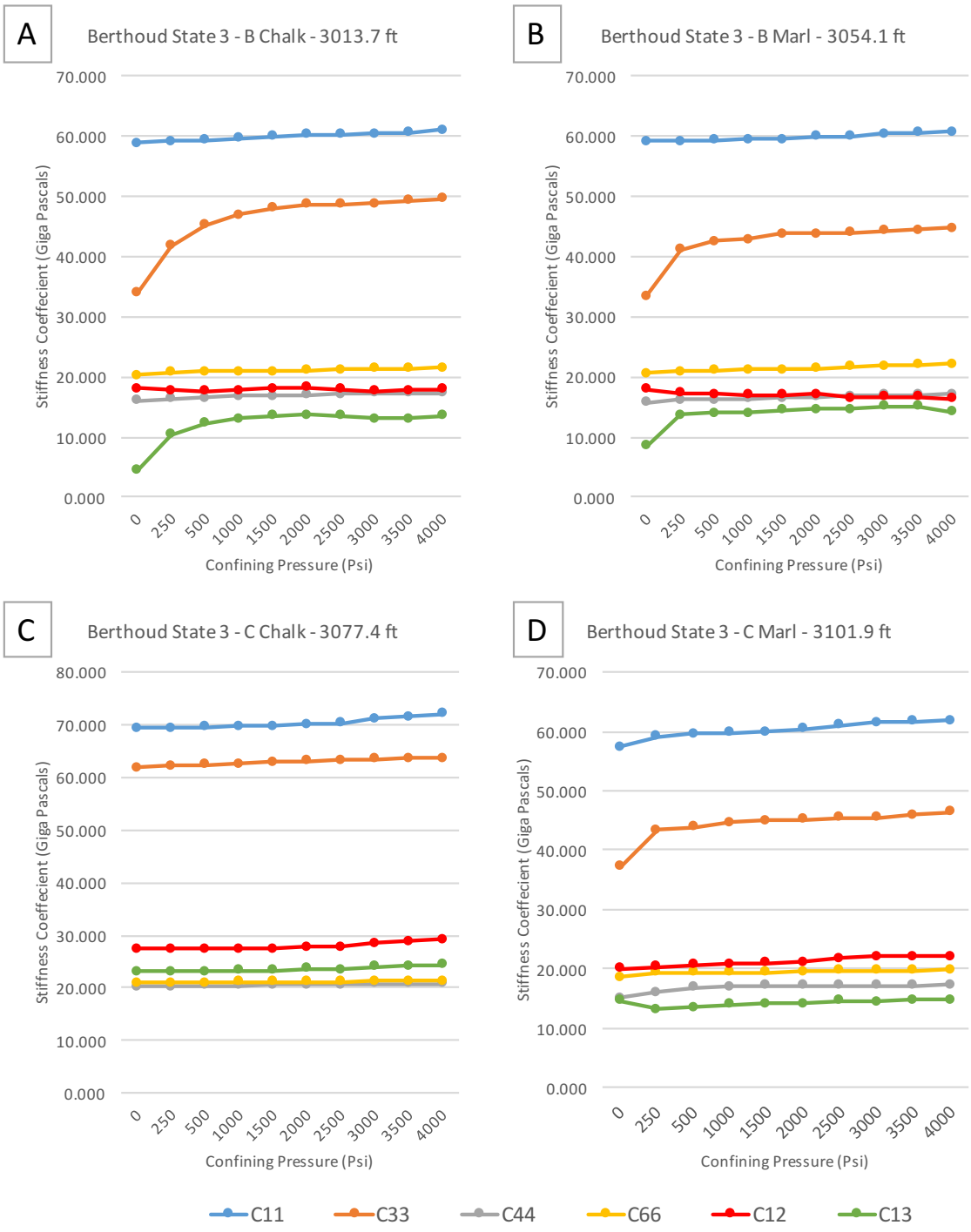


Figure 3.13 Crossplots of calculated stiffness coefficients (in giga Pascal's, Gpa) from measured velocities versus applied confining pressure (in psi). All samples are from the Berthoud State 3 core. Samples shown are: (A) B chalk. (B) B marl. (C) C chalk. (D) C marl. Generally, stiffness is greater in the three observed directions (i.e. 0°, 45° and 90°) in sample 3077. The latter sample particularly shows different behavior when compared to the other three samples.

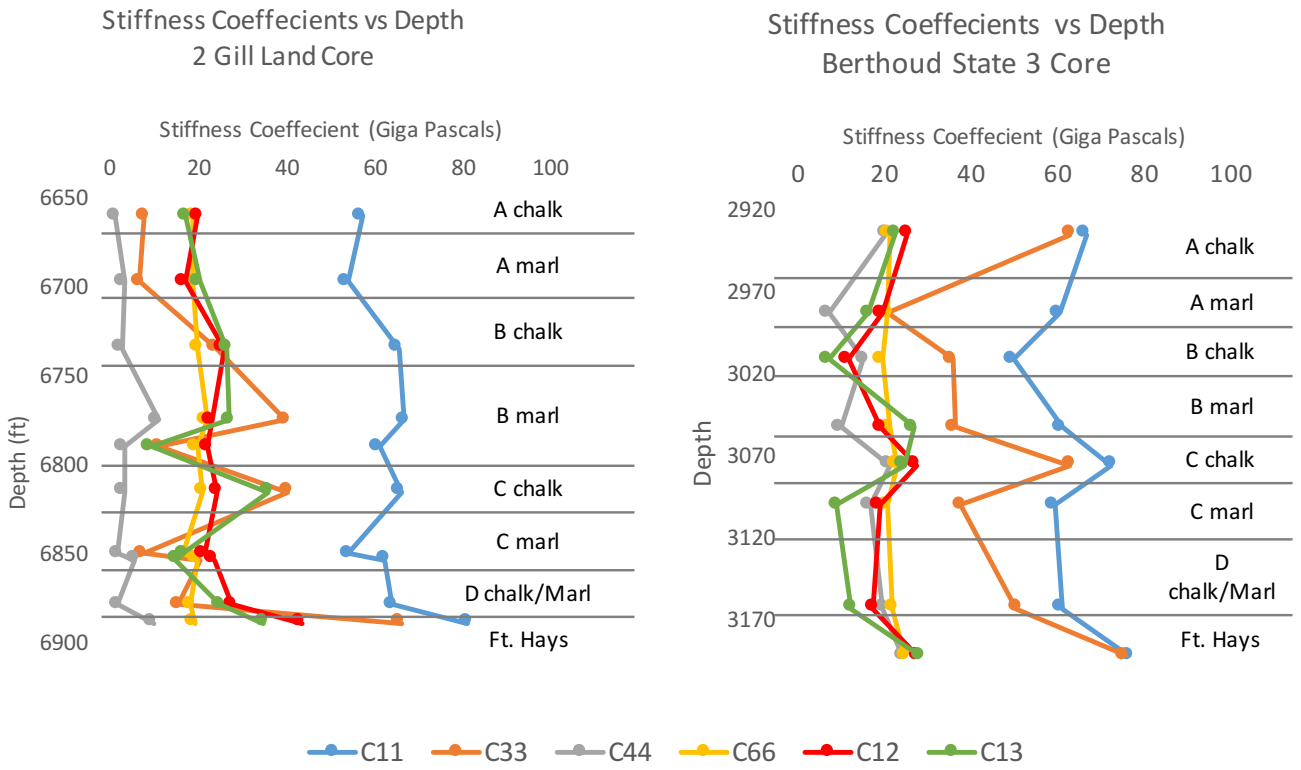


Figure 3.14 Stiffness coefficients (in Gpa) for benchtop measured velocities plotted against depth (in ft.). Left plot is for Gill Land 2 core samples. Right plot is for Berthoud State 3 core samples. This plot provides comparable multidirectional stiffness measurements for all Niobrara Formation interval. Ft. Hays limestone samples shows the highest stiffness coefficients in all directions. A moderate increase in stiffness can be observed in B and C samples when compared to the other intervals within the Smoky Hill Member.

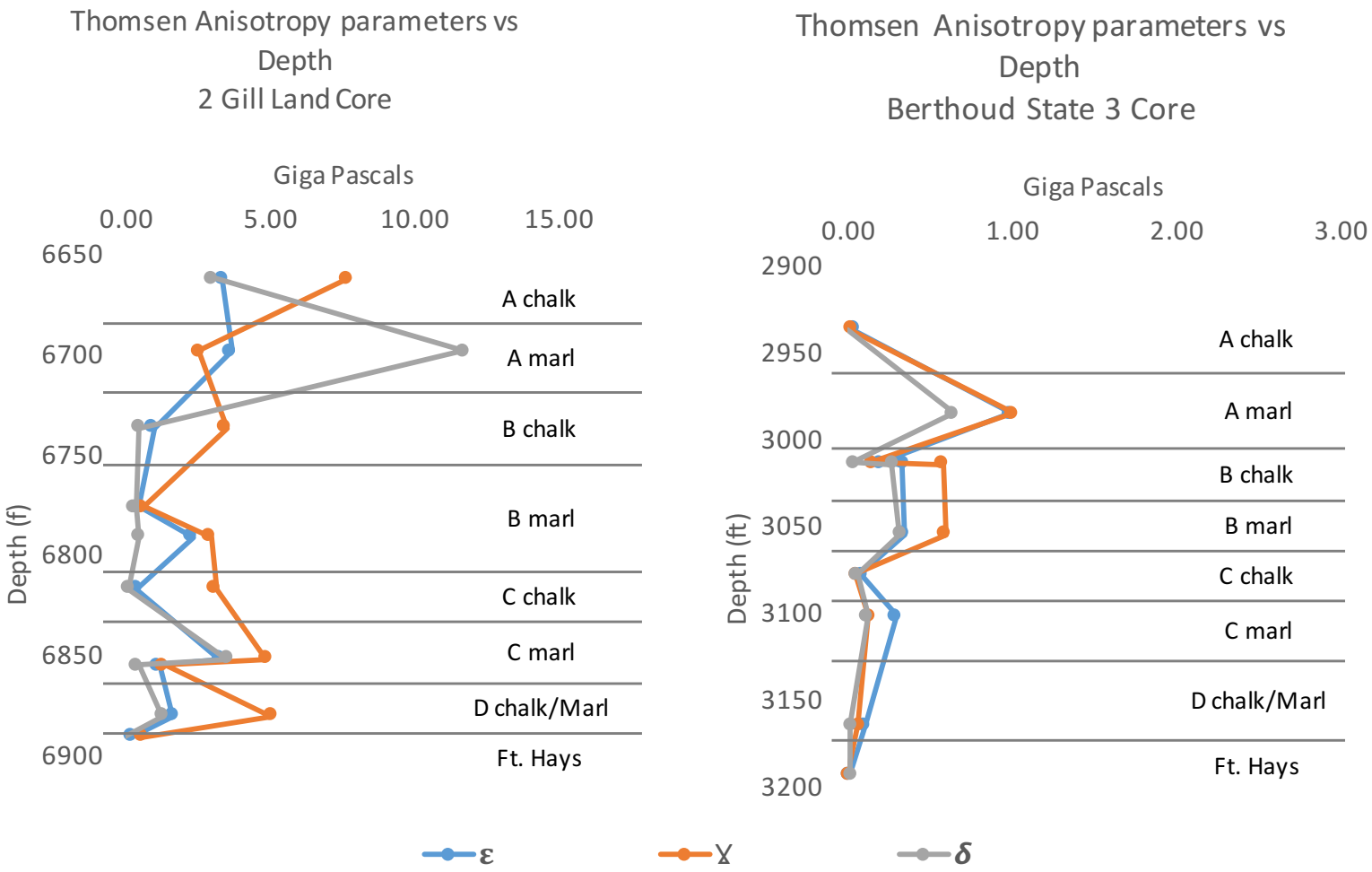


Figure 3.15 Thomsen anisotropy parameters from benchtop velocities. Right plot shows Berthoud State 3 core samples. Left plot shows Gill Land 2 core samples. Samples are annotated with the origin of sample interval. It is very important to note that Thomsen anisotropy parameters are much lower in magnitude for Berthoud State 3 core samples. Note the horizontal scale difference. Ft. Hays samples anisotropies are very low suggesting an isotropic acoustic behavior.

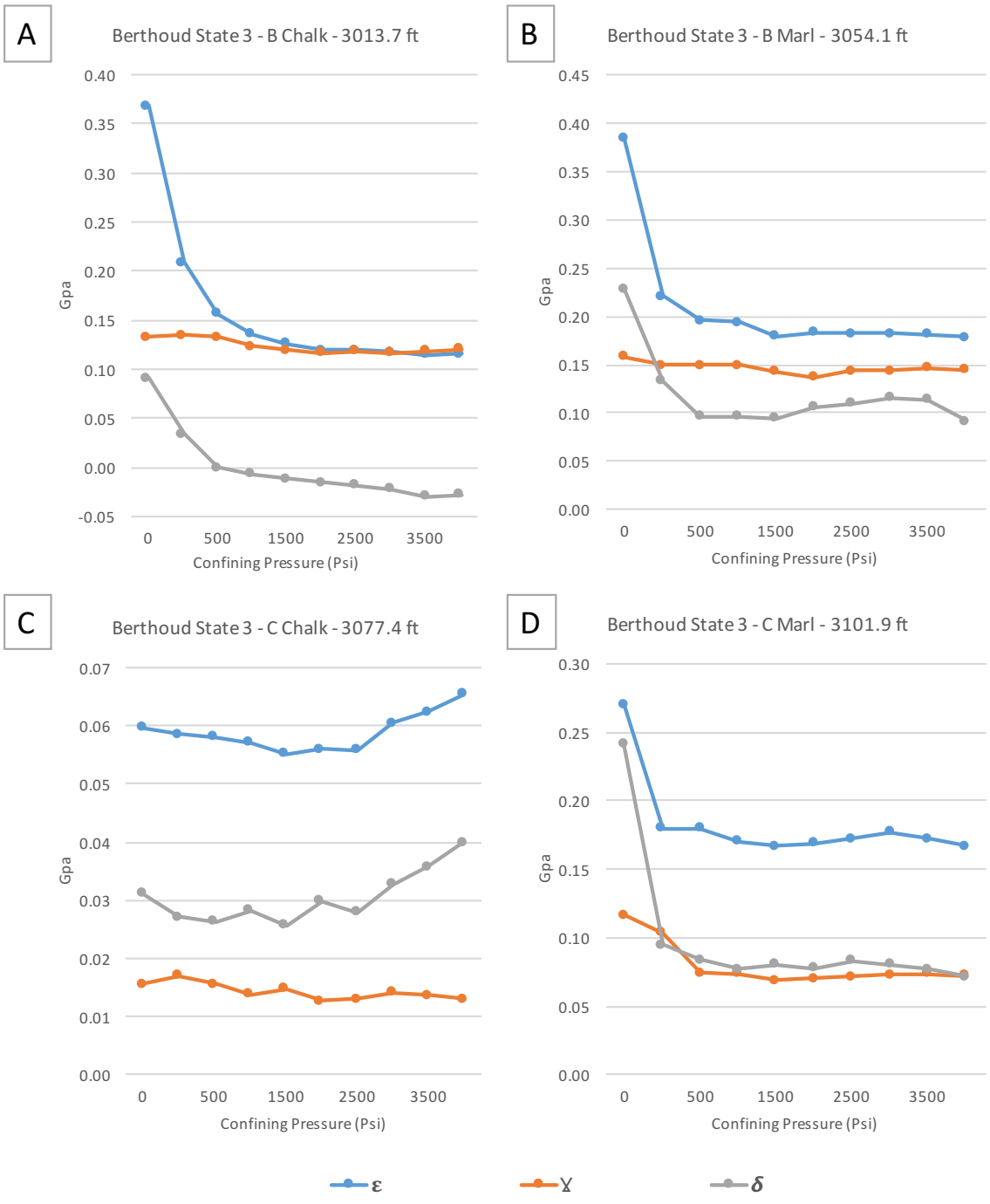


Figure 3.16 Thomsen anisotropy parameters calculated from measured velocities under different confining pressures. (A) sample from B chalk, (B) B marl, (C) C chalk and (D) C marl. All sample exhibit major change in all anisotropies at 250 psi except sample 3077.4 ft. While all the samples don't show major changes in their anisotropies beyond 250ps, 3077.4 sample shows noticably increasing epsilon and gamma anisotropies beyond 2500psi.

Poisson's ratio is the ratio of length or volume change in one axis to another. It can also be defined as the ratio of the strain in axis a to the strain in axis b. These parameters can be calculated using the following equations (King, 1969):

Bulk modulus

$$K = \frac{C_{33}(C_{11}+C_{12})-2C_{13}^2}{C_{11}+2C_{33}+C_{12}-4C_{13}} \quad (3.13)$$

Vertical shear modulus

$$G_V = C_{44} \quad (3.14)$$

Horizontal shear modulus

$$G_H = C_{66} \quad (3.15)$$

Horizontal Young's modulus

$$E_h = \frac{(C_{11}+C_{12})(C_{11}C_{33}-2C_{13}^2+C_{12}C_{33})}{C_{11}C_{33}-C_{13}^2} \quad (3.16)$$

Vertical Young's modulus

$$E_v = C_{33} - \frac{2C_{13}^2}{C_{11}+C_{12}} \quad (3.17)$$

Poisson's Ratio (X3 /X1) *

$$\nu_{13} = \frac{C_{13}(C_{11}-C_{12})}{C_{11}C_{33}-C_{13}^2} \quad (3.18)$$

Poisson's Ratio (X1/X3)

$$\nu_{31} = \frac{C_{13}}{C_{11}-C_{12}} \quad (3.19)$$

Poisson's Ratio (X1 /X2)

$$\nu_{12} = \frac{C_{12}C_{33}-C_{13}^2}{C_{11}C_{33}-C_{13}^2} \quad (3.20)$$

*see Figure 3.12 for an illustration of referenced axes.

Bulk, shear and Young's moduli results under variable confining pressure are presented in Figure 3.17. Poisson's ratios results are presented in Figure 3.18. Both 3013.7 and 3054 samples show notable decrease in compressibility up to 250 psi indicated by the increase in bulk modulus, no notable change is observed beyond 250 psi. Horizontal and vertical shear response of the samples increase when a pressure is applied up to 1500 psi. Shear resistance and vertical Young's modulus continue to increase beyond 1500 psi but change is very subtle. Sample 3013.7 exhibits the highest gain in vertical Young's modulus as confining pressure increases.

Samples 3077.4 and 3101.9 show increasing horizontal Young's modulus when confining pressure is applied. The change in compressibility is noticeably lower throughout the tested pressure interval when compared to the samples from the B interval within the Smoky

Hill Member. Overall gain in compressibility, shear and vertical Young's moduli in sample 3077.4 is minimal with increasing pressure when compared to the other samples. Sample 3077.4 also shows isotropic shear resistance behavior (i.e. both vertical and horizontal shear moduli are the same).

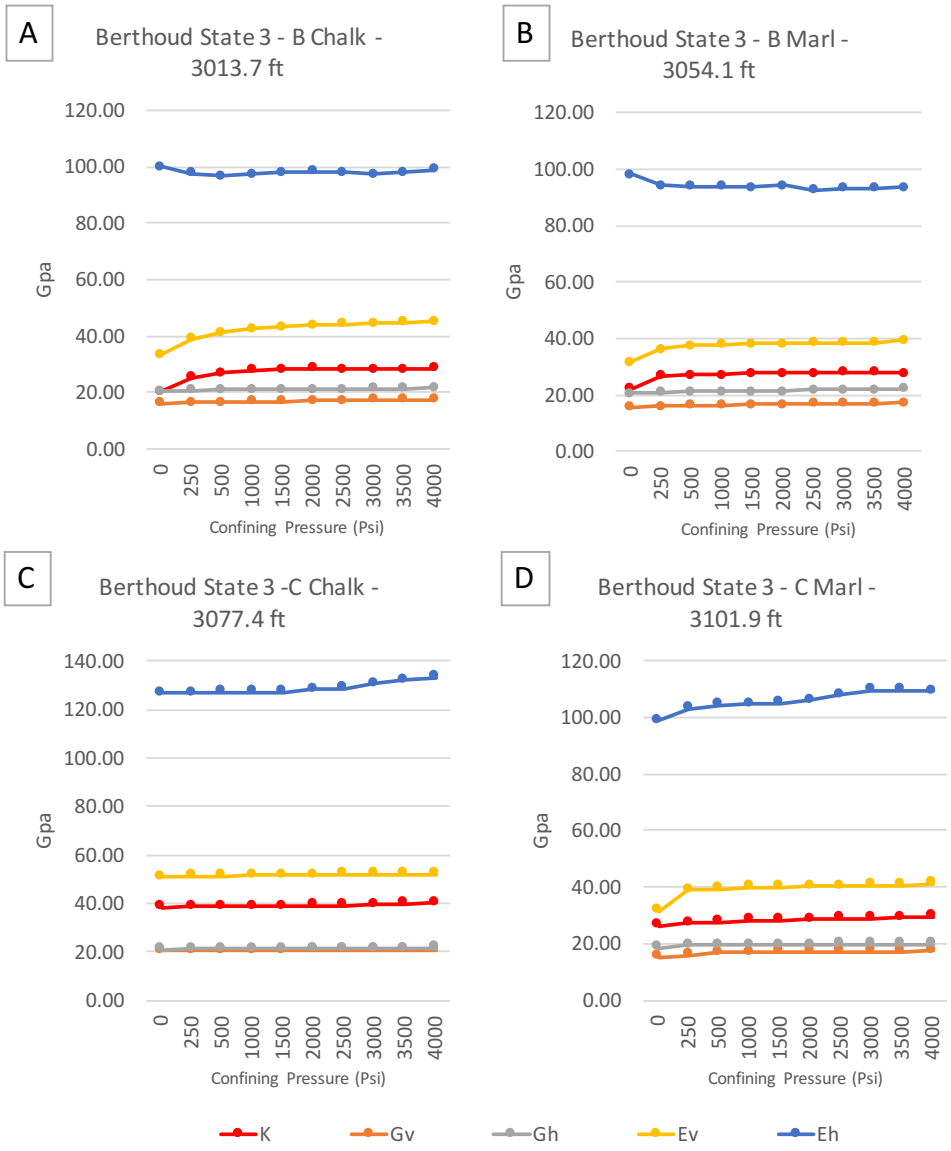


Figure 3.17 Crossplots of elastic moduli versus confining pressure: Bulk modulus (K),vertical shear modulus (Go), horizontal shear modulus (Gh), (Ev) and (Eh) are vertical and horizontal Young's modulus respectively. (A) sample from B chalk, (B) B marl, (C) C chalk and (D) C marl. All samples share similar trend beyond 250 psi in bulk modulus, shear moduli and vertical Young's modulus. Sample 3077 shows distenctivly smaller change between 0-250 psi. Bulk modulus is semi-stable beyond 250 psi in B samples whereas it increases in C samples.

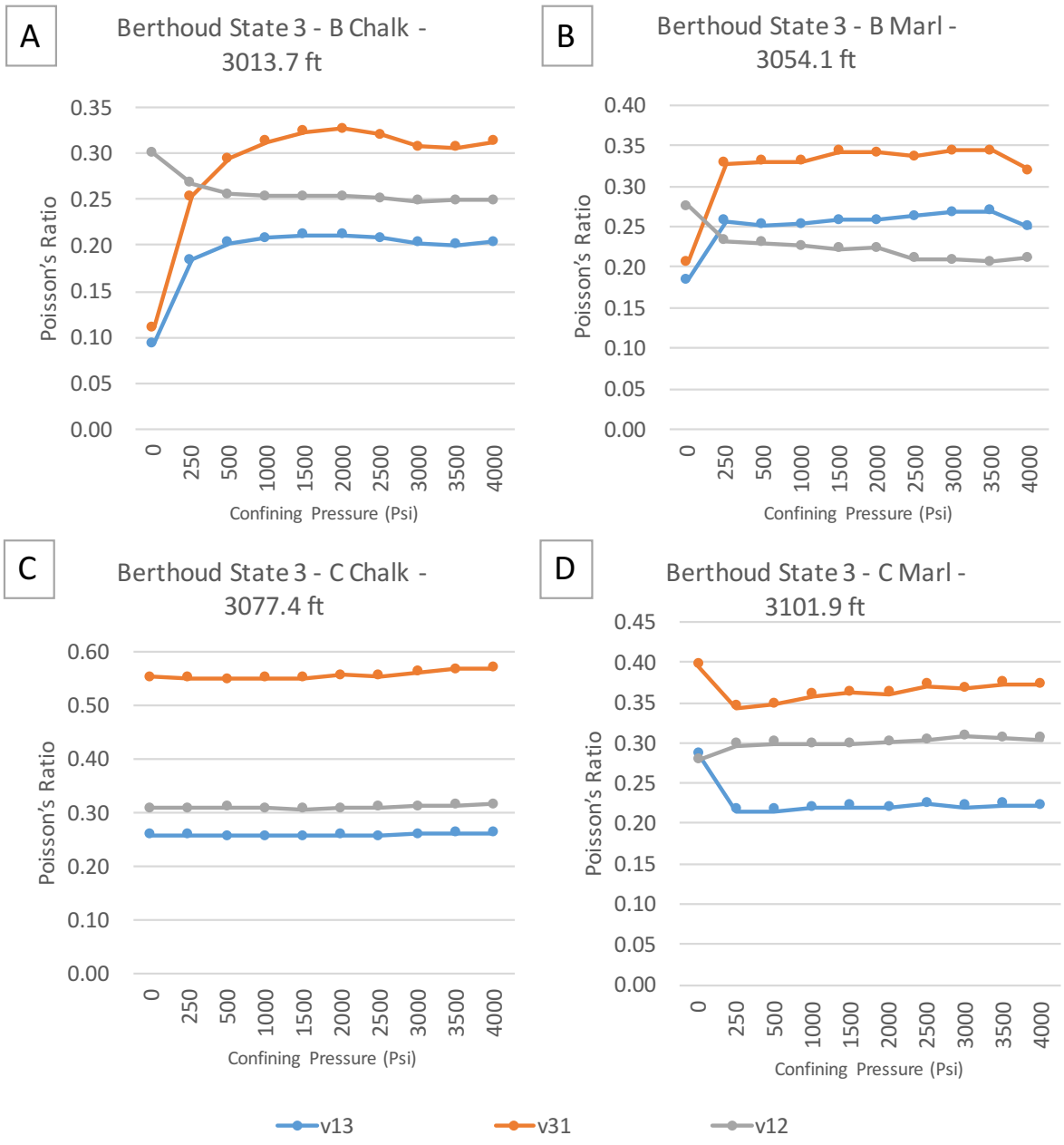


Figure 3.18 Poisson's ratio as a function of variable confining pressure. v13 is ratio of change X3/X1, v31 is for X1/X3 and v12 is for X1/X2. See Figure 3.12 for illustration of axes orientation. (A) sample from B chalk, (B) B marl, (C) C chalk and (D) C marl. Specifically in sample 3077.4, the effect of confining pressure on the change in Poisson's ratio seems to be minimal.

Horizontal to vertical (i.e. X1/X3) Poisson's ratio (*v31*) is highest for all samples suggesting that all samples have higher tendency to deform greater horizontally in the X1 direction. All samples show notable gain or loss of all Poisson's ratio in response to the variable confining pressure except for 3077.4 sample which shows negligible to minimal change in the

v13 and *v12*. By definition *v31* and *v13* are reciprocals of each other, therefore they tend to have an inversely proportional relationship (Figure 3.18).

3.3 Organic Content and Maturity

Core cuttings were analyzed using an in-house source rock analyzer. Results from a total of 17 samples from both cores were compiled below to obtain organic richness and maturity levels which were used to investigate its effect on ultrasonic velocities. A programmed pyrolysis was used to measure TOC, S1, S2, S3 and Tmax values (Table 3.2). The following equations were used to calculate: hydrogen index (HI), oxygen index (OI), productivity index (PI), and calculated vitrinite reflectance (Ro) (Jarvie et al., 2001):

$$HI = \left(\frac{S2}{TOC}\right) x\ 100 \tag{3.21}$$

$$OI = \left(\frac{S3}{TOC}\right) x\ 100 \tag{3.22}$$

$$PI = \frac{S1}{S1+S2} \tag{3.23}$$

$$\%Ro = (0.0180\ x\ Tmax) - 7.16 \tag{3.24}$$

3.3.1 Total Organic Carbon and Kerogen Type

Organic carbon richness in the samples ranged between 0.24 wt.% in the Ft. Hays limestone and 4.79 wt.% in marls. Samples from chalk intervals show poor organic richness (1.54 – 2.83 wt. %) compared to marl intervals (2.39 – 4.79 wt.%). Samples from the Ft. Hays Limestone Member have very low TOC levels (i.e. <0.7) and thus are considered to be non-source rocks. Samples from C marl intervals were consistently richest in both cores, exceeding 4 wt.% TOC. Total organic carbon levels variations were visible between different zones, however, no inter-core variability was observed. To determine kerogen types, pyrolysis results were plotted using modified Van Krevlen diagram (Figure 3.19). Results show that both cores contain a mixture of kerogen types II and III. However, Gill Land 2 core is located in a thermally mature area which lower hydrogen index values. Source rocks with type II only kerogen can generate both oil and gas in contrast to type III which can be more gas-prone. The Niobrara Formation was deposited in marine environment with variable and minimal terrestrial input from the west. This conforms to the results as type II can be correlated to shelf or marine settings whereas kerogen type III form in fluvial or alluvial settings (Hantschel and Kauerauf, 2009).

Table 3.2 Summary table for source rock analysis data used in this study. Note: two samples from Berthoud State 3 were not analyzed by pyrolysis.

Core	Zone	Depth	TOC	S1	S2	S3	Tmax	HI	OI	S2/S3	S1/TOC *100	PI	Calculated Ro
		ft.	wt. %	mg HC/g rock	mg HC/g rock	mg CO2/g rock	(°C)	mg HC/g rock	mg CO2/g rock	ratio	mg HC/g rock	ratio	From Tmax
Gill Land 2	A-Chalk	6661.92	2.75	3.27	3.61	0.25	439.00	131.00	9.00	14.44	118.91	0.48	0.74
	A-Marl	6698.23	3.48	2.99	4.27	0.31	442.00	123.00	9.00	13.77	85.92	0.41	0.80
	B Chalk	6736.25	3.03	2.84	3.28	0.24	449.05	108.00	8.00	0.87	93.73	0.46	0.92
	B Marl	6776.25	2.39	2.58	3.75	0.25	449.00	157.00	10.00	15.00	107.95	0.41	0.92
	B Marl	6791.05	4.13	1.81	3.29	0.33	460.10	80.00	8.00	9.97	43.83	0.36	1.12
	C chalk	6816.67	1.54	1.83	1.30	0.25	442.56	84.00	16.00	1.41	118.83	0.59	0.81
	C marl	6851.50	2.57	2.02	3.51	0.40	449.00	137.00	16.00	8.78	78.60	0.37	0.92
	C marl	6855.08	4.76	2.38	4.59	0.26	460.49	96.00	6.00	0.52	50.00	0.34	1.13
	D chalk/marl	6880.00	1.20	0.66	1.20	0.28	447.00	100.00	23.00	4.29	55.00	0.35	0.89
	Ft. Hays Limestone	6890.47	0.24	0.19	0.22	0.29	312.00	92.00	121.00	0.76	79.17	0.46	-
Berthoud State 3	A-Chalk	2936.50	2.71	5.04	5.89	0.33	432.72	217.00	12.00	17.85	185.98	0.46	0.63
	A-Marl	2984.70	3.15										
	B Chalk	3013.10	1.78										
	B Chalk	3013.75	2.83	2.92	7.03	0.34	439.69	248.00	12.00	20.68	103.18	0.29	0.75
	B Marl	3054.10	3.39	2.45	8.72	0.29	443.59	257.00	8.00	30.07	72.27	0.22	0.82
	C chalk	3077.40	2.50	5.41	5.94	0.31	438.42	238.00	13.00	19.16	216.40	0.48	0.73
	C marl	3101.90	4.79	1.85	14.42	0.55	442.00	301.04	11.48	26.22	38.62	0.11	0.80
	D chalk/marl	3164.50	0.64	0.22	0.19	0.41	349.65	30.00	64.00	0.46	34.38	0.53	-
	Ft. Hays Limestone	3193.05	0.28	0.12	0.08	0.20	416.83	30.00	71.00	0.40	42.86	0.60	-

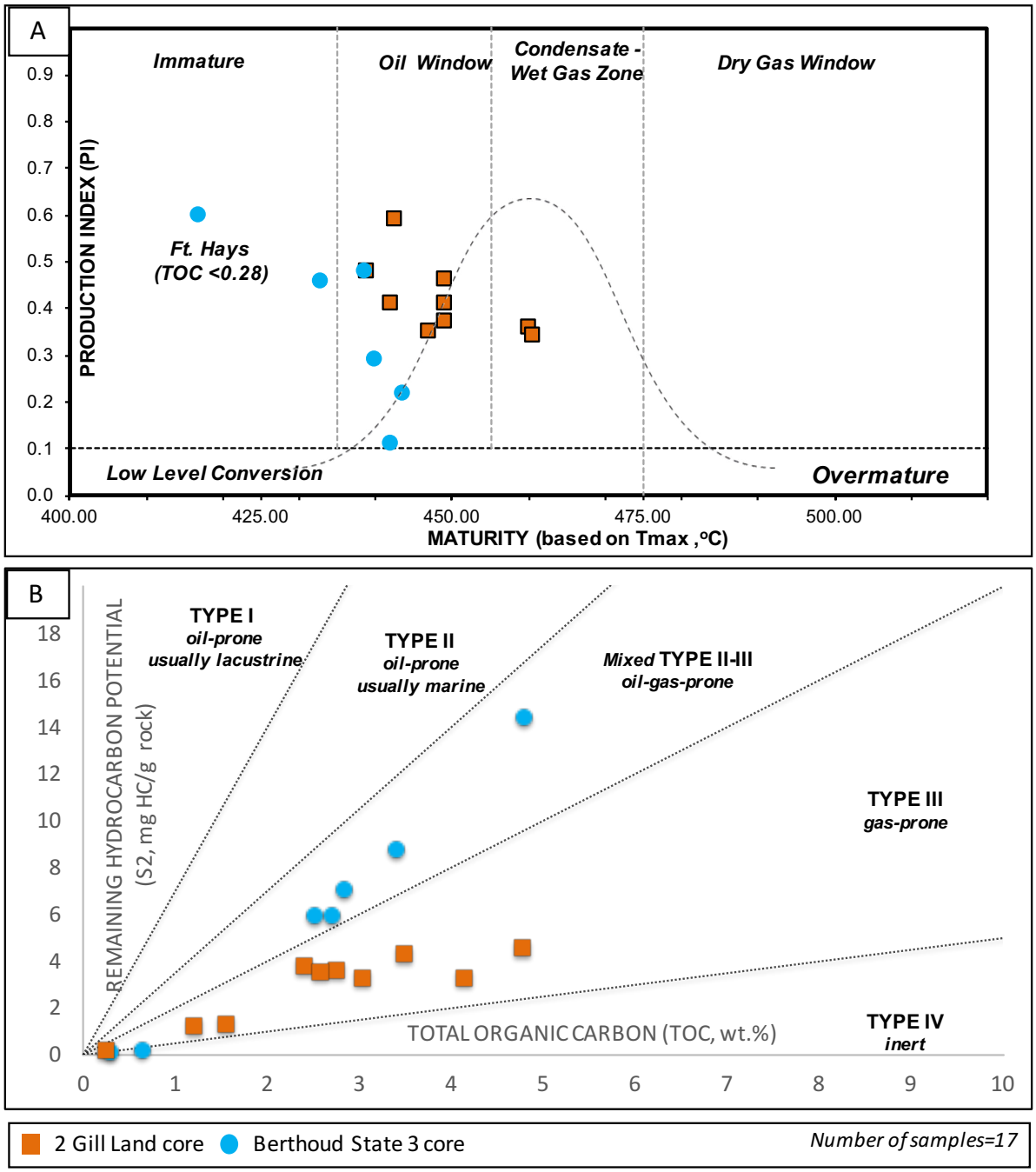


Figure 3.19a Plots of source rock analysis data: (A) maturity plot using Tmax and productivity index (PI), (B) kerogen typing from S2 versus TOC values, (C) maturation levels from Tmax and hydrogen index (HI), (D) kerogen typing from HI and oxygen index (OI). Two different levels of maturity can be observed. Although both cores contain mixture of kerogen types II and III, kerogen from Gill Land 2 core appears to contain more type III by comparison. It is important to note that the higher maturity of Gill Land 2 samples suppresses the kerogen types in B and D above. Plots reference grids are modified from (Finn and Johnson, 2005).

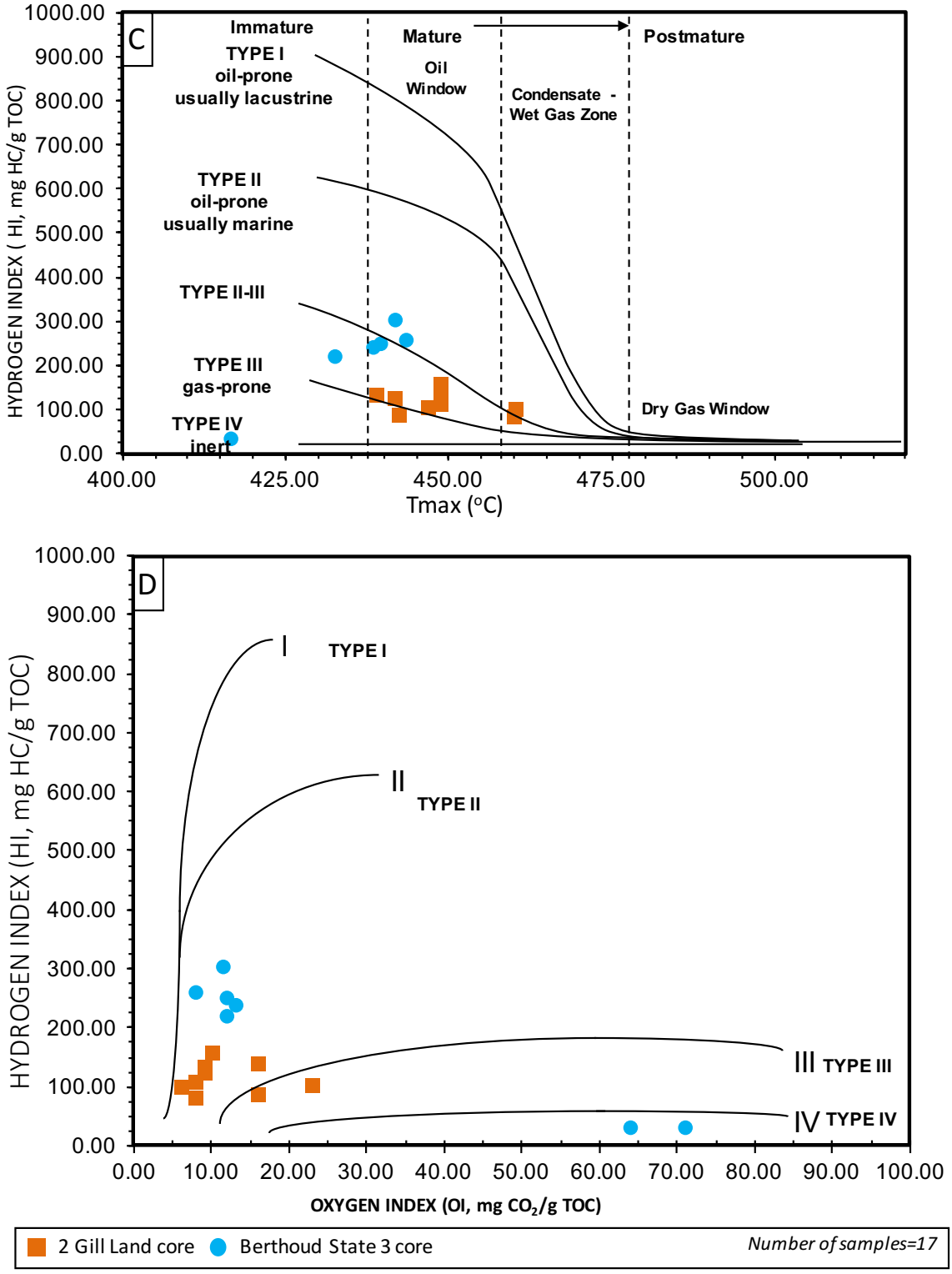


Figure 3.19b continued.

3.3.2 Source Rock Maturity

Maturation results obtained from the samples indicate variable levels of maturity within the samples. Production index and hydrogen index values were plotted against Tmax values (Figure 3.19). Samples with TOC < 1.0 wt.% were included in the plots but were recognized as non-source rock samples. These plots are commonly used to establish source rock maturity. Results show both cores are within the oil window, however, Gill Land 2 core exhibit noticeably higher maximum temperatures (i.e. Tmax) and, higher level of maturity with samples falling in the condensate/wet-gas window. The average S2 values (i.e. remaining hydrocarbons potential) for Berthoud State 3 samples are higher (Table 3.3), possibly due to the maximum burial depth exhibited by this core in comparison to Gill Land 2 core samples. Vitrinite reflectance (Ro) values were not measured during this study, however calculated values are presented in (Table 3.2). Average calculated Ro for Gill Land 2 (i.e. 0.92) indicate early peak of wet gas generation (Table 3.3). In contrast, Berthoud State 3 calculated Ro (i.e. 0.75) suggest maximum oil generation state (Figure 3.20).

Table 3.3 Average source rock analysis values for the samples sorted by cores. Average was obtained for samples with TOC values of ≥ 1.0 wt%

Core	Depth	TOC	S1	S2	S3	Tmax	HI	OI	S1/TOC *100	PI
	ft.	wt. %	mg HC/g rock	mg HC/g rock	mg CO2/g rock	(°C)	mg HC/g rock	mg CO2/g rock	mg HC/g rock	ratio
2 Gill Land	6785.22	2.87	2.26	3.20	0.29	448.69	112.89	11.67	83.64	0.42
Berthoud State 3	3025.92	3.02	3.53	8.40	0.36	439.29	252.21	11.30	123.29	0.31

3.4 X-Ray Diffraction Mineralogy

Smoky Hill Member of the Niobrara Formation consists mainly of highly cyclic beds of chalk and marls. XRD mineralogy results for the 19 samples were compiled from previous studies (Table 2.2). Carbonates in the form of calcite and minimal dolomite constitute the majority of the rock samples examined (Figure 3.21 and Figure 3.22). Total clay volumes were highly variable with a range of (5-36%). Clay types were mainly illite and mixed layer illite/smectite. Chlorite and kaolinite were present only in two samples and one sample respectively. A positive relationship was observed between total clay and quartz content (Figure 3.23). The samples can be interpreted, based on their XRD mineralogy, as mixed

carbonate mudstones and carbonate-dominated lithotypes (Figure 3.24) following the organic mudstone classifications scheme of Gamero-Diaz et al. (2013).

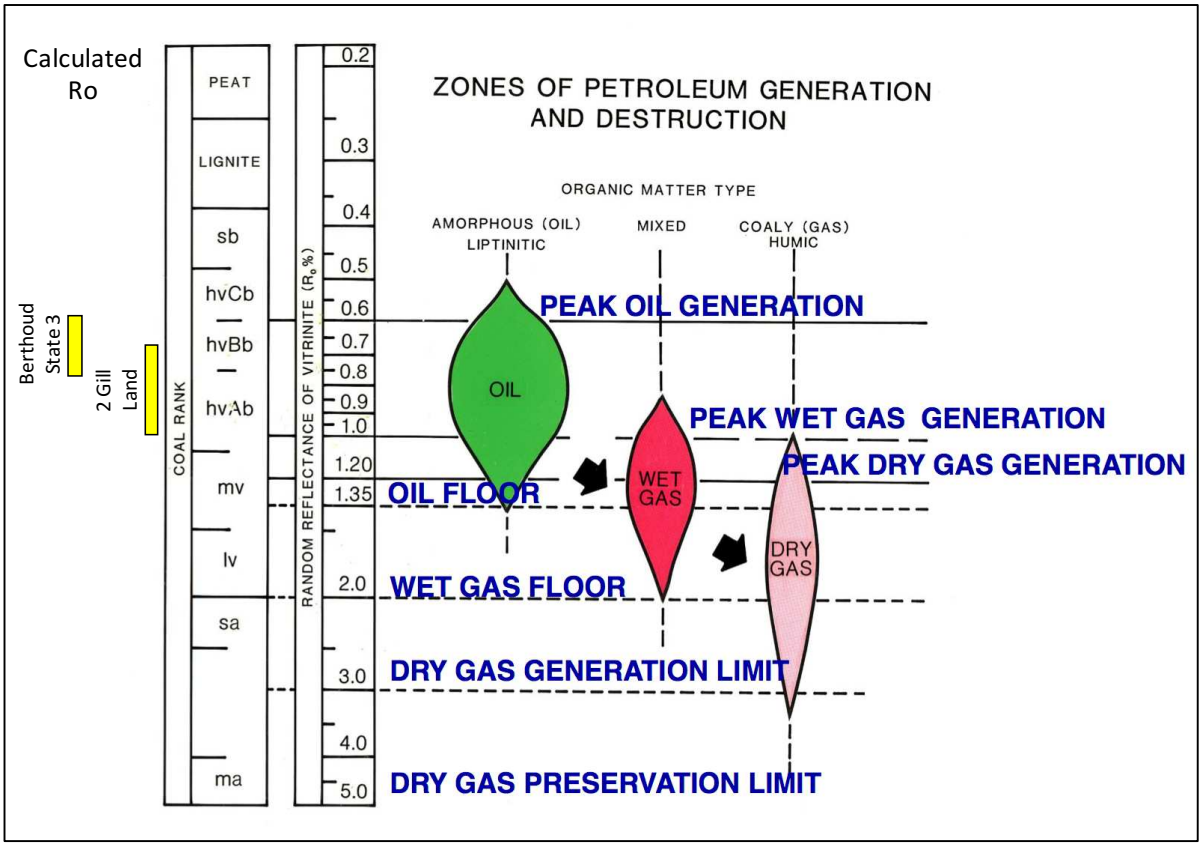


Figure 3.20 Vitrinite reflectance levels in reference to hydrocarbons generation and destruction windows. Range of calculated Ro for studied samples are noted with yellow bars. Modified from (Cardott, 2014).

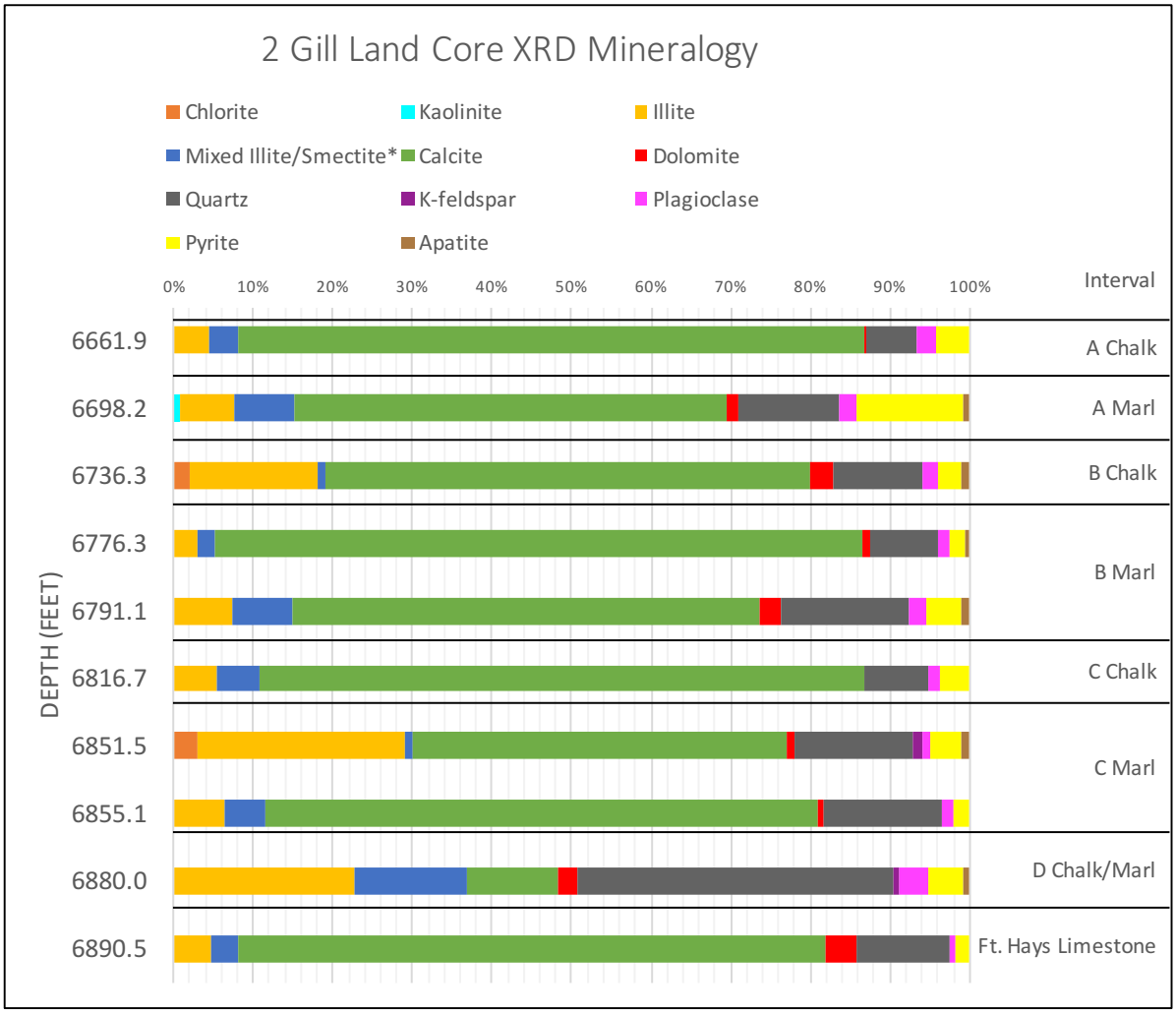


Figure 3.21 Summary of the XRD mineralogy for Gill Land 2 core samples. Samples are generally rich in carbonates with variable clay and quartz content.

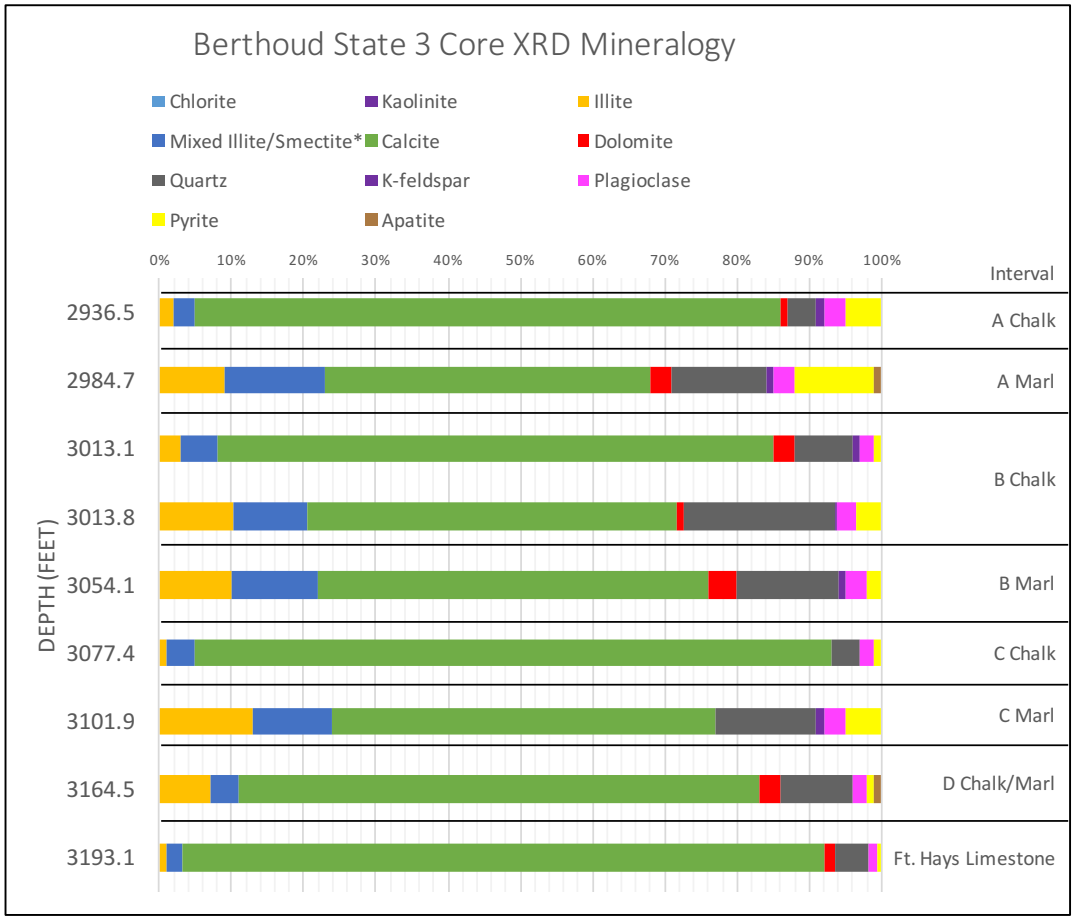


Figure 3.22 Summary of the XRD mineralogy for Berthoud State 3 core samples. Mineralogy variation is highly correlatable to Gill Land 2 core samples.

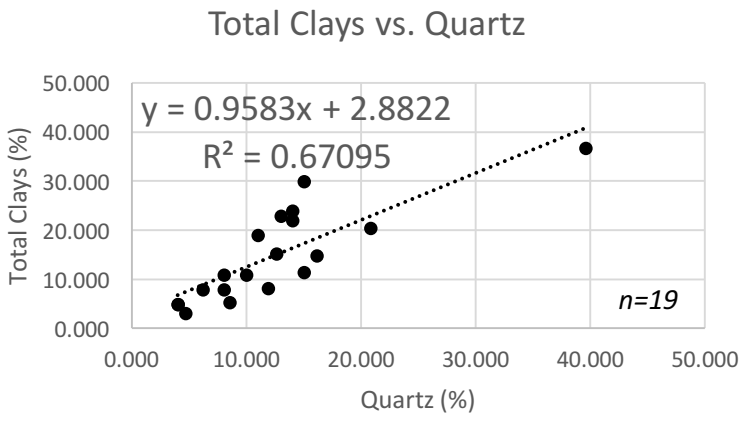


Figure 3.23 Crossplot of total clay versus quartz content. Positive excellent correlation is observed. Significance level is 0.05, calculated probability is 0.000018.

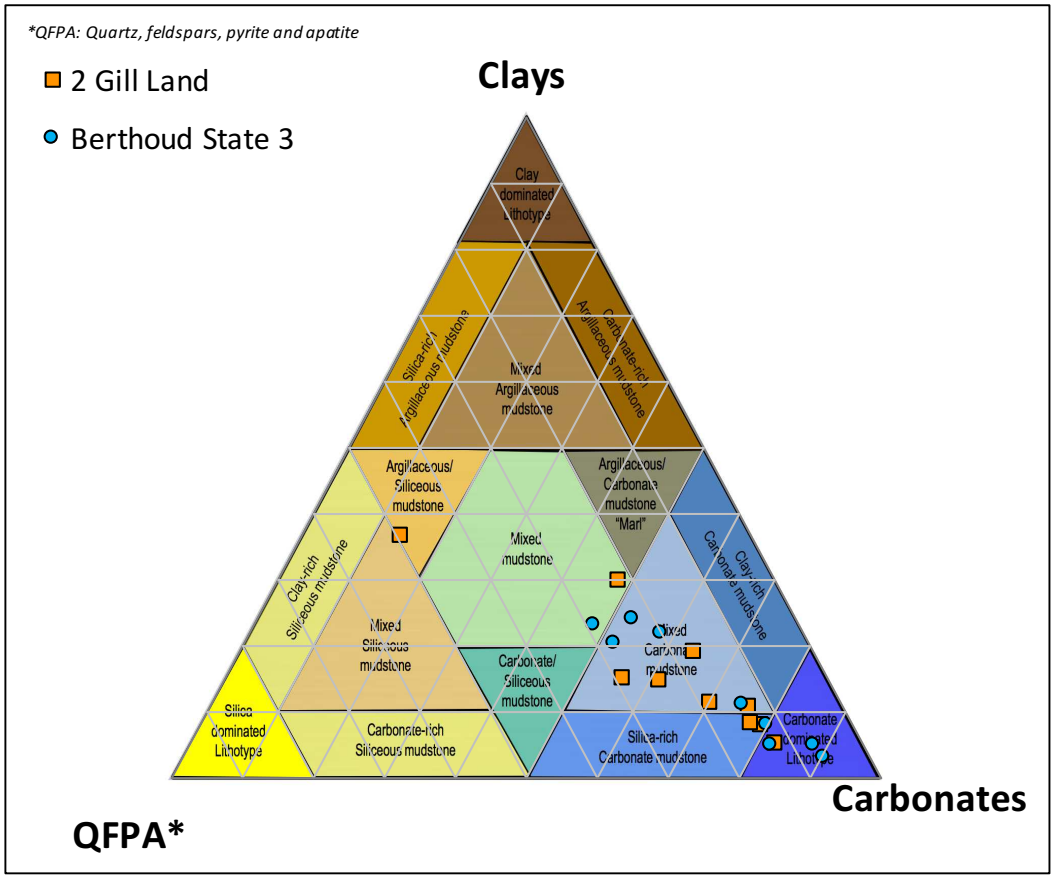


Figure 3.24 Ternary plot diagram of the XRD data. Reference grid is following the organic mudstone classification scheme (Gamero-Diaz et al., 2013). Plotted data can be interpreted as mixed carbonate mudstone and carbonate-dominated lithotype.

CHAPTER 4 DISCUSSION

The main objective of this project was to investigate the major parameters affecting the acoustic properties of Niobrara Formation. This chapter will discuss the effects of porosity, organic matter (richness and maturity) and mineralogy variation on the multidirectional velocity and anisotropy results presented in the previous chapter.

4.1 Porosity Effect

Porosity is an important controlling factor on ultrasound velocity. Effect of porosity on the sonic velocity of conventional rocks have been well documented in the literature (Castagna et al., 1985; Fabricius et al., 2005; Jones and Wang, 1981; Wyllie et al., 1956). This arises from the fundamental physics of waves travelling at higher speeds in closely packed medium and decreasing speed as voids are introduced.

Porosity for the Gill Land 2 core was acquired by Tanck (1997). Both helium and fluid core porosities were measured on 1-foot interval samples between (6719.5 - 6897.5 ft). Core porosity showed rather complex relationship when plotted against compressional velocity from well log (Figure 4.1). Although a trend can be observed, significance of correlation is marginal. A higher significance may arise with selective sampling. This suggests potentially more factors are controlling sonic velocity for examined samples.

Uncertainty in estimating core true porosity in organic and clay-rich formations was investigated by Saidian et al. (2015) for multiple mudrocks. By comparing multiple methods, porosity in shales cannot be determined by using a single method. However, water immersion porosimetry (WIP) was reliable for thermally mature samples with low expandable clay content whereas nitrogen adsorption yielded appropriate results for samples rich in organic-matter porosity. Therefore, WIP and nitrogen adsorption porosity measurements are recommended to obtain a quantitative analysis for the Niobrara formation porosity. For the purpose of this study a qualitative porosity indicator is sufficient to assess the velocity-porosity relationship. To facilitate a more accurate porosity data points for each sample, density porosity curve was calculated using the density porosity equation below:

$$\phi_{\mathrm{DPHI}} = \frac{\rho_{\mathrm{matrix}} - \rho_{\mathrm{bulk}}}{\rho_{\mathrm{matrix}} - \rho_{\mathrm{fluid}}} \tag{4.1}$$

Where: ρ_{matrix} is density of rock matrix, ρ_{bulk} is the bulk density of the sample and ρ_{fluid} is the fluid density in the pores. Matrix densities assumed for the Niobrara Formation are 2.67g/cc for chalk intervals and 2.70 g/cc for marls based on core analysis results

(ElGhonimy, 2015). Fluid density was assumed as 0.9 g/cc for wet gas window. This is an estimation compared to 0.7 g/cc used for gas wells in previous studies (ElGhonimy, 2015).

Calculated density porosity curve (Figure 4.2) indicates 1-6% higher porosity when compared to core WIP porosity. This could be an effect of the inaccessible kerogen and clay hosted pore or due to measurements precession and accuracy. Density porosity log was calibrated to core WIP porosity by applying a multiplier of 0.7. Core-calibrated density porosity results are presented in Figure 4.2. Average error of calibration is ±7%. Additionally, regression of the calibrated density porosity versus actual core porosity (Figure 4.3) indicates very high significance with p-value of $6.29e^{-14}$ (significance level for the correlation is 0.05).

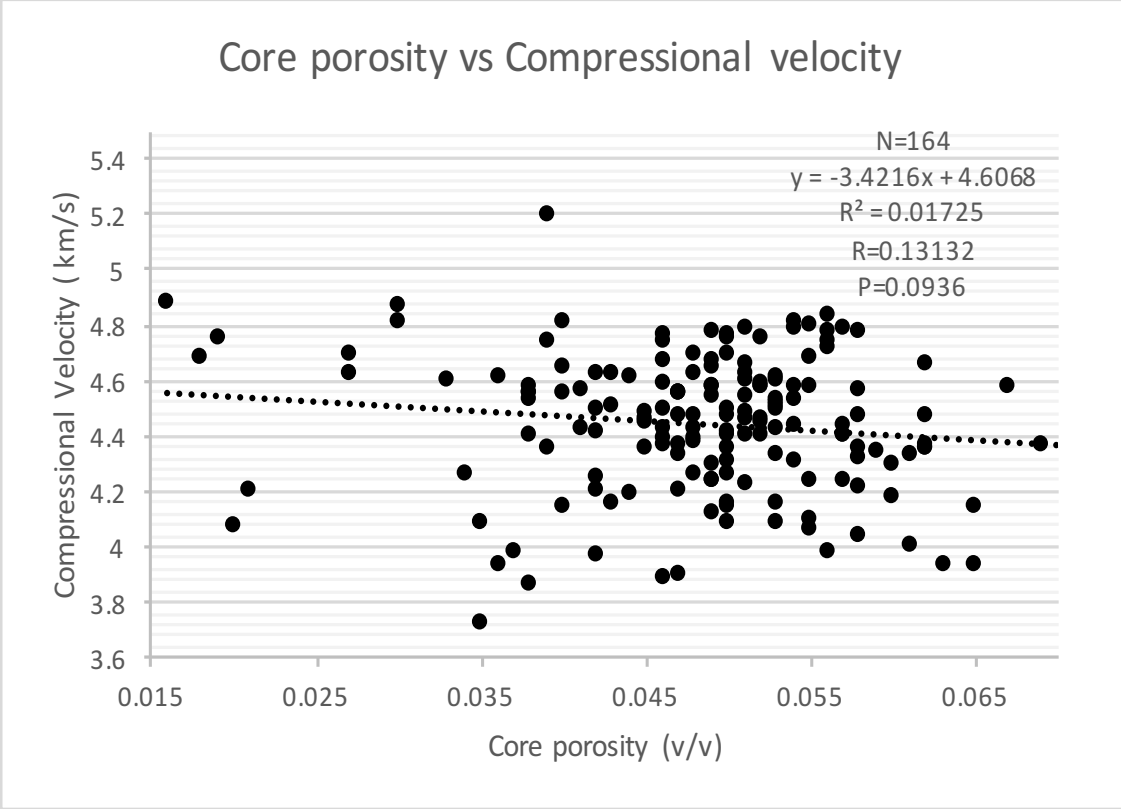


Figure 4.1 Compressional velocity from well log compared to core porosity for Gill Land 2 core. Number of samples is 164. P-value is 0.09, therefore correlation has marginal significance when compared to a significance level of 0.05.

Core-calibrated porosity values, when compared to measured velocities and calculated elastic parameters, suggest fair significance negative correlation when compared to C12 (i.e. parallel-to-bedding translational stiffness coefficient) values and good significance negative correlation when compared to parallel-to-bedding compressional to shear velocity ratio (i.e. Vp0/Vs0).

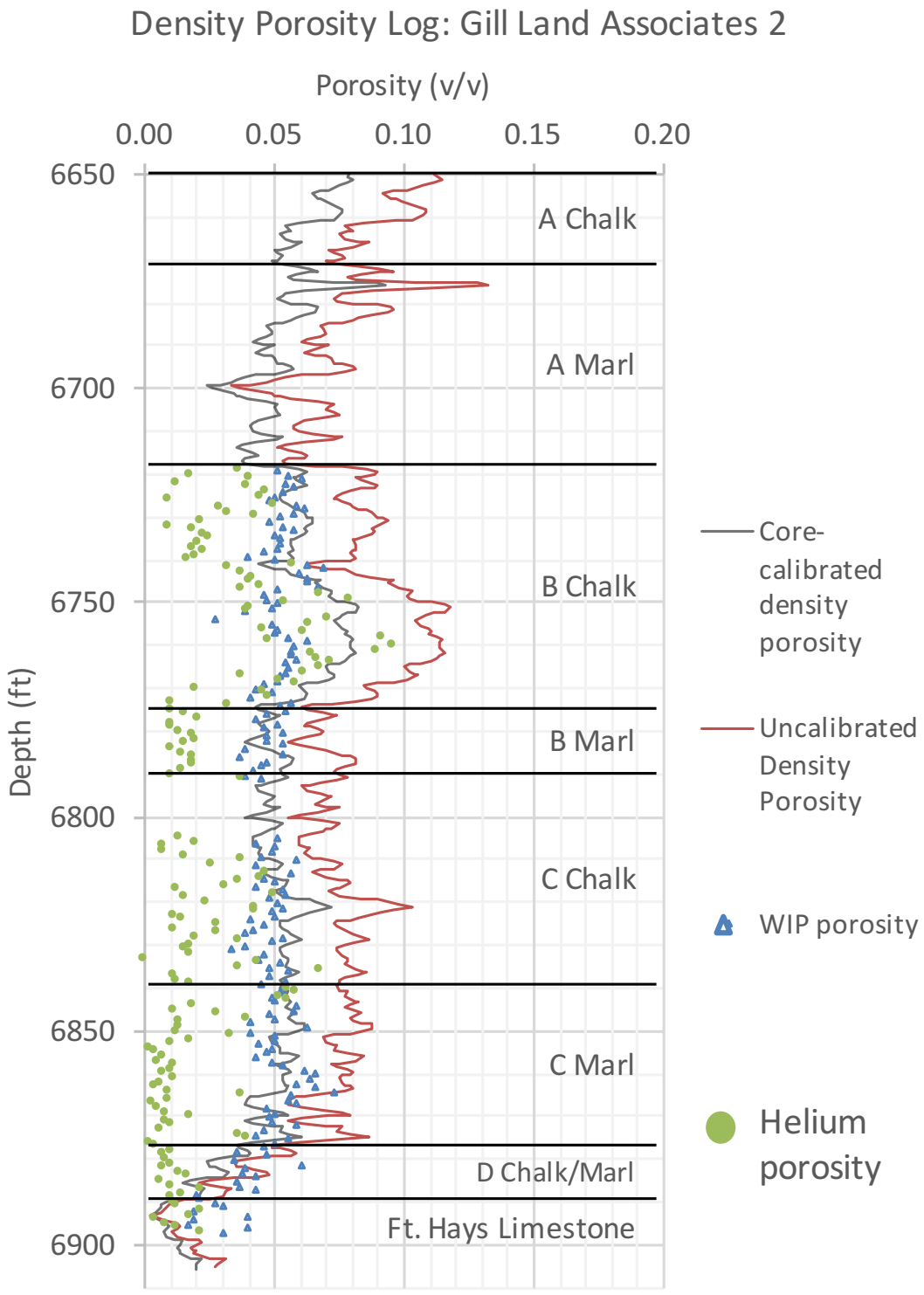


Figure 4.2 Calculated density porosity curve for the Gill Land 2 core Core. A core-calibration shift was achieved by applying a multiplier value of 0.7 to match the measured core porosity. Both types of core measured porosities are displayed for reference. Dphi was calibrated to WIP porosity specifically as helium is known to underestimate pore volume in tight samples.

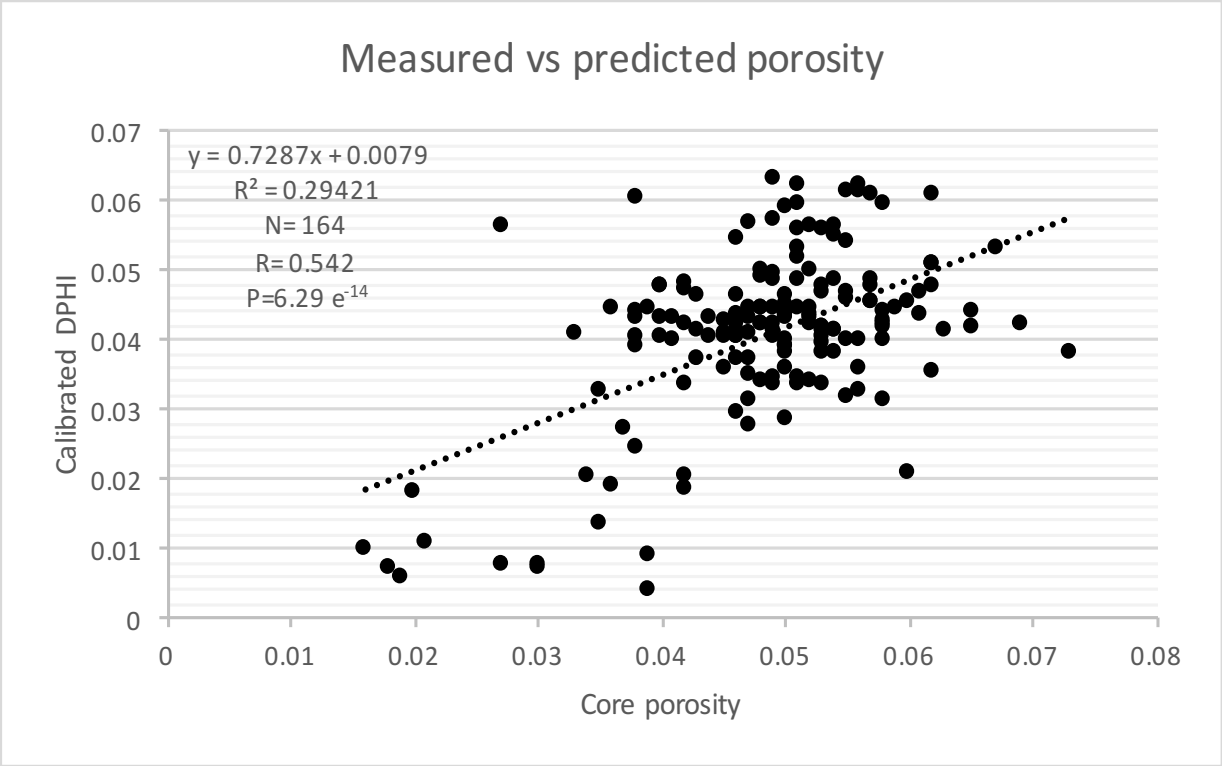


Figure 4.3 Crossplot of measured (horizontal axis) vs. calculated porosity (vertical axis). P-value of the regression indicate an excellent significance (significance level is 0.05).

It is important to note that C12 coefficient is dependent on Vp0, Vs0 and sample density (Figure 4.4). Core-calibrated porosity showed unexpectedly weak correlation to velocity and stiffness in the transverse direction. A significance level of 0.05 was used to determine significant correlations which equate to correlation coefficient (R^2) value of 0.63 or higher for a sample size of 10. Correlation to other velocities and stiffness coefficients yielded R-values less than the above threshold and were subsequently discarded (Table A.1).

4.2 Mineralogy Effect

Measured velocities, when compared to XRD mineralogy, show correlation coefficients of 0.49-0.62. Sample size is 19, therefore, the threshold for a correlation coefficient to be significant is 0.4683 (Table 2.4). A total of 66 statistically significant correlations exist (i.e. with R value higher than 0.4683) with ultrasonic measurements and wireline compressional slowness (DTCO). All the possible correlations are listed in Table A.2. Significant correlations with measured velocities exist for the 45 and 90 direction shear and compressional velocities. Carbonate content show positive relationship whereas pyrite and clays are inversely proportional to the compared velocities. Transverse compressional (C33)

and parallel shear (C44) stiffness coefficients show stronger correlation to the total carbonate volume and clay content with R value range 0.52-0.62. A positive correlation (i.e. R=0.52) exists between pyrite content and delta (***δ***) anisotropy. A similar but negative correlation exists for pyrite when compared to bulk modulus (K). Pyrite also seems to correlate to the responses of vertical Young's modulus and the parallel to bedding plane, v12 Poisson's ratio. Finally, quartz volume seems to correlate to the Vp45/Vs45 ratio with R=0.55 (Figure 4.5C).

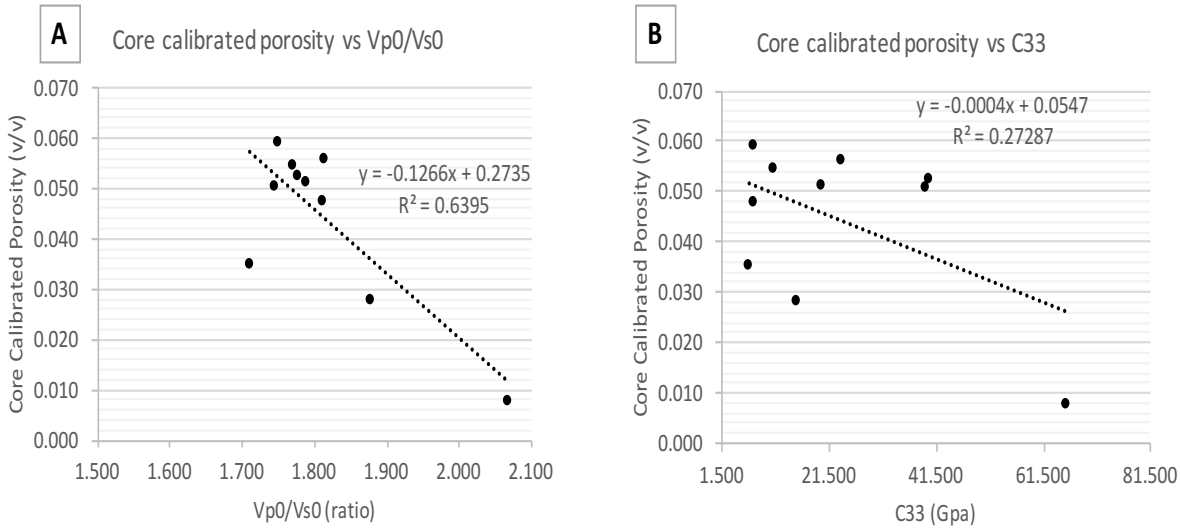


Figure 4.4 Crossplots showing core calibrated porosity for Gill Land 2 core samples versus: (A) Parallel to bedding compressional to shear velocity ratio, correlation p-value indicate good significance. (B) Transverse compressional (C33) stiffness coefficient Both crossplots indicate inverse relationship with porosity. C33 shows weak correlation significance to core-calibrated porosity. C33 coeffecient is dependant on Vp90 and sample denisty.

In summary, volume of illite present in the sample seem to cause a reduction in the 45 and transverse velocities. Total carbonate volume has the opposite effect. This effect is more observable on C33 and C44 stiffnesses (Figure 4.5A and B). As pyrite content increases, bulk modulus decrease, (i.e. compressibility is promoted by the presence of pyrite). Pyrite correlation content may be linked to an increased anoxic conditions. Anoxic conditions are necessary for the preservation of kerogen. Therefore, the increase of compressibility may rather by caused by higher kerogen content which is masked by the increase of pyrite volume.

Samples tested under variable confining pressure can be grouped in two groups: samples (3013.7, 3054.1 and 3101.9) have high clay content (average 20%), high carbonate content (average 53%) and relatively high quartz content (i.e. >14%) (Figure 3.22). In contrast, sample 3077.4 have low clay (5%), high total carbonates (88%) and low quartz content (4%).

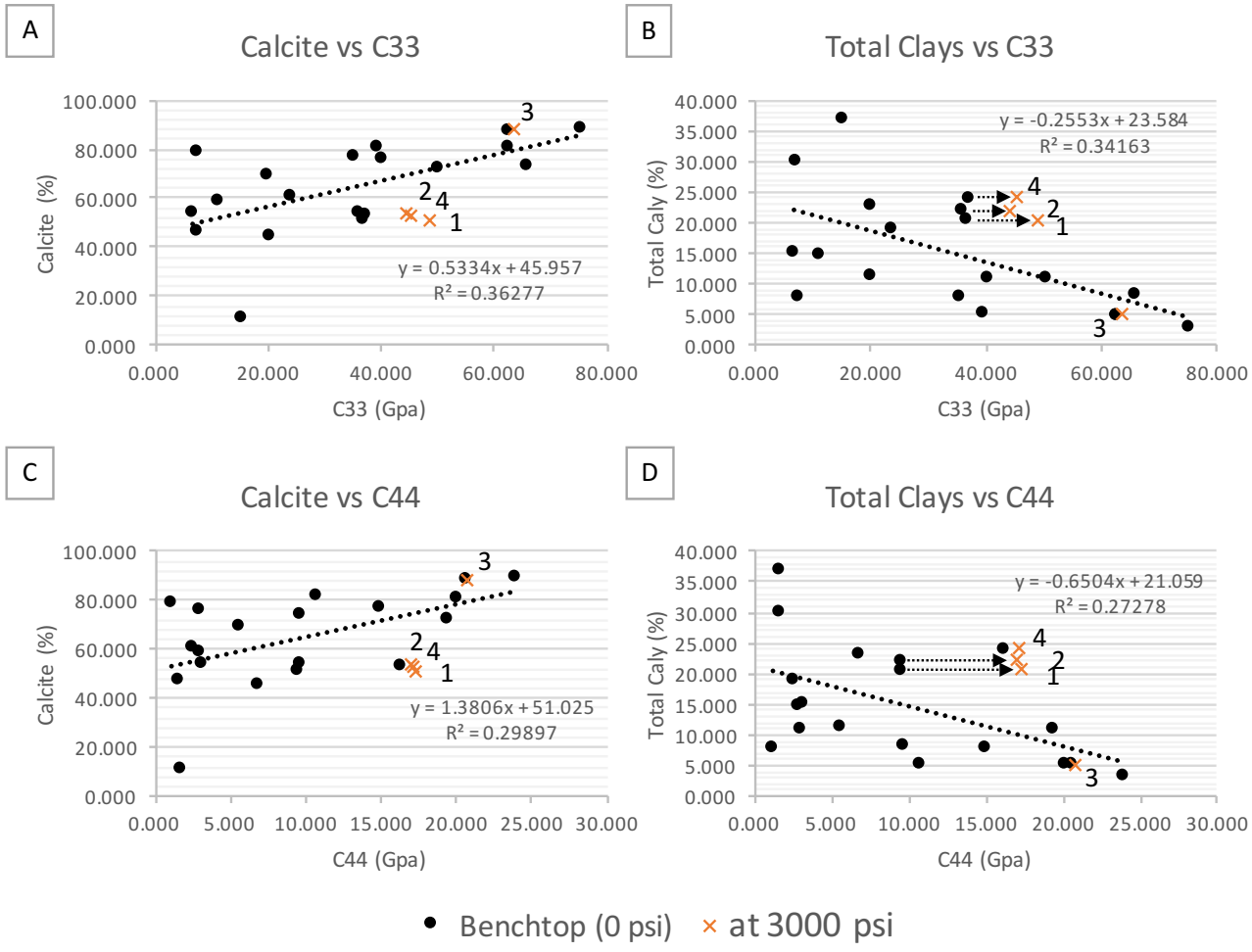


Figure 4.5 Crossplots showing samples of established mineralogy and ultrasonic parameters relationships with significant correlations. (A) and (B) show correlation with very good significance between C33 and calcite volume, and total clays vs. C33 respectively. (C) and (D) show lower significance correlation for C44 vs calcite content, and total clays vs C44 respectively. Four datapoints measured at 3000 psi are presented for reference but were not included in the regression. Pressure effect is observed as an increase in the C33 and C44 for each sample. Numbered samples are as follows: (1) B Chalk- 3013.75 ft, (2) B Marl-3054.1 ft, (3) C Chalk-3077.4 ft and (4) C Marl-3101.9 ft.

The observed responses when a pressure was applied are as follows: 3077.4 have overall higher velocities (Figure 3.10), no major velocity change in response to pressure increase, higher overall stiffness (Figure 3.13C) and much lower thomesen anisotropy values (i.e. 0.01-0.06 compared to a range of 0.1-0.4 for the other three samples), samples (3013.7, 3054.1 and 3101.9) show decrease in anisotropy with increasing applied pressure while 3077.4 sample showed overall stable values against variable confining pressure, sample 3101.9 compressibility dramatically decreased with pressure (Figure 3.17) which is conformable with the results obtained from the larger dataset above as this sample contains the highest pyrite content (i.e. 5%) in the confined pressure dataset and finally, 3077.4 sample Poisson's ratio showed very subtle response to pressure increase (Figure 3.18). By comparison, other samples indicated noticeable variation in their respective Poisson's ratios.

In comparison, (Maldonado, 2011) tested three outcrop samples representing lower marl, D chalk and Ft. Hays limestone. The aforementioned study samples were only measured for compressional velocity, pressure range was different (i.e. 1740-8000 psi) and the chalk sample was only tested for vertical velocity. Regardless, lower marl sample results are conformable with the velocities measurements in this study in general, although the D chalk sample yielded much higher rate of velocity change in response to pressure increase (Figure 1.9; Figure 1.10). D chalk was not measured under confining pressure for this study, however, D chalk sample from (Maldonado, 2011) indicate high clay content (22%) and lower calcite (~48%) which can be compared to the three clay-rich samples in this study.

4.3 Effects of Organic richness and Maturity

TOC and maturity data for the samples were compared to all the measured velocities and their respective elastic parameters. Total number of samples both sonic measurements and total organic content (TOC) is 19 samples, therefore the threshold for a significant correlation is R=0.4683 or R^2 =0.2193. All samples with TOC less than 1 wt.%, their respective source rock analysis (SRA) data were eliminated. This resulted in a smaller number of samples with valid SRA data to 14 samples. Consequently, this has restricted the acceptable correlation value to R=0.5324 or R^2=0.2834. Established number of significant correlations is 64 with lab ultrasonic data and 4 significant correlations with wireline logs (Figure 4.6; Table A.3).

Total organic content: higher organic content seems to coincide with a decrease in the transverse compressional (C33) and parallel translational (C12) stiffness coefficients. C12 decrease is exponential in response to change in TOC wt.% (Figure 4.7). C33 response may be caused by a combination of two factors: (a) the characteristic lower stiffness of kerogen in

comparison to the rock matrix stiffness and (b) kerogen form in horizontal laminae in source rocks. Although C12 is function of both C11 and C66, none of the later showed significant correlation within this dataset. For the same TOC level, C33 seems to increase as pressure is applied. Clay content showed similar relationship to C33 and C44. TOC did not reveal a valid correlation with C44 for this dataset. However, this could be an effect of the number of samples tested. The similarity in C33 response to both clay content and TOC richness suggests that most likely both factors affect the transverse stiffness as they both have lower stiffness compared to the rock matrix stiffness. Furthermore, the observed relationship is conformable with results obtained from a larger dataset combining samples from multiple source rocks from various basins (Prasad et al., 2011). The aforementioned study combined kerogen with total porosity (Figure 4.8). C12 correlation to TOC shows fair to good significance (i.e. P-value =0.016).

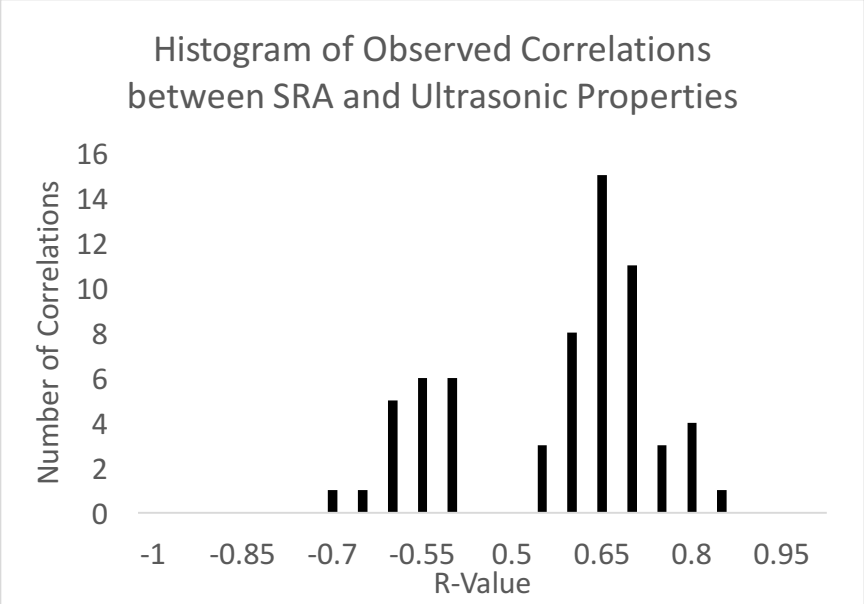


Figure 4.6 Histogram analysis of the established correlations between SRA data and observed ultrasonic properties. Any correlation with R value between 0.5 and -0.5 was eliminated due to insignificancy.

Existing producible hydrocarbons (S1): values of S1 from SRA varied between 0.6 – 5.4 mg HC/g rock. Correlations of S1 with major significance exist with: shear velocity in the 45 direction (Vs45), transverse compressional (C33) and transverse shear (C44) stiffness coefficients. C44 versus S1 yielded the highest significance correlation (R^2=0.45).

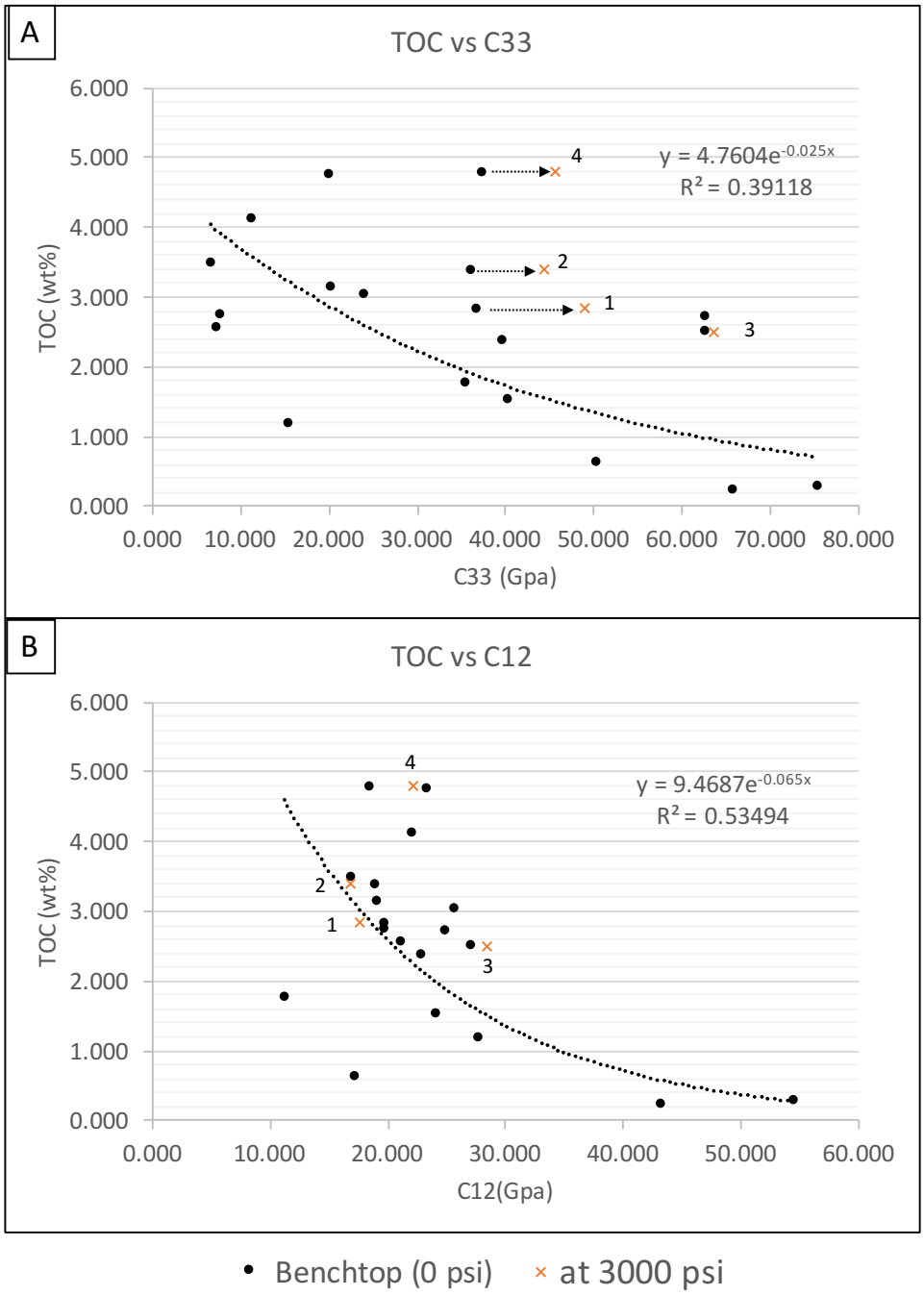


Figure 4.7 TOC effect on C33 (A) and C12 (B) stiffness coefficients. Number of samples= 19. Samples measured under 3000 psi confining pressure are presented. Numbered samples are as follows: (1) B Chalk- 3013.75 ft, (2) B Marl-3054.1 ft, (3) C Chalk-3077.4 ft and (4) C Marl-3101.9 ft.

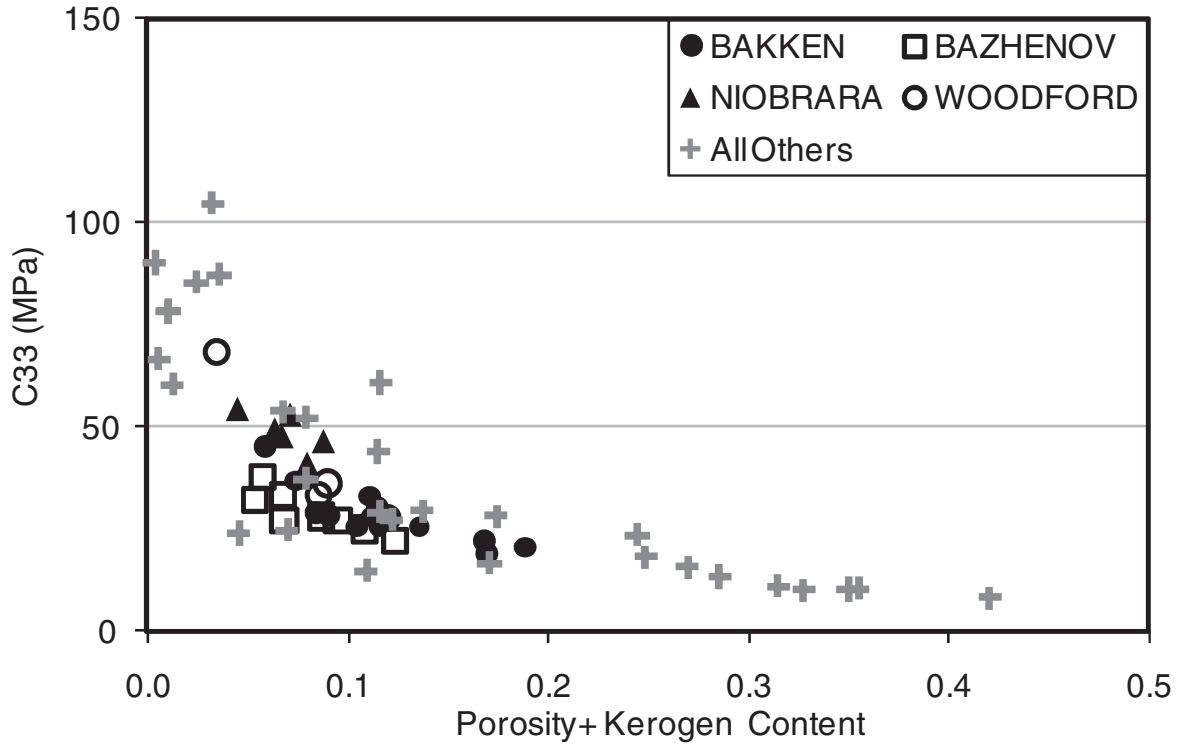


Figure 4.8 C33 vs. (porosity and kerogen content) for multiple source rocks (Prasad et al., 2011). Data for Niobrara from this study are presented in Figure 4.7.

Change in respect to Vs45 is linear compared to polynomial for C33 and C44. In contrast to kerogen, presence of hydrocarbons seems to increase the transverse stiffness coefficients. When compared to C33, C44 shows much higher relative increase when subjected to 3000psi pressure (Figure 4.9).

Potential hydrocarbons (S2): This SRA parameter measures the potentially producible hydrocarbons upon thermal cracking. S2 was observed to have significant correlations with Vs/Vp45 ratio, Vs90 and the wireline measured compressional slowness (DTCO). Relationship with compressional slowness has the highest correlation significance with R^2 value of 0.56 (Figure 4.10) . Higher S2 (i.e. lower maturity) content seem to promote the shear velocity in the 45 and 90 while slowing down the overall compressional wave velocity, at least in the 0 and 45 directions.

CO2 produced due to thermal cracking (S3): samples with higher S3 values were associated with slower compressional velocity, faster shear velocity in the 45 direction and higher *v*31 Poisson's ratio (X1/X3). Both S3 and S2 are comparable when each are correlated to Vs/Vp45 and DTCO.

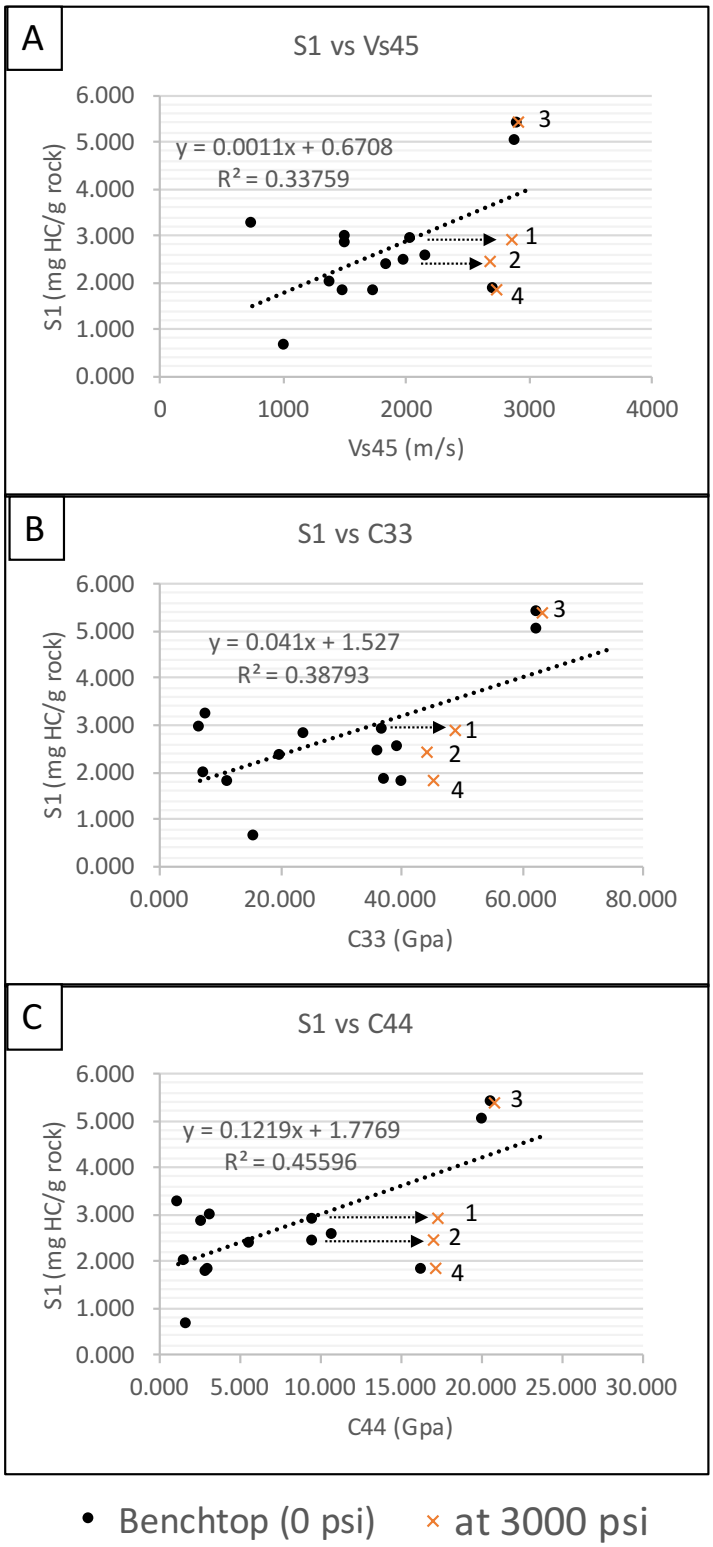


Figure 4.9 Vs45 (A), C33 (B) and C44 (B) correlation to S1 values. S1 vs. C44 yielded the highest correlation coefficient. Number of samples is 14. Numbered samples are: (1) B Chalk-3013.75 ft, (2) B Marl-3054.1 ft, (3) C Chalk-3077.4 ft and (4) C Marl-3101.9 ft.

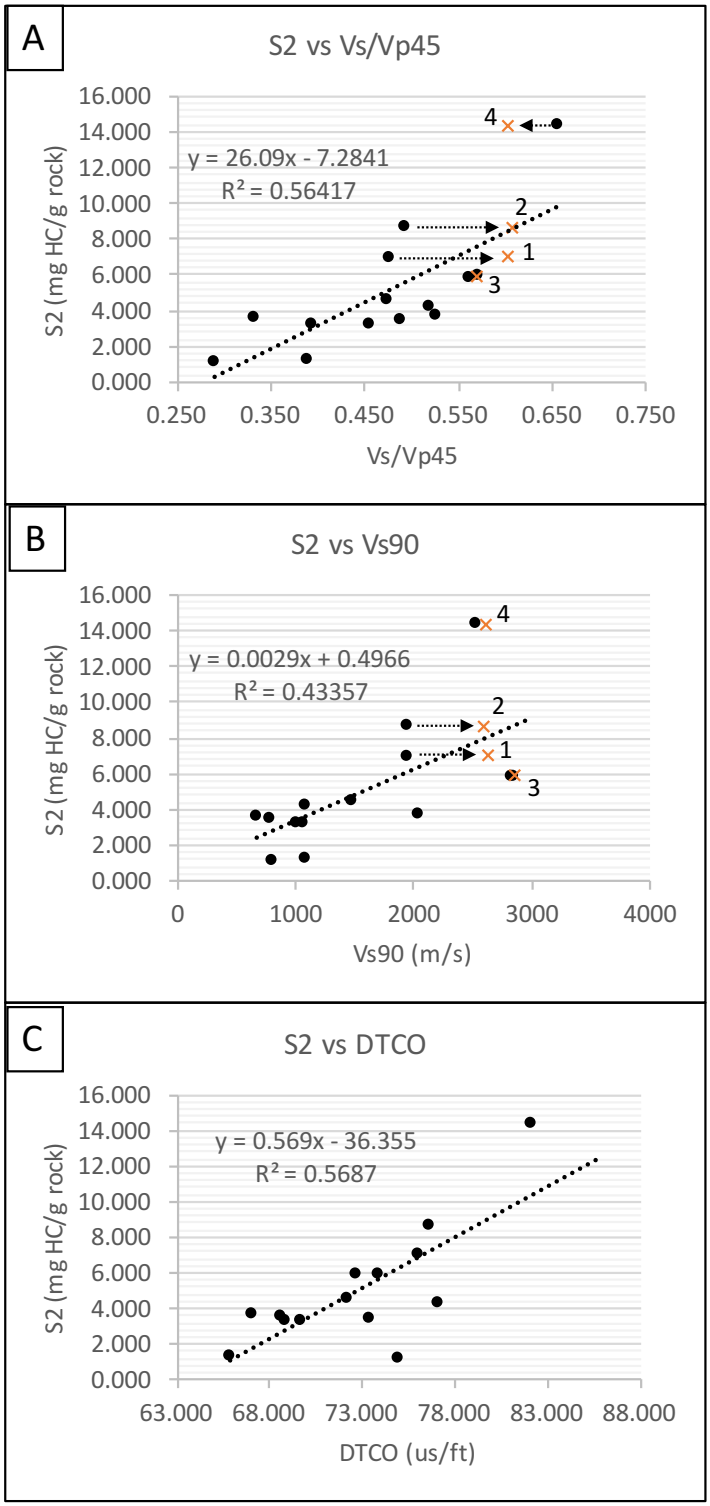


Figure 4.10 Vs/Vp45, Vs90 and DTCO correlation with S2 values. S2 vs. DTCO shows an excellent correlation significance. Number of samples is 14. Numbered samples are as follows: (1) B Chalk- 3013.75 ft, (2) B Marl-3054.1 ft, (3) C Chalk-3077.4 ft and (4) C Marl-3101.9 ft.

This is caused by the diagenetic link in the process of pyrolysis, as the amount of CO2 produced during pyrolysis is related to the thermally cracked hydrogens during S2 pyrolysis phase (Figure 4.11).

Hydrogen index (HI): in general, lower HI values may suggest lower maturity of the analyzed sample. Hydrogen index shows significant linear correlations to two wireline logs and three acoustic benchtop velocities. Both compressional slowness and deep resistivity logs show increased values in response to a higher hydrogen index. Slower compressional velocity in response to increasing hydrogen index pattern has been previously documented in a larger source rock dataset (Prasad et al., 2011). Although a marked increase in Vp0 was observed in the larger dataset when HI<200, this was not observed in this dataset. Vertical shear, 45 degrees shear and vertical compressional velocities also show positive significant correlation to hydrogen index (Figure 4.12). All correlations indicate moderate significance except Vs90 which yielded R^2 of 0.64. Hydrogen index is dependent on the S2 and TOC values, thus the increase in wireline compressional slowness as well as vertical velocity and Vs45 was also observed with higher S2 values (Figure 4.10). When a confining pressure is applied, vertical shear velocity increases whereas vertical compressional velocity decreases.

Oxygen Index (OI): Vp/Vs0 ratio has a fairly significant proportional correlation when compared to measured OI (Figure 4.13). This parameter is diagenetically linked to S3 as the oxygen measured is a function of the CO2 released by thermal cracking. Vp/Vs0 ratio decreases for B chalk and marl samples when a pressure is applied. In contrast, C chalk and marl samples showed an increase in their respective Vp/Vs0 ratio.

Tmax and calculated vitrinite reflectance R_0: Vitrinite reflectance is calculated for this dataset and therefore it is dependent on Tmax. Tmax revealed a correlation with C33 (Figure 4.14) with weak marginal significance (i.e. $R^2 = 0.286$).

4.4 Estimating Organic Richness and Maturity

One of the main objectives for this study is to assess any potential indications of source rock richness and maturity using acoustic wireline measurements. Several relationships have been established based on lab measurements and documented accordingly in the previous section. Modelled equations with highest significance (Figure 4.7; Figure 4.10; Figure 4.12; Figure 4.13) have been used to calculate TOC, S2, hydrogen index and oxygen index for the Aristocrat PC H11-07 core. Shear and compressional wireline velocities as well as density log are available for this well and were used to calculate C11, C66 and C12 correlation coefficients.

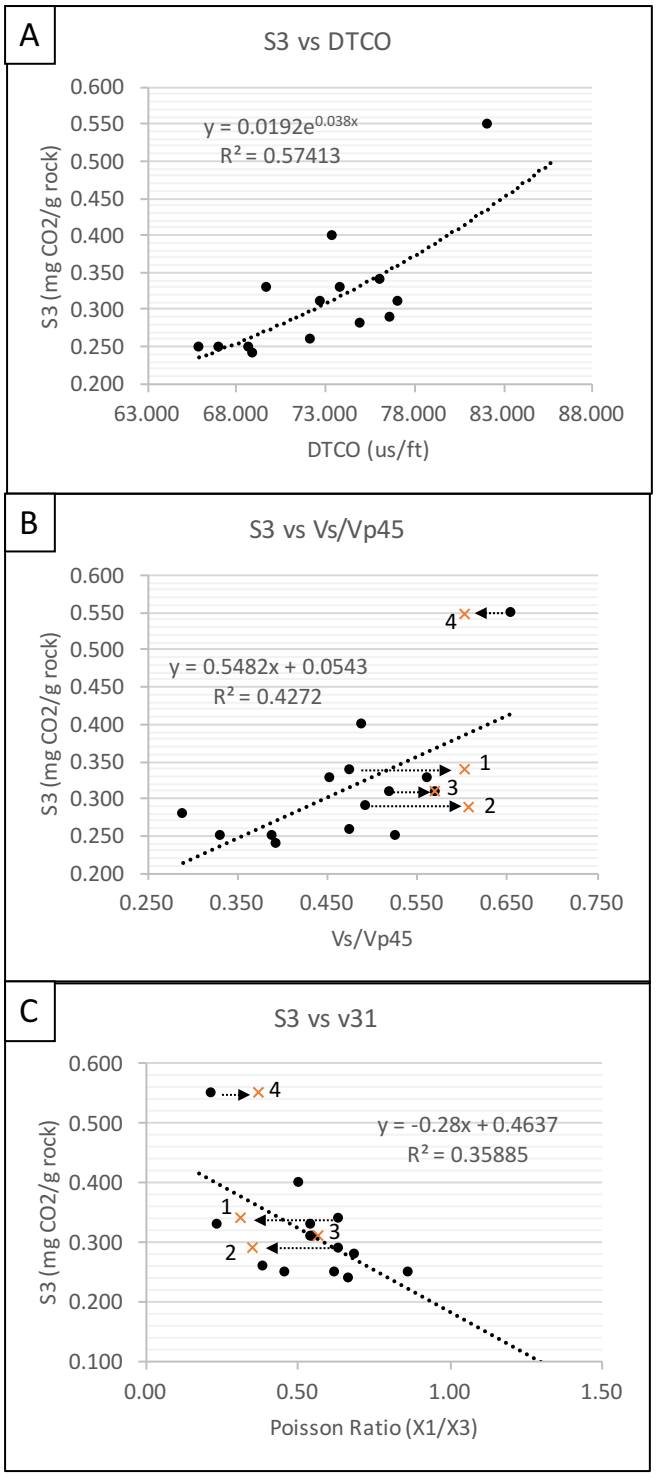


Figure 4.11 DTCO, Vs/Vp45 and *v*31 correlations to S3 content. Numbered samples are as follows: (1) B Chalk- 3013.75 ft, (2) B Marl-3054.1 ft, (3) C Chalk-3077.4 ft and (4) C Marl-3101.9 ft. Correlation results are comparable to S2 crossplots in Figure 4.10.

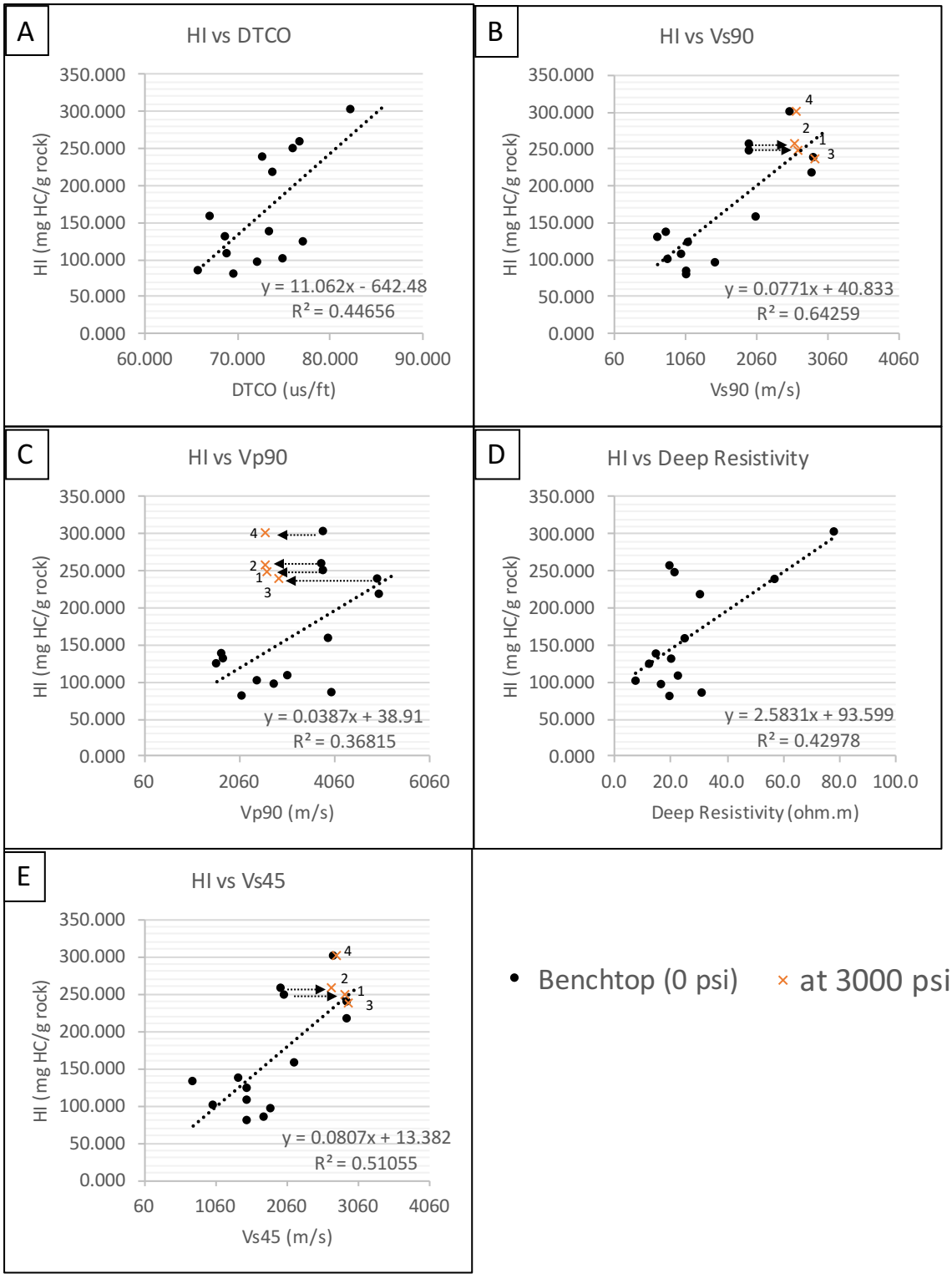


Figure 4.12 DTCO, Vs90, Vp90, deep resistivity and Vs45 linear correlations with hydrogen index (HI). Numbered samples are as follows: (1) B Chalk- 3013.75 ft, (2) B Marl-3054.1 ft, (3) C Chalk-3077.4 ft and (4) C Marl-3101.9 ft. Number of samples=14.

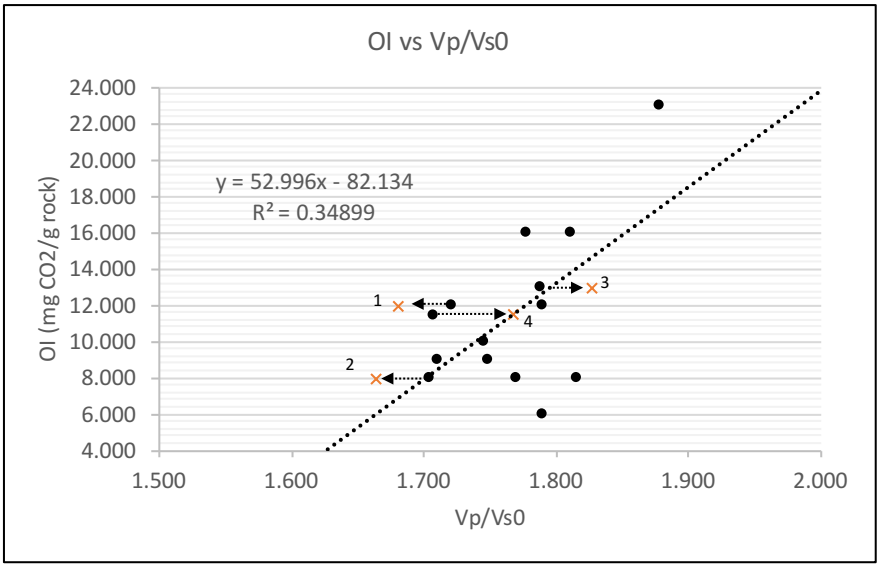


Figure 4.13 Oxygen index compared to Vp/Vs0 ratio. The correlation has fair significance based on number of samples=14. Numbered samples are as follows: (1) B Chalk- 3013.75 ft, (2) B Marl-3054.1 ft, (3) C Chalk-3077.4 ft and (4) C Marl-3101.9 ft. Number of samples=14.

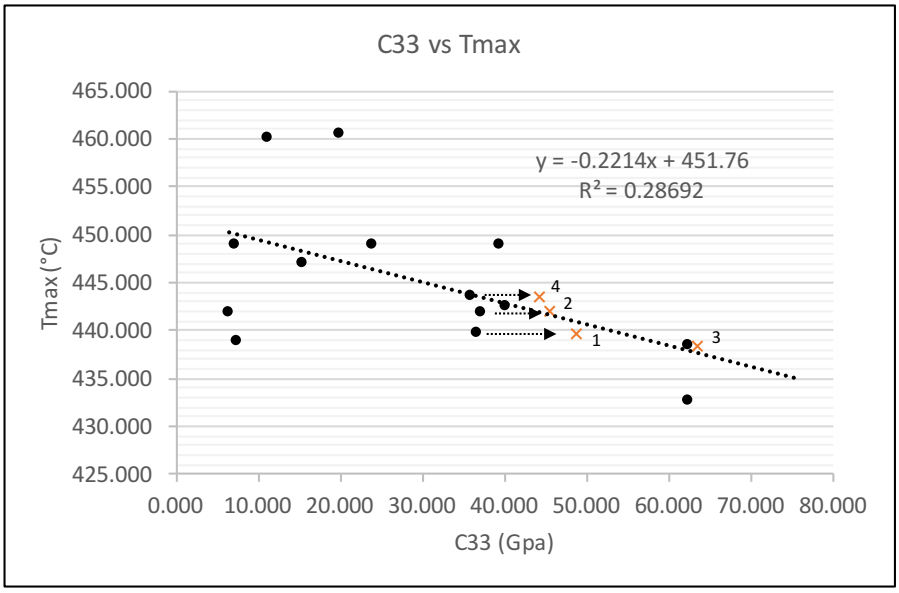


Figure 4.14 Tmax correlation with C33. Correlation shows weak marginal significance. Numbered samples are as follows: (1) B Chalk- 3013.75 ft, (2) B Marl-3054.1 ft, (3) C Chalk-3077.4 ft and (4) C Marl-3101.9 ft.

The core has been studied previously and source rock analysis data points were acquired on a 2-4 ft. resolution (ElGhonimy, 2015). Actual measured datapoints were used to verify accuracy and validity of the prediction models (Figure 4.15). The modelled equations used to calculate TOC, S2, HI and OI are as follows:

$$TOC = 9.4687e^{-0.065*C_{12}} \quad (4.2)$$

$$S2 = 0.569 * DTCO - 36.355 \quad (4.3)$$

$$HI = 11.062 * DTCO - 642.48 \quad (4.4)$$

$$OI = 52.996 * {}^{V_{P0}}/_{V_{S0}} - 82.134 \quad (4.5)$$

These models were calculated based on significant correlations of lab-measured source rock analysis data compared to ultrasonic lab measurements. Results from samples with TOC<1 wt.%, including the Ft. Hays limestone samples, were eliminated due to high uncertainty in analysis results. Models prediction results can be summarized as follows:

Total organic content (TOC): predicted TOC closely follows the trend of the lab measured TOC levels. Estimated values have an error average of ±0.83 wt.% (Figure 4.16). Lower error values are observed in marly or clay-rich intervals across the Smoky Hill Member (Figure 4.15). Overall, predictive model may be used for qualitative assessment of intervals within the Smoky Hill Member.

Potential hydrocarbons (S2): predicted S2 values results show overpredicted values when compared to measured S2 values. Error in prediction range between +0.1 to +12 with an average value of +3.862 mg HC/g rock (Figure 4.16). Predicted values error in chalk-dominated zones is much lower: +0.2 to +1.7. Modeled values can be used only in a qualitative assessment within low-clay zones with high speculation.

Hydrogen Index (HI): hydrogen index is a function of S2 and TOC values. Prediction values are noticeably more representative in chalk-dominated zones (Figure 4.15). Error range is -50 to +250 with an average of +105.9 mg HC/g rock. Model is interpreted to be erroneous based on the current dataset. Larger dataset may be needed before an assessment of validity can be made.

Oxygen Index (OI): Predicted values generally under-estimate the true oxygen index across zones with relatively lower TOC levels. Error range varies between -35 to +23 with an average value of -10.64 mg CO2/g rock (Figure 4.17). Model may be used to assess the oxygen index in relatively organic-rich zones across the Smoky Hill Member.

Previous work to estimate TOC from logs by ElGhonimy (2015) concluded the following:

- Schmoker method (Schmoker, 1983) over-estimated TOC in marls while overestimating TOC in chalks.
- Delta log R (Passey et al., 1990) showed very poor match (Figure 4.18) due to high uncertainty in level of organic maturity. Additionally, resistivity in chalks was responding to lithological changes rather than maturity.
- Uranium method: in which a regression was established between core measured TOC, gamma ray and spectral uranium logs. Although the calculated regressions yielded very low correlation coefficients (Figure 4.19), it was concluded to be the best estimate of TOC as it showed overall similar trend to measured TOC.

Equations presented in Figure 4.19 were used to calculate the predicted TOC from total gamma ray and spectral uranium logs. This was done to replicate the results obtained by (ElGhonimy, 2015). A comparison between the TOC predicted by the method proposed in this study and the uranium/GR method is presented in Figure 4.20. TOC predicted by the regression between spectral uranium log and actual TOC measurements showed fair to moderate fit to actual core TOC. Calculated TOC was overpredicted in chalk intervals and under-predicted in marl intervals. Additionally, this method relies completely on the availability of core TOC measurements for the subject well or core. In contrast, the method presented in this study shows moderately qualitative TOC prediction based on wireline shear and compressional acoustic logs. Finally, the uranium method can generate higher accuracy TOC predictions in B Marl sub-member whereas the method presented in this study yield better estimates for the C Marl sub-member.

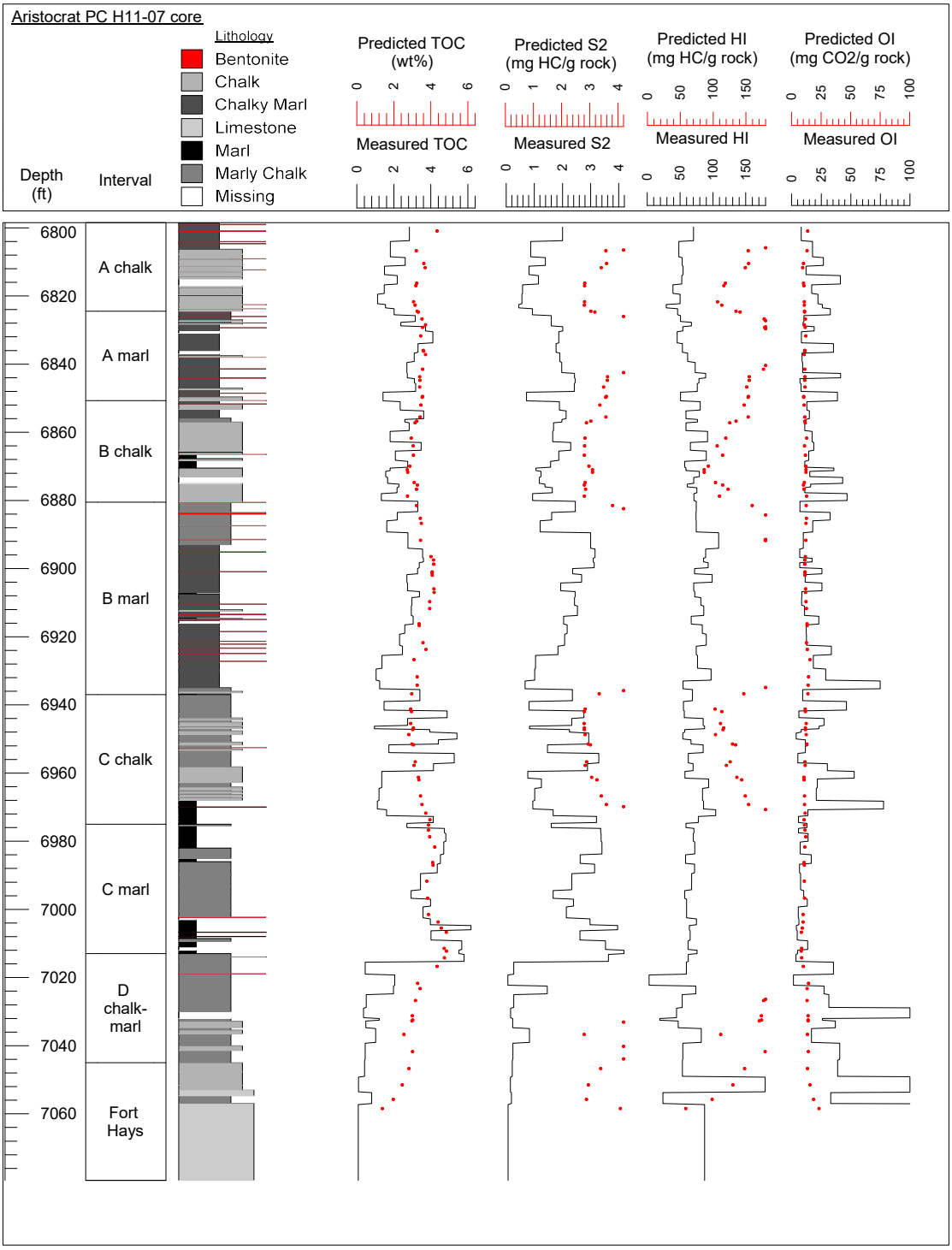


Figure 4.15 Measured vs. predicted source rock richness (TOC) and maturity: (S2, hydrogen index HI and oxygen index OI) based on lab generated prediction models. Data displayed for Aristocrat PC H11-07 core. Measured data points and core description are courtesy of ElGhonimy (2015).

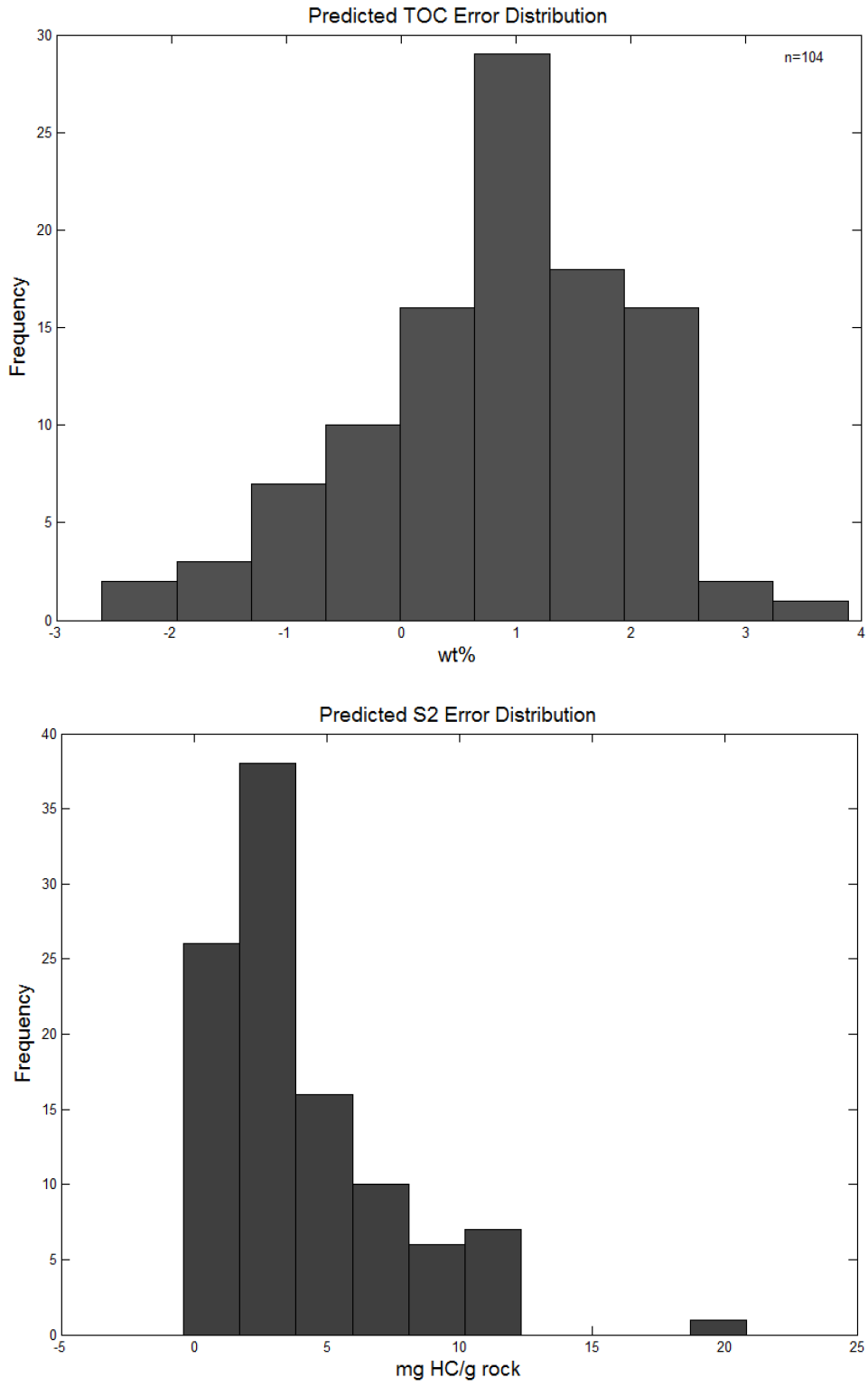


Figure 4.16 Error distribution for predicted TOC and S2 values.

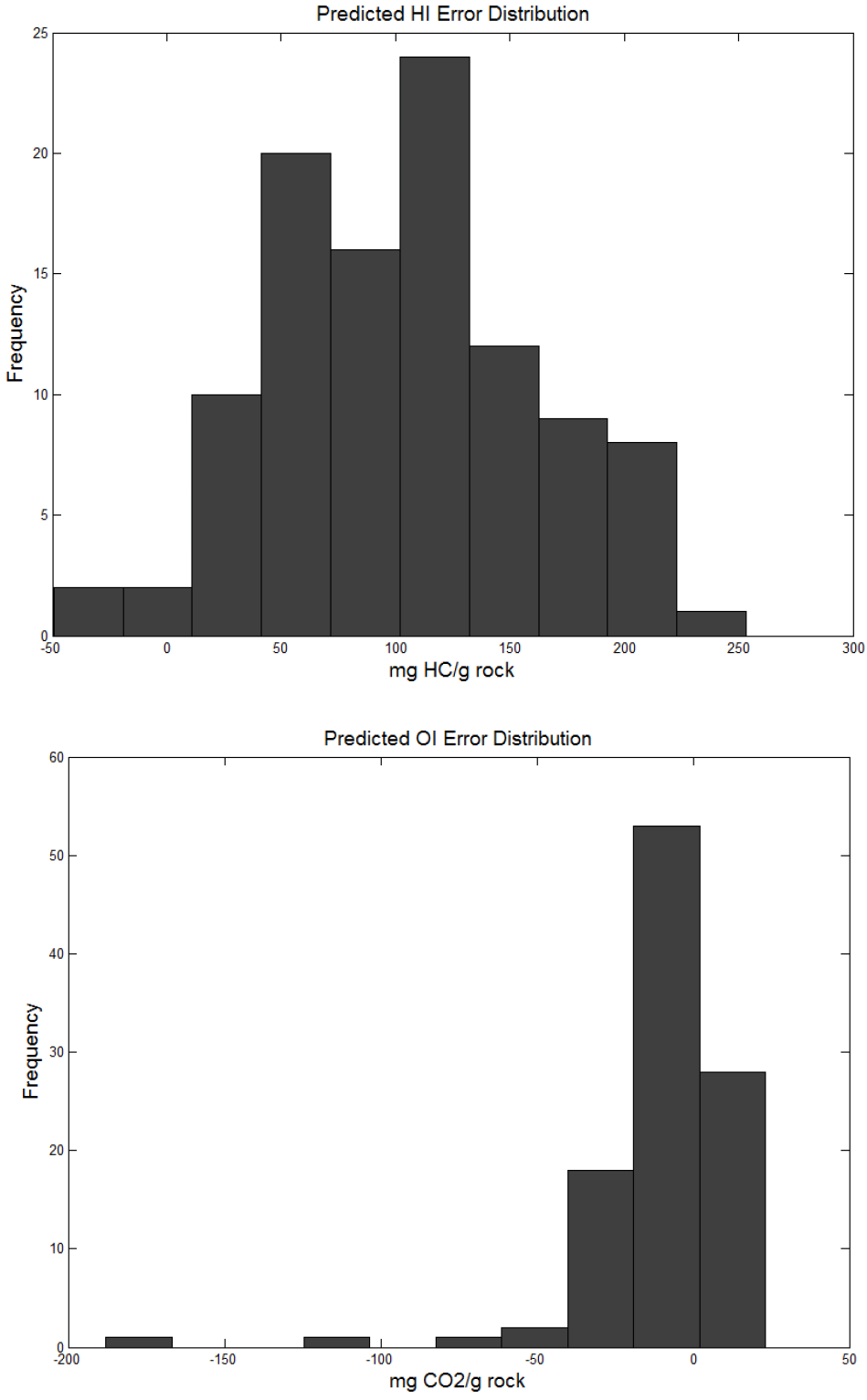


Figure 4.17 Error distributions for predicted HI and OI values.

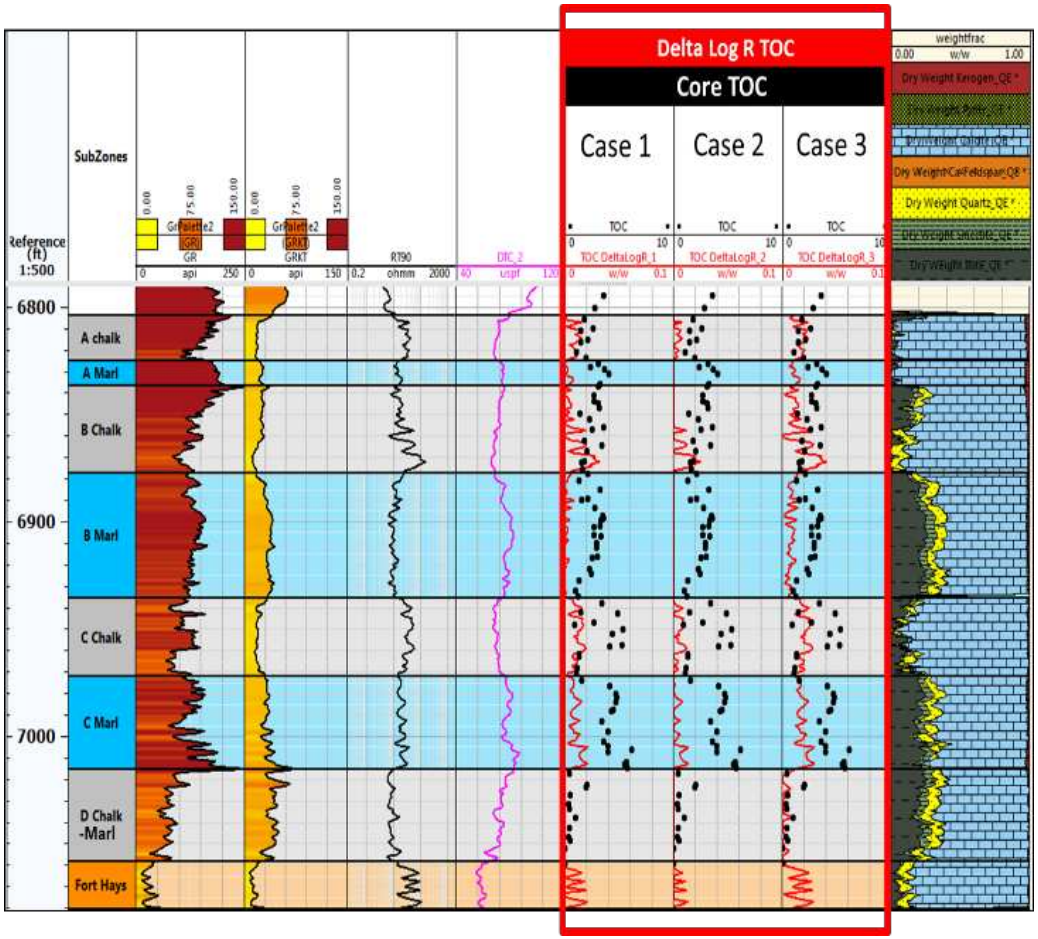


Figure 4.18 Predicted TOC by delta log R method compared to core TOC (ElGhonimy, 2015). Three cases were calculated using three different resistivity baselines.

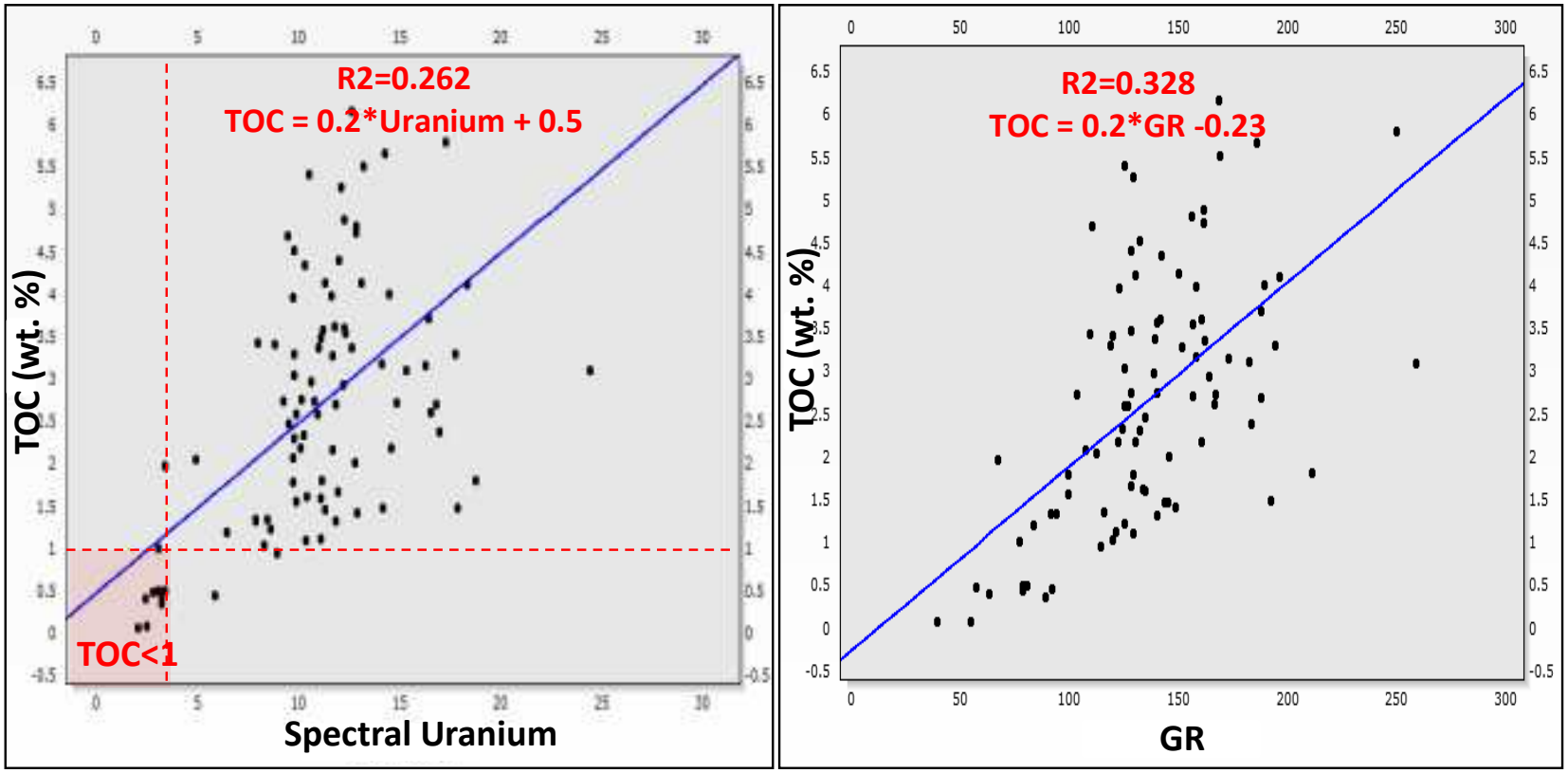


Figure 4.19 core TOC vs spectral uranium and total GR logs. Regressions calculated were used to predict TOC from uranium and total GR logs in ElGhonimy (2015)

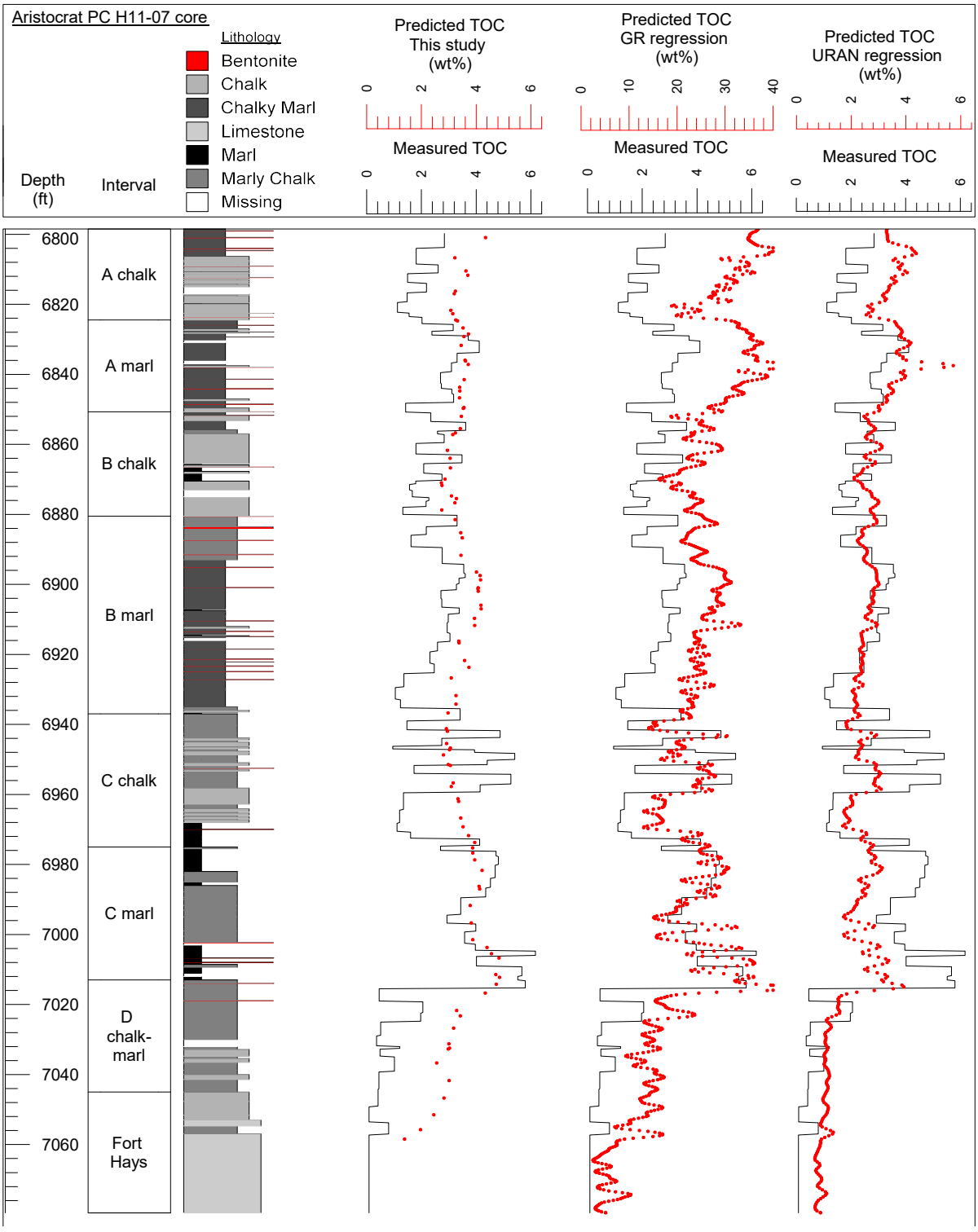


Figure 4.20 comparison of TOC prediction for Aristocrat PC H11-07 core using: this study method (track1), ElGhonimy (2015) regressions based on core TOC, GR and spectral uranium logs (tracks 2 and 3). The GR estimated TOC is six times higher than the core TOC. Uranium method shows the best fit to core data across the B Marl interval whereas the method from this study provide better accuracy in the C Marl interval.

CHAPTER 5 CONCLUSIONS

Two complete Niobrara cores from Wattenberg field were studied using a systematic approach. Core description and facies analysis were used to define sedimentary and textural variations. Ultrasonic measurements, source rock analysis and XRD mineralogy results were presented for a total of 19 core plug samples. Ultrasonic velocity was measured for both S-wave and P-wave on three principle directions: 0°, 45° and 90° in reference to the observed bedding plane. Velocities presented in this study were measured under two main conditions: benchtop conditions, with no applied pressure and under confining pressure. Four of the 19 samples were subjected to a confining pressure from 0 to 4000 psi. The same velocities were measured while pressuring up and pressuring down the sample. Several source rock analysis and XRD datapoints from previous studies were incorporated into this study. Data was integrated to investigate mineralogy, organic carbon richness and maturity effects on Niobrara Formation acoustic properties.

Facies distribution analysis results from both cores show high frequency cycles of interstratified chalks and marls with variable carbonate and clay content. Chalk pellet density and bioturbation index can be very useful in distinguishing facies. A weak correlation between chalk content and bioturbation exists. Although high facies heterogeneity exists across different cores, geomechanical, acoustic behavior and petrophysical logs are still correlatable. Samples with higher illite clay content showed a decrease in 45° and 90° velocities. Carbonate content showed a reverse effect. Carbonate and illite clay content show a significant correlation when compared against C44 and C33 stiffness coefficients. Pyrite content significantly correlate to increasing compressibility in samples. This is believed to be a proxy effect of the increased kerogen content. The effect of confining pressure was especially noticeable at the initial pressure increase stages up to 500 psi in all clay rich samples. Additionally, clay-rich samples showed decreasing anisotropy with pressure increase. Sample 3077.4 from Berthoud State 3 core which contains higher chalk content and lower clay volume showed very minimal velocity changes and respectively minimal anisotropy changes with increasing pressure. Poisson's ratio changes were inconclusive, however, clay-poor sample had much subtle response by comparison to clay-rich samples. 3077.4 sample may be interpreted as mainly isotropic due to its uniform elastic behavior.

Higher organic richness was observed to decrease C33 and C12. In contrast, Pre-existing hydrocarbons (S1) increased the transverse stiffness of the samples. Lower maturity indicated by higher S2 was associated with higher shear velocities in the 45° and 90° while

slowing down the overall compressional velocity. Both S2 and S3 showed comparable correlations to wireline compressional slowness (DTCO) and V_{S45}/ $V_{P45.}$ Hydrogen index shows possible significant correlation to V_{S90}, V_{S45}, $V_{P90,}$ DTCO and deep resistivity. Oxygen index and Tmax revealed marginal or weak significance correlations to measured elastic properties of the samples. Overall, maturation seem to enhance stiffness or rigidity of the samples. In contrast, higher kerogen content is possibly associated with a decrease in the rigidity of the samples.

The total number of statistically significant correlations generated in this study is 136: source rock richness and maturity yielded 64 with lab ultrasonic data and four significant correlations with wireline logs, total of 66 statistically significant correlations exits between XRD mineralogy and ultrasonic measurements including wireline compressional slowness (DTCO). Additionally, two significant correlations were established between core-calibrated porosity and ultrasonic measurements. Modeled regression equations with highest correlation significance were used to predict TOC, S2, HI and OI for Aristocrat PC H11-07. Note that model predictions for other parameters have been presented but are dependent on the following velocities: Vs90, Vp45 or Vs45. Lab source rock analysis was studied for this well previously (ElGhonimy, 2015). A comparison between predicted and measured source rock richness and maturity indicated the following: (1) predicted TOC can be used as a good qualitative assessment with much higher accuracy in marly zones, (2) S2 was overpredicted overall with lower error in chalk-dominated lithologies, (3) hydrogen index was erroneous and should be calibrated by a larger dataset, (4) Oxygen index provided better estimates in organic-rich intervals but can extremely underestimate OI in organic-poor zones. TOC prediction model presented in this study is a function of shear and compressional acoustic wireline logs, therefore, it can be used to assess TOC richness without core data availability. In contrast, uranium method requires actual TOC core measurements in order to generate a regression for the tested core or well. Uranium method still provides a better overall estimated trend and should be used when enough core data are available whereas the presented method can be used in wells with limited or no core TOC data.

This study provided a pilot attempt to establish a methodology through which a qualitative assessment of organic richness and maturity can be inferred with moderate to high significance. Initial results indicate high possibility of significant relationships between organic content and resulting acoustic properties of the Niobrara Formation. However, it is crucial that the presented correlations must be further investigated with a larger dataset of samples from other Niobrara cores within the same field. Such dataset enrichment is predicted to enhance the

accuracy of the estimation models. It is also highly recommended to carry out a multi-variable analysis on the dataset to separate the combined effects of mineralogy, organic richness and maturity. X-ray micro computed tomography (CT) is also recommended for the tested samples in order to understand the textural variations on the plug scale. Micro CT analysis will also provide a quantifiable measurements of micro-fractures.

REFERENCES CITED

Alam, M. M., I. L. Fabricius, and M. Prasad, 2011, Permeability prediction in chalks: AAPG Bulletin, v. 95, p. 1991-2014.

Brunauer, S., P. H. Emmett, and E. Teller, 1938, Adsorption of gases in multimolecular layers: Journal of the American Chemical Society, v. 60, p. 309-319.

Cardott, B. J., 2014. Woodford Shale play update: expanded extent in the oil window.

In: Presented at the Woodford Shale Forum 2014, May 29, 2014.

Castagna, J. P., M. L. Batzle, and R. L. Eastwood, 1985, Relationships between compressional-wave and shear-wave velocities in clastic silicate rocks: GEOPHYSICS, v. 50, p. 571-581.

Encana Corporations (2008). Wattenberg Gas Field. Town of Erie website: Document Centre. Accessed on 5 August 2015. Available at: https://www.erieco.gov/DocumentCenter/Home/View/384

Cullity, B. D., 1956, Elements of X-ray Diffraction, Addison-Wesley Publishing Company, 514 p.

Dean, W. E., and M. A. Arthur, 1998, Geochemical Expressions of Cyclicity in Cretaceous Pelagic Limestone Sequences, Stratigraphy and Paleoenvironments of the Cretaceous Western Interior Seaway, USA, v. 6, SEPM Society for Sedimentary Geology, p. 227-255.

ElGhonimy, R. S., 2015, Petrophysics, geochemistry, mineralogy, and storage capacity of the Niobrara Formation in the Aristocrat PC H11-07 core, Wattenberg field, Denver Basin, Colorado, Master's thesis, Colorado School of Mines, Golden, Colorado, 142 p.

Fabricius, I. L., C. Olsen, and M. Prasad, 2005, Log interpretation of marly chalk, the Lower Cretaceous Valdemar Field, Danish North Sea: Application of iso-frame and pseudo water film concepts: The Leading Edge, v. 24, p. 496-505.

Finn, T.M., and R.C. Johnson, 2005, Niobrara Total Petroleum System (503703) in the Southwestern Wyoming Province, in USGS Southwestern Wyoming Province Assessment Team, eds., Petroleum Systems and Geologic Assessment of Oil and Gas in the Southwestern Wyoming Province, Wyoming, Colorado, and Utah: USGS Digital Data Series DDS-69-D, chapter 6, 27 p.

Fisher, R. A., and F. Yates, 1953, Statistical tables for biological, agricultural and medical research, Oliver and Boyd, 146 p.

Gamero-Diaz, H., Miller, C. and Lewis, R. 2013. sCore: A Mineralogy Based Classification Scheme for Organic Mudstones. Paper 166284 presented at the SPE Annual Technical Conference and Exhibition, New Orleans, Louisiana, 30 September- 2 October.

Hantschel, T., and A. I. Kauerauf, 2009, Fundamentals of basin and petroleum systems modeling: Dordrecht, Berlin, Springer, 476 p.

Hornby, B. E., 1998, Experimental laboratory determination of the dynamic elastic properties of wet, drained shales: Journal of Geophysical Research: Solid Earth, v. 103, p. 29945-29964.

Jarvie, D. M., B. L. Claxton, F. Henk, and J. T. Breyer, 2001, Oil and shale gas from the Barnett Shale, Ft: Worth Basin, Texas (abs.): AAPG Annual Meeting Program, p. A100.

Jones, L. E., and H. F. Wang, 1981, Ultrasonic velocities in Cretaceous shales from the Williston basin: Geophysics, v. 46, p. 288-297.

Keel, M. B., 2015, Organic Porosity Distribution: A Function of Aromaticity in Organic-Rich Mudrocks, Master's thesis, University of Kansas, Lawrence, Kansas, 71 p.

King, M. S., 1969, Static and dynamic elastic moduli of rocks under pressure: The 11th US Symposium on Rock Mechanics (USRMS), American Rock Mechanics Association, 23 p.

Longman, M. W., B. A. Luneau, and S. M. Landon, 1998, Nature and distribution of Niobrara lithologies in the Cretaceous Western Interior Seaway of the Rocky Mountain region: The Mountain Geologist, v. 35, p. 137-170.

Maldonado, A. C., 2011, Elastic and mechanical properties of the Niobrara Formation with application to hydraulic fracture design, Master's thesis, Colorado School of Mines, Golden, Colorado, 160 p.

Nelson, P.H., and Santus, S.L., 2011, Gas, water, and oil production from Wattenberg field in the Denver Basin, Colorado: U.S. Geological Survey Open-File Report 2011–1175, 23 p.

Panfiloff, A., 2016, Experimental evaluation of dynamic elastic properties and anisotropy in shales, Master's thesis, Colorado School of Mines, 2016.

Passey, Q., S. Creaney, J. Kulla, F. Moretti, and J. Stroud, 1990, A Practical Model for Organic Richness from Porosity and Resistivity Logs: American Association of Petroleum Geologists Bulletin, v. 74, p. 1777-1794.

Pearson, K., G. Jeffery, and E. M. Elderton, 1929, On the distribution of the first product moment-coefficient, in samples drawn from an indefinitely large normal population: Biometrika, v. 21, p. 164-201.

Prasad, M., K. C. Mba, T. Sadler, and M. L. Batzle, 2011, Maturity and impedance analysis of organic-rich shales: SPE Reservoir Evaluation and Engineering, v. 14, p. 533-543.

Saidian, M., Kuila, U., Prasad, M., Alcantar-Lopez, L., Rivera, S. and Godinez, L.J., 2015, A comparison of measurement techniques for porosity and pore size distribution in mudrocks: a case study of Haynesville, Niobrara, Monterey and Eastern European Silurian Formations, AAPG Memoir 110, 60 p.

Schmoker, J. W., and T. Hester, 1983, Organic Carbon in Bakken Formation, United States Portion of Williston Basin: American Association of Petroleum Geologists Bulletin, v. 67, p. 2165-2174.

Smagala, T. M., C. A. Brown, and G. L. Nydegger, 1984, Log-derived indicator of thermal maturity Niobrara Formation, Denver Basin, Colorado, Nebraska, Wyoming, in J. Woodward, F. F. Meissner, and J. L. Clayton eds., Hydrocarbon source rocks of the greater Rocky Mountain region: Rocky Mountain Association of Geologists, p. 355-363.

Sonnenberg, S. A., 2011, The Niobrara Petroleum System: A new resource play in the Rocky Mountain Region, *in* Estes-Jackson, J.E., and Anderson, D.S., eds., Revisiting and revitalizing the Niobrara in the Central Rockies: Rocky Mountain Association of Geologists Guidebook, p. 13-32.

Tanck, G. S., 1997, Distribution and origin of organic carbon in the Upper Cretaceous Niobrara Formation and Sharon Springs Member of the Pierre Shale, Western Interior, United States, Master's thesis, The University of Arizona, Tucson, Arizona, 426 p.

Tissot, B. P., and D. H. Welte, 2013, Petroleum Formation and Occurrence, Springer Berlin Heidelberg, 702 p.

Vernik, L., and X. Liu, 1997, Velocity anisotropy in shales: A petrophysical study: Geophysics, v. 62, p. 521-532.

Vernik, L., and J. Milovac, 2011, Rock physics of organic shales: The Leading Edge, v. 30, p. 318-323.

Vernik, L., and A. Nur, 1992, Ultrasonic velocity and anisotropy of hydrocarbon source rocks: Geophysics, v. 57, p. 727-735.

Weimer, R.J., 1983, Relation of unconformities, tectonics, and sea-level changes, Cretaceous of Denver basin and adjacent area, in M. Reynolds and E. Dolly, eds., Mesozoic paleogeography of west-central United States: Denver, Colorado, Society of Economic Paleontologists and Mineralogists, Rocky Mountain Section Special Publication, p. 359-376.

Weimer, R. J., S. A. Sonnenberg, and G. B. Young, 1986, Wattenberg field, Denver basin, Colorado, in C. W. Spencer and R. F. Mast, eds., Geology of tight gas reservoirs: AAPG Studies in Geology, v. 24, p. 134-164.

Woodruff, W., A. Revil, M. Prasad, and C. Torres-Verdín, 2015, Measurements of elastic and electrical properties of an unconventional organic shale under differential loading: Geophysics, v. 80, p. D363-D383.

Wyllie, M. R. J., A. R. Gregory, and L. W. Gardner, 1956, Elastic Wave Velocities in Heterogeneous and Porous Media: Geophysics, v. 21, p. 41-70.

APPENDIX A

Table A.1 All correlation coefficients between all ultrasonic velocities and stiffness coefficients (rows) and core calibrated porosity for Gill Land 2 core (column). Darker highlight indicates higher R-value.

	Core calibrated porosity
Vp0	-0.456
Vp45	-0.543
Vp90	-0.416
Vs0	0.433
Vs45	-0.487
Vs90	-0.369
Vp/Vs0	-0.800
Vp/Vs45	0.052
Vp/Vs90	-0.004
Vs/Vp0	0.779
Vs/Vp45	-0.132
Vs/Vp90	0.001
C11	-0.581
C33	-0.522
C44	-0.401
C66	0.273
C12	-0.755
C13	-0.455

Table A.2 All significant correlation coefficients between all ultrasonic measurements (rows) and all XRD mineralogy (columns). Darker highlight indicates higher R-value.

	Illite	Mx I/S*	Calcite	Dolomite	Quartz	Plag.	Pyrite	Clays	Carb.
Vp0	-0.356	-0.249	0.385	-0.040	-0.191	-0.286	-0.415	-0.400	0.389
Vp45	-0.495	-0.232	0.504	0.057	-0.325	-0.247	-0.549	-0.505	0.517
Vp90	-0.551	-0.218	0.569	0.007	-0.425	-0.178	-0.558	-0.545	0.580
Vs0	-0.645	-0.088	0.580	-0.178	-0.501	0.011	-0.362	-0.563	0.578
Vs45	-0.542	-0.218	0.558	0.001	-0.490	-0.205	-0.409	-0.530	0.568
Vs90	-0.567	-0.120	0.530	-0.035	-0.466	-0.023	-0.392	-0.514	0.537
Vp/Vs0	-0.164	-0.287	0.251	0.010	-0.118	-0.388	-0.277	-0.254	0.256
Vp/Vs45	0.416	0.158	-0.444	0.009	0.560	0.253	0.042	0.387	-0.452
Vp/Vs90	0.310	-0.086	-0.178	-0.010	0.268	-0.090	-0.147	0.207	-0.182
Vs/Vp0	0.112	0.295	-0.211	-0.002	0.068	0.397	0.270	0.215	-0.215
Vs/Vp45	-0.374	-0.079	0.378	-0.024	-0.483	-0.120	-0.054	-0.326	0.383
Vs/Vp90	-0.334	0.125	0.176	-0.037	-0.289	0.119	0.228	-0.209	0.177
C11	-0.341	-0.254	0.364	0.029	-0.169	-0.336	-0.400	-0.391	0.373
C33	-0.567	-0.286	0.602	-0.007	-0.459	-0.245	-0.531	-0.584	0.613
C44	-0.544	-0.186	0.547	-0.080	-0.480	-0.034	-0.410	-0.522	0.551
C66	-0.126	0.200	0.014	-0.023	-0.046	0.298	0.028	-0.024	0.013
C12	-0.201	-0.303	0.278	0.035	-0.108	-0.418	-0.328	-0.293	0.285
C13	-0.108	-0.143	0.137	-0.007	-0.024	-0.249	-0.155	-0.146	0.139
ε	0.409	0.000	-0.369	-0.119	0.233	0.006	0.565	0.344	-0.384
γ	0.491	-0.048	-0.359	-0.140	0.318	0.086	0.230	0.377	-0.376
δ	0.150	0.033	-0.230	-0.115	0.072	-0.014	0.721	0.156	-0.242
K	-0.541	-0.197	0.546	0.043	-0.397	-0.279	-0.522	-0.527	0.559
Gv	-0.544	-0.186	0.547	-0.080	-0.480	-0.034	-0.410	-0.522	0.551
Gh	-0.126	0.200	0.014	-0.023	-0.046	0.298	0.028	-0.024	0.013
Ev	-0.570	-0.281	0.603	0.005	-0.482	-0.193	-0.522	-0.585	0.614
Eh	-0.345	-0.010	0.131	0.029	-0.166	-0.171	0.479	-0.268	0.135
v13	0.257	-0.123	-0.001	-0.030	0.085	0.008	-0.596	0.140	-0.003
v31	-0.123	-0.222	0.187	0.000	-0.066	-0.345	-0.196	-0.191	0.190
v12	-0.250	0.082	0.013	0.017	-0.098	-0.048	0.604	-0.151	0.015

Table A.3 All possible correlation coefficients between all ultrasonic measurements and wireline logs (rows) and all source rock analysis measurements (columns). Darker highlight indicates higher R-value.

	TOC	S1	S2	S3	Tmax (°C)	HI	OI	S2/S3	S1/TOC*100	PI	Calculated Ro
Vp0	-0.39	0.44	-0.08	-0.32	-0.14	0.15	0.08	-0.05	0.60	0.35	-0.14
Vp45	-0.48	0.47	0.29	0.06	-0.33	0.49	0.09	0.23	0.54	0.05	-0.33
Vp90	-0.48	0.53	0.38	0.07	-0.47	0.61	0.04	0.39	0.60	0.03	-0.47
Vs0	-0.12	0.52	0.33	-0.12	-0.29	0.49	-0.29	0.40	0.52	0.08	-0.29
Vs45	-0.30	0.58	0.62	0.41	-0.37	0.71	-0.13	0.52	0.48	-0.20	-0.37
Vs90	-0.24	0.62	0.66	0.37	-0.45	0.80	-0.14	0.65	0.51	-0.26	-0.45
Vp/Vs0	-0.51	-0.16	-0.63	-0.31	0.24	-0.53	0.59	-0.70	0.08	0.41	0.24
Vp/Vs45	-0.11	-0.46	-0.65	-0.53	0.12	-0.60	0.45	-0.55	-0.20	0.34	0.12
Vp/Vs90	-0.30	-0.40	-0.62	-0.50	0.06	-0.56	0.45	-0.65	-0.03	0.53	0.06
Vs/Vp0	0.50	0.14	0.64	0.31	-0.25	0.54	-0.58	0.71	-0.10	-0.42	-0.25
Vs/Vp45	0.06	0.43	0.75	0.65	-0.21	0.70	-0.32	0.61	0.19	-0.43	-0.21
Vs/Vp90	0.28	0.38	0.66	0.55	-0.14	0.56	-0.40	0.63	0.04	-0.50	-0.14
C11	-0.48	0.41	-0.12	-0.35	-0.13	0.10	0.14	-0.09	0.59	0.37	-0.13
C33	-0.54	0.62	0.36	0.08	-0.54	0.61	0.06	0.41	0.70	0.09	-0.54
C44	-0.30	0.68	0.63	0.38	-0.51	0.79	-0.07	0.63	0.58	-0.20	-0.51
C66	0.32	0.50	0.31	-0.14	-0.28	0.47	-0.24	0.39	0.53	0.08	-0.28
C12	-0.54	0.15	-0.49	-0.40	0.08	-0.30	0.45	-0.52	0.40	0.49	0.08
C13	-0.48	0.12	-0.40	-0.60	-0.37	-0.07	0.32	-0.15	0.45	0.52	-0.37
ε	0.32	-0.25	-0.38	-0.04	0.23	-0.52	-0.03	-0.26	-0.32	0.12	0.23
γ	0.07	-0.38	-0.58	-0.29	0.14	-0.63	0.26	-0.49	-0.22	0.35	0.14
δ	0.20	-0.01	-0.17	0.00	-0.10	-0.24	-0.08	-0.04	-0.11	0.10	-0.10
K	-0.44	0.41	0.26	-0.09	-0.31	0.47	-0.05	0.27	0.51	0.10	-0.31
Gv	-0.30	0.68	0.63	0.38	-0.51	0.79	-0.07	0.63	0.58	-0.20	-0.51
Gh	0.32	0.50	0.31	-0.14	-0.28	0.47	-0.24	0.39	0.53	0.08	-0.28
Ev	-0.44	0.69	0.53	0.30	-0.46	0.69	-0.06	0.50	0.62	-0.08	-0.46
Eh	-0.01	0.21	0.06	0.02	-0.10	-0.03	-0.28	0.10	0.03	0.02	-0.10
v13	-0.15	-0.14	-0.08	-0.03	0.11	0.02	0.26	-0.11	0.02	0.01	0.11
v31	-0.58	0.00	-0.50	-0.60	-0.33	-0.19	0.42	-0.26	0.35	0.53	-0.33
v12	0.14	0.15	0.06	0.04	-0.09	-0.04	-0.27	0.10	-0.03	0.00	-0.09
RHOB	-0.64	-0.52	-0.38	-0.11	0.21	-0.45	0.47	-0.33	-0.38	0.00	0.21
DT	0.28	-0.04	0.75	0.74	-0.27	0.67	0.08	0.60	-0.26	-0.79	-0.27
GR	0.49	-0.09	-0.33	-0.19	0.13	-0.50	-0.32	-0.28	-0.24	0.21	0.13
Deep Resistivity	0.45	0.30	0.72	0.64	-0.34	0.66	-0.04	0.46	0.24	-0.28	-0.34